

**SYNTHESIS AND THERMO-PHYSICAL PROPERTIES
OF Sr-CHLOROAPATITE AND ITS VARIOUS GLASS-
BONDED COMPOSITES LOADED WITH
PYROCHEMICAL CHLORIDE WASTE**

By

BINOY KUMAR MAJI

CHEM02201004012

Indira Gandhi Centre for Atomic Research, Kalpakkam

A thesis submitted to the

Board of Studies in Chemical Sciences

In partial fulfillment of requirements

for the Degree of

DOCTOR OF PHILOSOPHY

of

HOMI BHABHA NATIONAL INSTITUTE

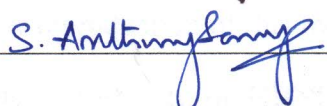


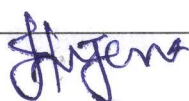
August, 2016

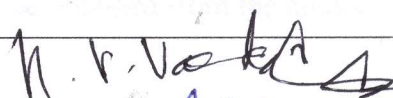
Homi Bhabha National Institute¹

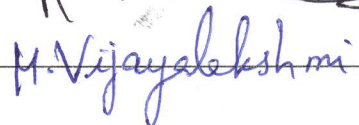
Recommendations of the Viva Voce Committee

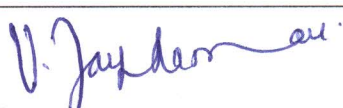
As members of the Viva Voce Committee, we certify that we have read the dissertation prepared by **BINOY KUMAR MAJI** entitled **"SYNTHESIS AND THERMO-PHYSICAL PROPERTIES OF Sr-CHLOROAPATITE AND ITS VARIOUS GLASS-BONDED COMPOSITES LOADED WITH PYROCHEMICAL CHLORIDE WASTE"** and recommend that it may be accepted as fulfilling the thesis requirement for the award of Degree of Doctor of Philosophy.

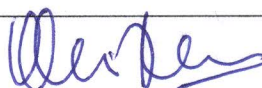
Chairman – Dr. S. Anthonysamy  Date: 4/4/2017

Guide / Convener – Dr. Hrudananda Jena  Date: 04/04/2017

Examiner – Prof. U. V. Varadaraju  Date: 4/4/17

Member 1- Dr. M. Vijayalakshmi  Date: 4/4/17

Member 2- Dr. V. Jayaraman  Date: 04.04.2017

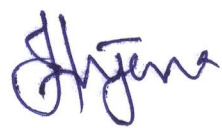
Technology Adviser- Dr. M. V. Krishnaiah  Date: 04/04/2017

Final approval and acceptance of this thesis is contingent upon the candidate's submission of the final copies of the thesis to HBNI.

I/We hereby certify that I/we have read this thesis prepared under my/our direction and recommend that it may be accepted as fulfilling the thesis requirement.

Date: 04/04/2017

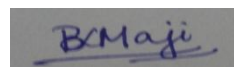
Place: Kalpakkam


Dr. Hrudananda Jena
Guide

STATEMENT BY AUTHOR

This dissertation has been submitted in partial fulfillment of requirements for an advanced degree at Homi Bhabha National Institute (HBNI) and is deposited in the Library to be made available to borrowers under rules of the HBNI.

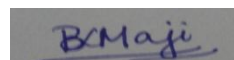
Brief quotations from this dissertation are allowable without special permission, provided that accurate acknowledgement of source is made. Requests for permission for extended quotation from or reproduction of this manuscript in whole or in part may be granted by the Competent Authority of HBNI when in his or her judgment the proposed use of the material is in the interests of scholarship. In all other instances, however, permission must be obtained from the author.

A rectangular box containing a handwritten signature in blue ink that reads "B. Maji".

(BINOY KUMAR MAJI)

DECLARATION

I, hereby declare that the investigation presented in the thesis has been carried out by me. The work is original and has not been submitted earlier as a whole or in part for a degree / diploma at this or any other Institution / University.

A rectangular box containing a handwritten signature in blue ink that reads "B. Maji".

(BINOY KUMAR MAJI)

List of Publications arising from the thesis

Journal

1. “Effect of pyrochemical waste loading on the heat capacity of $\text{Sr}_{10}(\text{PO}_4)_6\text{Cl}_2$ and its glass-bonded composites measured by drop calorimetry”, Binoy Kumar Maji, H. Jena, M. V. Krishnaiah, R. Asuvathraman, *J. Therm. Anal. Calorim.* **2016**, 124 (2), 857-863.
2. “Electrical conductivity and glass transition temperature (T_g) measurements on some selected glass used for nuclear waste immobilization”, Binoy Kumar Maji, H. Jena, R. Asuvathraman, *J. Non-Cryst. Solids*, **2016**, 434, 102-107.
3. “Effect of pyrochemical chloride waste loading on thermo-physical properties of borosilicate glass bonded Sr-chloroapatite composites”, H. Jena, Binoy Kumar Maji, R. Asuvathraman, K. V. G. Kutty, *Mater. Chem. Phys.* **2015**, 162, 188-196.
4. “Comparison of thermal expansion and heat capacity properties of various borosilicate glass-bonded strontium chloroapatite composites loaded with simulated pyrochemical waste”, Binoy Kumar Maji, H. Jena, R.V. Krishnan, R. Asuvathraman, K. Ananthasivan, K.V.G. Kutty, *J. Therm. Anal. Calorim.* **2015**, 119 [3], 1825-1831.
5. “Determination of C_p from enthalpy increment on pristine glasses and its glass-bonded ceramic composites loaded with 10 wt. % simulated pyrochemical waste by drop calorimetry”, Binoy Kumar Maji, H. Jena, M. V. Krishnaiah, **2017**, In press, DOI:10.1007/s10973-017-6163-1.

Chapters in books and lectures notes

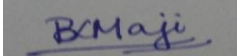
- 1.

Conferences

1. “Glass-ceramics of alkaline earth Chloroapatites as matrices for nuclear waste immobilization”, H. Jena, Binoy Kumar Maji, R. Asuvathraman, K. V. G. Kutty, AGM-2013, **2013**, IGCAR, Kalpakkam, India.
2. “Strontium chloroapatite based glass-ceramics composites for nuclear waste immobilization”, H. Jena, Binoy Kumar Maji, R. Asuvathraman, K. V. G. Kutty, RTMC-2013, 25-27th July, **2013**, CP-30, pp-54, VIT University, Vellore, India.
3. “Studies on the synthesis and thermal expansion measurements on Glass bonded-Strontium chloroapatite composites for simulated pyrochemical waste immobilization”, Binoy Kumar Maji, H. Jena, R. Asuvathraman, K. V. G. Kutty, Symposium and Workshop on Thermal Analysis (THERMANS-2013), 19th - 23rd December, **2013**, C-16, pp 355-360, DAE-BRNS, BARC, Mumbai, India.
4. “Synthesis and thermophysical property measurements on various types of glasses for nuclear waste immobilization”, Binoy Kumar Maji, H. Jena, R. Asuvathraman, Symposium and Workshop on Thermal Analysis (THERMANS-2016), **2016**, F, p-126, IIT-BHU, Varanasi, UP, India.
5. “Thermophysical properties of nuclear wasteform matrices”, R. Asuvathraman, K. Joseph, R. R. Madhavan, Binoy Kumar Maji, H. Jena, Symposium and Workshop on Thermal Analysis (THERMANS-2016), **2016**, IT, p-12, IIT-BHU, Varanasi, UP, India.

Others

- 1.


(BINOY KUMAR MAJI)

ACKNOWLEDGEMENTS

With great pleasure, I would like to express my deep gratitude to my research supervisor Dr. Hrudananda Jena, Solid State Chemistry Section, MCD, CG, IGCAR and Dr. K. V. G. Kutty, Former Head, Materials Chemistry Division, Chemistry Group, IGCAR, Kalpakkam, for their invaluable guidance, sharing of knowledge, experience and constant encouragement throughout the course of this investigation and completion of the thesis.

I sincerely thank Dr. R. Sridharan, Associate Director, MCG/CG, Dr. M. Joseph, Associate Director, FChG/CG for their constant support and encouragement.

I would like to register my special thanks to Dr. S. Anthonysamy, Chairman of Doctoral Committee and Dean of Chemical science; Dr. M. Vijayalakshmi and Dr. V. Jayaraman, members of DC, Dr. M. V. Krishnaiah, Technology adviser and Dr. K. Nagrajan, Former Director, CG (also a former DC member) for their invaluable advises, support and motivation, extended to me throughout my thesis work.

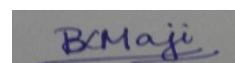
I would like to thank Dr. R. Asuvathraman, Dr. Kitheri Jeseeph, Shri R. Raja Madhavan, Shri Sanjit Kumar Parida and all my friends to their support and help during this work. I also want to thank Dr. K. Anathasivan and Dr. R. Ventakrishnan for their valuable suggestion and technical discussion.

I sincerely thank Dr. K. Sankaran and the Laboratory members of Analytical and Spectroscopy Section, MCD, CG for their invaluable help on the detailed analysis of my leaching studies samples timely. I thank Dr. R. Sudha and Shri Swapan Kumar Mahato for SEM-EDAX studies and Shri Abhiram Senapati for carrying out DSC experiments of my samples.

I also want to thank Satendra, Suranjan, Pavan, Debasish, Soumen da and Sajal da for their diversified help and continuous encouragement about my work at the tea time discussions.

I express my gratitude to my parents, my wife Rumpa and my son Arkish for their constant help, support and encouragements without which this thesis might not have come to this stage.

Finally, I acknowledge the Director, IGCAR and administrative authorities of IGCAR, Kalpakkam for giving me permission and all the facilities to do the work.

A rectangular box containing a handwritten signature in blue ink that reads "B. Maji".

(BINOY KUMAR MAJI)

CONTENTS

	Page no.
SYNOPSIS	xix
List of Figures	xxv
List of Tables	xxxi
CHAPTER 1: INTRODUCTION	
1.1 Radioactive Wastes	1
1.2 Classification of radioactive wastes	2
1.2.1 Exempt Waste (EW) and Very Low-Level Waste (VLLW)	3
1.2.2 Low-Level Waste (LLW)	4
1.2.3 Intermediate-Level Waste (ILW)	4
1.2.4 High-Level Waste (HLW)	5
1.3 Radioactive waste management in India	10
1.4 Immobilization of High-Level Waste (HLW)	11
1.4.1 Zeolites	11
1.4.2 De-chlorination and immobilization in a glass matrix	12
1.4.3 Alternate mineral matrices capable of fixing halides:	12
Immobilization of High-Level Chloride Waste in Apatite	
1.5 Apatite: Crystal Structure	13
1.6 Chemical durability of apatite and apatite glass-ceramic	14
1.7 Solid state properties of Apatites and glass bonded apatites	14
1.7.1 TG-DTA and DSC method	14
1.7.2 Thermal Expansion	17
1.7.2.1 Dependence of thermal expansion on crystal structure and bonding	19
1.7.2.2 Dependence of thermal expansion on physical properties	19
1.7.2.3 Importance of thermal expansion data	20
1.7.2.4 Methods of measuring thermal expansion coefficients	22
1.7.2.4.1 Microscopic method (Lattice expansion	22

measurement)	
1.7.2.4.2 Macroscopic methods (Bulk expansion measurements)	23
1.7.2.4.2.1 Optical Interferometry	23
1.7.2.4.2.2 Precision Optical Micrometry	24
1.7.2.4.2.3 Push-rod Dilatometry	24
1.7.2.4.3 Micro vs. Macro Methods	27
1.7.3 Heat Capacity	27
1.7.3.1 Einstein theory of heat capacity	28
1.7.3.2 Debye theory of heat capacity	29
1.7.3.3 Free electron model of metals for heat capacity	30
1.7.3.4 Requirement of heat capacity	30
1.7.4 Electrical conductivity	31
1.7.4.1 Mechanism of ionic conduction	31
1.7.4.2 Temperature dependence of ionic conductivity	32
1.7.4.3 Effect of carrier concentration and Ionic transport number on electrical conductivity	33
1.7.4.4 Criteria for solid state ionic conductivity	35
1.7.4.5 Methods of measuring ionic conductivity	35
1.7.4.5.1 DC methods	35
1.7.4.5.2 AC methods	36
1.8 Scope of the present studies	37
References	38
 CHAPTER 2: EXPERIMENTAL	
2.1 Introduction	43
2.2 Chemicals and Reagents	43
2.3 Experimental procedure	45
2.4 Instrumental techniques and principles	46

2.4.1 X-ray Diffraction (XRD)	46
2.4.1.1 X-ray Generation and properties	46
2.4.1.2 XRD Equipment	47
2.4.1.3 Powder X-ray Diffraction	48
2.4.1.4 Bragg's Law	49
2.4.1.5 High Temperature X-ray powder Diffractometry	52
2.4.1.5.1 Experimental Set-up	53
2.4.1.5.2 X-ray Diffraction at high temperatures	54
2.4.1.5.3 Thermal expansion measurement by high temperature XRD (HTXRD)	55
2.4.2 Thermal Analysis	56
2.4.2.1 Thermogravimetric Analysis (TGA)	56
2.4.2.2 Differential Thermal Analysis (DTA)	56
2.4.2.3 Differential Scanning Calorimetry (DSC)	57
2.4.2.3.1 Experimental set up for DSC measurement	57
2.4.2.3.2 Application of DSC	59
2.4.3 Scanning Electron Microscopy (SEM)	60
2.5 Leaching studies for chemical durability	60
2.5.1 Static method by hydrothermal Autoclave measurement	61
2.5.2 Dynamic method by Soxhlet measurement	61
2.6 Thermal expansion Measurement by Thermomechanical method (Dilatometry)	62
2.7 Enthalpy increment Measurement by Drop Calorimetry	64
2.7.1 Description of the Drop Calorimeter	64
2.7.2 Enthalpy increment measurement procedure	65
2.8 Electrical conductivity measurements	66

2.8.1 AC impedance spectroscopy	66
2.8.2 Analysis of impedance spectrum	67
2.8.3 Frequency response analyser	70
2.8.4 Applications of impedance measurements	72
References	73

CHAPTER 3: SYNTHESIS, CHARACTERIZATION AND THERMOPHYSICAL PROPERTY MEASUREMENT ON STRONTIUM CHLOROAPATITE AND ITS BOROSILICATE GLASS-BONDED COMPOSITE WITH SIMULATED PYROCHEMICAL CHLORIDE WASTE

3.1 Introduction	77
3.2 Experimental	79
3.2.1 Synthesis of the Sr-chloroapatite ceramic and glass-bonded simulated waste loaded Sr-chloroapatite composites	79
3.2.2 Fabrication of pellets of Sr-chloroapatite with varying amounts of chloride waste and BSG	82
3.2.3 Leaching studies on the simulated waste loaded samples by hydrothermal condition (Autoclave) and Soxhlet method	83
3.2.4 Thermal expansion measurements on the glass bonded composites by high temperature X-ray diffraction (HTXRD)	84
3.2.5 Thermal expansion and glass transition temperature (T_g) measurements by dilatometry	85
3.2.6 Glass transition temperature (T_g) and heat capacity (C_p) measurements by DSC	87
3.2.7 Enthalpy increment and C_p measurement by Drop Calorimetry	88
3.2.8 Electrical conductivity measurement by AC-impedance	90
3.3 Results and discussions	92
3.3.1 Characterization by powder-XRD and SEM-EDAX studies	92

3.3.2 Leaching studies by autoclave and soxhlet method	97
3.3.3 Thermal expansion by HTXRD	100
3.3.4 Thermal expansion by Thermomechanical analysis (dilatometry) and T_g measurement by TMA and DSC	106
3.3.5 Enthalpy increment and heat capacity by Drop calorimetry	109
3.3.6 Electrical conductivity by AC-impedance	115
References	116

CHAPTER 4: SYNTHESIS, CHARACTERIZATION AND THERMOPHYSICAL PROPERTIES ON ALIMUNO BOROSILICATE GLASS (AIBSG)-BONDED STRONTIUM CHLOROAPATITE COMPOSITES WITH SIMULATED PYROCHEMICAL CHLORIDE WASTE

4.1 Introduction	121
4.2 Experimental	122
4.2.1 Preparation and characterization of Alumino borosilicate glass (AIBSG) and its glass-bonded ceramic composite with Sr-Chloroapatite	122
4.2.2 Leaching studies on the simulated waste loaded samples by Soxhlet method	123
4.2.3 Thermal expansion measurements on the glass bonded composites by high temperature X-ray diffraction (HTXRD)	123
4.2.4 Thermal expansion and glass transition temperature (T_g) measurements by dilatometry	124
4.2.6 Glass transition temperature (T_g) and heat capacity (C_p) measurements by DSC	125
4.2.5 Enthalpy increment measurement by Drop Calorimetry	126
4.2.6 Electrical conductivity measurement by AC-impedance	126
4.3 Results and Discussions	127
4.3.1 Characterization by powder-XRD	127

4.3.2 Leaching studies by soxhlet method	129
4.3.3 Thermal expansion by HTXRD	129
4.3.4 Thermal expansion and T_g measurement by Dilatometry	132
4.3.5 Enthalpy increments and C_p measurement by Drop calorimetry	135
4.3.6 Electrical conductivity by AC-impedance	139
References	140

CHAPTER 5: SYNTHESIS, CHARACTERIZATION AND THERMOPHYSICAL PROPERTY MEASUREMENTS ON BARIUM BOROSILICATE GLASS (BaBSG)-BONDED Sr-CHLOROAPATITE COMPOSITES LOADED WITH SIMULATED PYROCHEMICAL CHLORIDE WASTE

5.1 Introduction	145
5.2 Experimental	146
5.2.1 Synthesis and characterization of barium borosilicate glass (BaBSG) and BaBSG-bonded Sr-chloroapatite composite (SrApCl-10w20BaBSG)	146
5.2.2 Leaching studies by soxhlet measurement	147
5.2.3 Thermal expansion measurements on the glass bonded composites by high temperature X-ray diffraction (HTXRD)	147
5.2.4 Thermal expansion by thermomechanical measurement (Dilatometry)	148
5.2.5 Glass transition temperature (T_g) and heat capacity (C_p) measurements by DSC	149
5.2.6 Enthalpy increments and C_p measurement by Drop Calorimetry	149
5.2.7 Electrical conductivity by AC-impedance	150
5.3 Results and Discussions	150
5.3.1 Characterization by XRD	150

5.3.2 Leaching studies by soxhlet method	152
5.3.3 Thermal expansion by HTXRD	153
5.3.4 Thermal expansion and T_g measurement by dilatometry	156
5.3.5 Glass transition temperature (T_g) by DSC	156
5.3.6 Enthalpy increment and heat capacity (C_p) by Drop calorimetry	158
5.3.7 Electrical conductivity measurement by AC-impedance	161
References	162

CHAPTER 6: SYNTHESIS, CHARACTERIZATION AND THERMOPHYSICAL PROPERTIES ON LEAD BOROSILICATE GLASS (PbBSG)-BONDED Sr-CHLOROAPATITE COMPOSITES WITH SIMULATED PYROCHEMICAL CHLORIDE WASTE

6.1 Introduction	167
6.2 Experimental	167
6.2.1 Synthesis and characterization of Sr-chloroapatite and its lead borosilicate glass-bonded composites	168
6.2.2 Fabrication of pellets of Sr-chloroapatite and its PbBSG glass-bonded composites	168
6.2.3 Leaching studies on the simulated waste loaded samples	169
6.2.4 Thermal expansion measurements by HTXRD	170
6.2.5 Thermal expansion and glass transition temperature (T_g) measurements by dilatometry	171
6.2.6 Glass transition temperature (T_g) and heat capacity (C_p) measurement by DSC	172
6.2.7 Enthalpy increment and heat capacity measurement by Drop Calorimetry	172
6.2.8 Electrical conductivity measurements by AC-impedance	173
6.3 Results and Discussions	173

6.3.1 Characterization by XRD	173
6.3.2 Leaching studies by soxhlet method	174
6.3.3 Thermal expansion by HTXRD	175
6.3.4 Thermal expansion and T_g measurement by Dilatometry	178
6.3.5 Enthalpy increment and C_p by Drop calorimetry	181
6.3.6 Electrical conductivity by AC-impedance	184
References	185

CHAPTER-7

Summary and Conclusions	189
Scope of the Work	194

SYNOPSIS

The radioactive waste generated from nuclear industry such as nuclear reactors, reprocessing of spent nuclear fuel *etc.* needs to be immobilized and stored or disposed safely for the sustenance and safe generation of nuclear power. The wastes generated by PUREX (Plutonium Uranium Extraction) process for the thermal reactor fuel reprocessing is being immobilized into borosilicate glass. Fast reactors are being built and operated to breed the fissile material to fill the scarcity of fissile material in nature to cater the growing demand for energy. The metal fueled fast reactors envisage closed fuel cycle in which pyrochemical reprocessing is the most important step to reprocess the fuel and the waste generated after the spent fuel reprocessing are in the chloride form. The solubility of chlorides in the borosilicate glass is very low and may corrode the matrix. Therefore, various matrices are being tried worldwide for the fixation of chloride waste. Currently, glass-bonded sodalites (GBS) are being studied for the immobilization of pyrochemical waste at Argonne National Laboratory. But, this process has some difficulties such as formation of less leach resistant nepheline phase, long time required for zeolite dehydration, comparatively low waste loading, high processing temperature *etc.* Therefore studies are being taken up to find out suitable matrices for immobilization of pyrochemical chloride waste. In this present study, apatites were explored as a candidate matrix for immobilizing chloride waste. Apatites are naturally occurring minerals with a general formula of $M_{10}(PO_4)_6X_2$, where (M = Ca, Sr, Ba *etc.*; X = OH, Cl, F *etc.*); depending on the M and X-constituents, the apatite is named as hydroxy, chloro, fluoro apatite. In these materials, halides are part of the crystal structure. Apatites can also incorporate alkaline earth and various other aliovalent cations into its crystal structure. Apatites crystallize in

hexagonal crystal system ($SG = P6_3/m$) and can accommodate cation and anion vacancies in its structure. Apatites are also known to have high resistance to leaching of the constituent elements under geological conditions. It may not be possible to immobilize the whole spectrum of the pyrochemical waste in a single phase Sr-chloroapatite. Therefore, attempts were made to explore the optimum waste loading into a composite matrix comprised of Sr-chloroapatite (crystalline phase) and a borosilicate glass (BSG) phase. The glass encapsulated SrApCl can immobilize most of the radwaste elements in the composite matrix, thus utilizing the immobilization efficiency of both the ceramic and glass phase. To evaluate the effect of various other glass compositions on the waste loaded glass-bonded ceramic composites, alumino borosilicate glass (AlBSG), barium borosilicate glass (BaBSG) and lead borosilicate glass (PbBSG) with Sr-chloroapatite were also studied.

Chapter-1 deals with a brief introduction to radioactive waste and the pyro-reprocessing of spent metallic fuel and their waste management. This chapter also describes the literature survey of various other matrices and the basic principles used to measure the thermo-physical properties.

In Chapter-2 the detailed description of the synthesis and characterization of glass bonded ceramic composites are given. This chapter also contains detailed experimental procedure used to measure thermo-physical properties of the composites at elevated temperatures.

Chapter-3 deals with the synthesis and optimization of simulated chloride waste loading into the glass-bonded ceramic composites. This chapter describes the synthesis of Sr-chloroapatite (SrApCl), Sr-chloroapatite with 20 wt% borosilicate glass (SrApCl-20BSG), Sr-chloroapatite with 10 wt% simulated chloride waste

(SrApCl-10w) and 10 wt% - 16 wt.% simulated waste loaded Sr-chloroapatite with 20 wt% borosilicate glass (SrApCl-10w20BSG, SrApCl-13w20BBSG and SrApCl-16w20BSG) composites. Powder-XRD patterns reveal the formation of crystalline Sr-chloroapatite phases in all the waste loaded glass-bonded ceramic composites. However, XRD pattern shows the presence of impurity phases in case of 16 wt% waste loaded glass-bonded ceramic composite. High temperature power-XRD also shows that structural transitions were not observed for the crystalline phase on heating the sample from 298 to 673 K in air. Leaching studies shows an increase in normalised leach rate with the increase in waste loading from 10 – 16 wt%. However, the composite with 10 wt% waste loading shows highest leaching resistance. The normalised leach rate was found to be in the order of $10^{-6} \text{ g cm}^{-2} \text{ d}^{-1}$ which is very much within the acceptable limits. Percentage thermal expansion also increases with increase in waste loading which was also reflected in glass transition temperatures (T_g) (i.e. lowest thermal expansion exhibits highest T_g and vice versa). Enthalpy increments (ΔH) of the glass-bonded composites were also measured by drop-calorimetric method and heat capacity (C_p) of these glass-bonded ceramic composites was calculated from this enthalpy increment data using least square fittings.

Chapter-4 deals with the synthesis and characterization of aluminoborosilicate glass-bonded ceramic composite with 10 wt% waste loading (SrApCl-10w20AlBSG). The properties of SrApCl-10w20AlBSG were also compared with that of the pristine aluminoborosilicate glass. Powder-XRD pattern of SrApCl-10w20AlBSG shows the presence of Sr-chloroapatite crystalline phase in the waste loaded glass-bonded ceramic composite. The non-occurrence of structural phase transitions was confirmed on heating the samples at 298-673 K in-situ by high temperature power-XRD

(HTXRD). Leaching studies was done by soxhlet method at 373K for 28 days and the leachate solutions were analyzed by various analytical techniques. % thermal expansion and glass transition temperatures were also measured by dilatometry which shows pristine glass exhibits the lower thermal expansion and higher T_g values compared to glass-bonded ceramic composites. Enthalpy increment values of these glass and glass-bonded ceramic composites were also measured by drop-calorimetry and using the least square fitting, heat capacity of these composites were calculated upto the temperature range of 773 K. These C_p values were then compared with the values obtained from DSC measurement and found to be in good agreement.

Similarly, Chapter-5 deals with the synthesis and characterization of barium borosilicate glass-bonded ceramic composite with 10 wt% waste loading (SrApCl-10w20BaBSG). The properties of SrApCl-10w20BaBSG were also compared with that of the pristine barium borosilicate glass. Powder-XRD pattern of SrApCl-10w20BaBSG shows the presence of Sr-chloroapatite phase in the waste loaded glass-bonded ceramic composite. High temperature power-XRD also shows the absence of structural transitions or formation of any new phases on heating the sample from 298 to 673 K in air. Leaching studies was done by soxhlet method at 373 K for 28 days in de-ionized water medium and the leachate solutions were analyzed by various analytical techniques. % thermal expansion and glass transition temperatures were measured by dilatometry. The measured T_g and thermal expansion values indicate lower % thermal expansion for pristine glass and higher T_g values compared to glass-bonded ceramic composites. Enthalpy increment values of these glass and glass-bonded ceramic composites were also measured by drop-calorimetry. Heat capacity of these composites was calculated upto the temperature range of 773 K by using the

least square fitting method. These C_p values were then compared with the values obtained from DSC measurement and found to be in good agreement.

Likewise, Chapter-6 deals with the synthesis and characterization of lead borosilicate glass-bonded ceramic composite with 10 wt% waste loading (SrApCl-10w20PbBSG). The properties of SrApCl-10w20PbBSG were also compared with that of the pristine lead borosilicate glass. Powder-XRD pattern of SrApCl-10w20PbBSG shows the prevalence of Sr-chloroapatite crystalline phase in the waste loaded glass-bonded ceramic composite. HT-XRD shows the absence of structural phase transitions or formation of any new phases on heating the sample from 298 to 673 K in air. Leaching studies was done by soxhlet method at 373K for 28 days and the leachate solutions were analyzed by various analytical techniques. % thermal expansion and glass transition temperatures were also measured by dilatometry that shows pristine glass has lower thermal expansion and higher T_g values compared to glass-bonded ceramic composites. Enthalpy increment (ΔH) values of these glass and glass-bonded ceramic composites were also measured by drop-calorimetry. Heat capacity of the composites were calculated from the ΔH value upto the temperature range of 773 K using the least square fitting method. These C_p values were then compared with the values obtained from DSC measurement and found to be in good agreement.

From these above observations, it can be concluded that all the four glass compositions form glass-bonded ceramic composites without any second phase with 10 wt% of simulated chloride waste. High temperature XRD studies also show the absence of structural transitions or formation of new phases from the constituent elements added to the glass-ceramic composite on heat-treating the composites. These

data reveals the structural stability of the composites in presence of the decay heat from the radio-nuclides present in the waste form. The results obtained from leaching studies imply, SrApCl-10w20BSG exhibit higher leach resistance than SrApCl-10w20AlBSG, SrApCl-10w20BaBSG and SrApCl-10w20PbBSG. The measured % thermal expansion found to show an increasing trend of SrApCl-10w20AlBSG < SrApCl-10w20BSG < SrApCl-10w20BaBSG \approx SrApCl-10w20PbBSG, which was also manifested in glass transition temperature. The trend of T_g values were found to be SrApCl-10w20AlBSG > SrApCl-10w20BSG > SrApCl-10w20PbBSG > SrApCl-10w20BaBSG. However, the difference in thermal expansion coefficients was very small. The measured heat capacity values found to be in the order of SrApCl-10w20BSG > SrApCl-10w20AlBSG > SrAPCl-10w20BaBSG > SrApCl-10w20PbBSG. C_p value is one of the important criteria for selecting the matrix and it is desirable to be high for the host matrix to qualify for waste immobilization.

From the above studies it is evident that 10 wt. % waste loading is feasible into the glass bonded ceramic composites without deviating from the desired criteria of a suitable matrix such as low leach rate, thermal stability etc. Among the various types of glass-bonded ceramic composites, SrApCl-10w20BSG is found to be more suitable and closely satisfy the desired requirements of a best matrix than SrApCl-10w20AlBSG, SrApCl-10w20BaBSG and SrApCl-10w20PbBSG composites.

List of Figures	Page no.
Fig. 1.1: Activity of radionuclides in HLW from the reprocessing of SNF with time after reprocessing	6
Fig.1.2: Electrorefining process in pyrochemical reprocessing	7
Fig. 1.3: Schematic of $\text{Ca}_5(\text{PO}_4)_3(\text{OH})$	13
Fig. 1.4: Condon-Morse curve of potential energy vs. interatomic separation	18
Fig. 1.5: Schematic diagram of an interferometer for the measurement of thermal expansion	24
Fig. 1.6: Schematic diagram of a) sample assembly, b) measurement circuit of a push-rod dilatometer for the measurement of thermal expansion	26
Fig. 2.1: PANalytical X'Pert powder diffractometer for XRD measurement	48
Fig. 2.2: Reflection and Transmission geometry in XRD	49
Fig. 2.3: Interaction of X-rays with matter	51
Fig. 2.4: Incidence and diffraction of x-rays on to the lattice	51
Fig. 2.5: Schematic of diffraction from parallel plane of a crystal	52
Fig. 2.6: Schematic of X-ray diffraction geometry including the high temperature measurement attachment	54
Fig. 2.7: Schematic of a Differential Scanning Calorimeter	58
Fig. 2.7a: Temperature control loop where the sample and reference are	58

always kept at same T	
Fig. 2.8: A typical DSC thermogram of polymer sample	59
Fig. 2.9: Apparatus set-up of Soxhlet measurement for leaching studies	62
Fig. 2.10: Photograph of home-built calorimeter	65
Fig. 2.11: Area under the curve for enthalpy increment measurement	66
Fig. 2.12: a) Equivalent circuit of a ceramic electrolyte, b) Complex impedance plot	68
Fig. 2.13: Schematic of impedance measurement	71
Fig. 2.14: Schematic of cell assembly for the electrical conductivity measurement	71
Fig. 3.1: Measured and fit enthalpy increments values and heat capacity of standard MgO compared with the Knacke <i>et. al.</i>	90
Fig. 3.2: Room temperature XRD patterns of SrApCl + x wt. % Waste + y wt. % BSG composites, (x = 0 - 16, y = 0 - 20)	93
Fig. 3.3: The crystal structure of Sr ₁₀ (PO ₄) ₆ Cl ₂	95
Fig. 3.4: (a) SEM image of SrApCl-10w20BSG showing the Crystalline and glass phases and (b) Corresponding EDAX of the SEM image shown in (a)	96
Fig. 3.5: Plot of normalised leach rates vs. compositions of glass-bonded composites	99
Fig. 3.6: Normalised leach rate (NLR, g cm ⁻² d ⁻¹) vs. Time (d) for SrApCl-10w20BSG by soxhlet method	99
Fig. 3.7: High temperature XRD patterns of the SrApCl + 13 wt. % waste + 20 wt. % BSG composites at temperatures mentioned	101

in the pattern	
Fig. 3.8: Comparison of lattice constants (a -axis) vs. T (K) of the compositions	102
Fig. 3.9: Comparison of lattice constants (c) vs. T (K) of the compositions from HTXRD data	103
Fig. 3.10: Mean coefficient of thermal expansion (α_m) vs. T of the composites along a -axis from HTXRD data	104
Fig. 3.11: Mean coefficient of thermal expansion (α_m) vs. T of glass composites along c -axis from HTXRD	105
Fig. 3.12: Typical heat-treated SrApCl pellet used for thermal expansion by Push rod dilatometry	105
Fig. 3.13: % thermal expansion of SrApCl + x waste + 20 BSG composites by dilatometry	107
Fig. 3.14: Instantaneous CTE (α_i) vs. T showing the glass transition temperature (T_g) of glass bonded composites	108
Fig. 3.15: T_g measurement BSG, SrApCl-20BSG and SrApCl-10w20BSG by DSC method	109
Fig. 3.16: Enthalpy increment with T (K) for SrApCl and its glass-bonded composites compare with pure BSG	110
Fig. 3.17: Heat capacity vs. T (K) of SrApCl and its glass bonded composites with pure BSG	115
Fig. 3.18: Arrhenius plot of $\log(\sigma T)$ vs. $1000/T$ for various glass-bonded ceramic matrices	116
Fig. 4.1: Room temperature XRD patterns of SrApCl, SrApCl-	128

10w20AlBSG and AlBSG

Fig. 4.2:	Normalised leach rate with time for SrApCl-10w20AlBSG	129
Fig. 4.3:	HT-XRD patterns of SrApCl-10w20AlBSG at various temperatures	130
Fig. 4.4:	Lattice parameter (<i>a</i> -axis) expansion with T (K)	131
Fig. 4.5:	Lattice parameter (<i>c</i> -axis) expansion with T (K) by HTXRD	131
Fig. 4.6:	Volume expansion with T (K) by HTXRD	132
Fig. 4.7:	% TE vs. T (K) for SrApCl, SrApCl-10w20AlBSG and AlBSG by dilatometry	134
Fig. 4.8:	Comparison of glass transition temperature (T_g) for SrApCl-10w20AlBSG and AlBSG	135
Fig. 4.9:	Enthalpy increments measurements of SrApCl, SrApCl-10w20AlBSG and AlBSG	137
Fig. 4.10:	Heat capacity measurements of SrApCl, SrApCl-10w20AlBSG and AlBSG by drop calorimetry	137
Fig. 4.11:	Comparison of Electrical conductivity of SrApCl, SrApCl-10w20AlBSG and pristine AlBSG	139
Fig. 5.1:	XRD patterns of SrApCl, SrApCl-10w20BaBSG and BaBSG at room temperatures	151
Fig. 5.2:	Normalised leach rate with time for SrApCl-10w20BaBSG	152
Fig. 5.3:	HTXRD patterns of SrApCl-10w20BaBSG at various temperatures	153
Fig. 5.4:	Lattice parameter (<i>a</i> -axis) expansion with T (K) by HTXRD	154
Fig. 5.5:	Lattice parameter (<i>c</i> -axis) expansion with T (K) by HTXRD	155

Fig. 5.6:	Lattice cell volume expansion with T (K) by HTXRD	155
Fig. 5.7:	Percentage linear thermal expansion of SrApCl, SrApCl-10w20BaBSG and BaBSG with T (K)	157
Fig. 5.8:	Glass transition temperatures (T_g) for BaBSG and SrApCl-10w20BaBSG by DSC and dilatometry	157
Fig. 5.9:	Enthalpy increments measured and fit values of SrApCl, SrApCl-10w20BaBSG and BaBSG with T (K)	159
Fig. 5.10:	Heat capacity of SrApCl, SrApCl-10w20BaBSG and BaBSG with T (K)	160
Fig. 5.11:	Electrical conductivity of SrApCl, SrApCl-10w20BaBSG and BaBSG	162
Fig. 6.1:	Room temperature XRD patterns of SrApCl, SrApCl-10w20PbBSG and PbBSG	174
Fig. 6.2:	Normalised leach rate with time for SrApCl-10w20PbBSG	175
Fig. 6.3:	HT-XRD patterns of SrApCl-10w20PbBSG with T (K)	176
Fig. 6.4:	Lattice parameter (a -axis) expansion with T (K) by HTXRD	177
Fig. 6.5:	Lattice parameter (c -axis) expansion with T (K) by HTXRD	177
Fig. 6.6:	Cell volume (V) expansion with T (K) by HTXRD	178
Fig. 6.7:	Percentage linear thermal expansion of SrApCl, SrApCl-10w20PbBSG and PbBSG with T (K)	179
Fig. 6.8:	Glass transition temperature measurements for SrApCl-10w20PbBSG and PbBSG by DSC as well as by dilatometry	180
Fig. 6.9:	Measured and Fit values of enthalpy increment with T (K) for SrApCl, SrApCl-10w20PbBSG and PbBSG	182

Fig. 6.10: Heat capacity measurement with T (K) for SrApCl, SrApCl-10w20PbBSG and PbBSG by drop calorimetry	182
Fig. 6.11: Electrical conductivity measurements of SrApCl, SrApCl-10w20PbBSG and PbBSG	185
Fig. 7.1: Percentage thermal expansion vs. T (K) plot of Sr-chloroapatite glass-bonded composites with various types of glass bonding material	191
Fig. 7.2: Heat capacity values of the glass-bonded composites obtained from drop calorimetry measurements	192

List of Tables	Page no.
Table 2.1: Chemicals name, formula, company name	44
Table 3.1: Compositions of simulated glass waste	80
Table 3.2: Composition of Sr-chloroapatite glass composite with simulated waste shown in mass and mol % for a 10 g target matrix (with 10 wt. % waste + 20 wt. % BSG + 70 wt. % SrApCl composite)	80
Table 3.3: Synthesized Sr-chloroapatite and its glass-bonded composites	81
Table 3.4: Thermodynamics functions of SrApCl	111
Table 3.5: Coefficients of fit equations, $H_T^0 - H_{298K}^0 = a + bT + cT^2 + d/T$	111
Table 3.6: Enthalpy increments and heat capacity data for SrApCl-10w	112
Table 3.7: Enthalpy increments and heat capacity data for SrApCl-20BSG	113
Table 3.8: Enthalpy increments and heat capacity data for SrApCl-10w20BSG	114
Table 3.9: Enthalpy increments and heat capacity data for BSG	114
Table 4.1: Lattice constants calculated from the XRD patterns of $Sr_{10}(PO_4)_6Cl_2$ and waste-loaded glass-bonded composites	128
Table 4.2: Comparison of T_g values by DSC and dilatometric method for AlBSG and SrApCl-10w20AlBSG	135
Table 4.3: Enthalpy increments and heat capacity data for SrApCl-	138

10w20AlBSG

Table 4.4: Enthalpy increments and heat capacity data for AlBSG	138
Table 4.5: Coefficients of fit equations, $H_T^0 - H_{298K}^0 = a + bT + cT^2 + d/T$	139
Table 5.1: Lattice constants of SrApCl and SrApCl-10w20BaBSG recorded at room temperature	152
Table 5.2: Comparison of T_g values by DSC and dilatometric method for BaBSG and SrApCl-10w20BaBSG	158
Table 5.3: Enthalpy increments and heat capacity data for SrApCl-10w-20BaBSG	160
Table 5.4: Enthalpy increments and heat capacity of BaBSG	161
Table 5.5: Coefficients of fit equations, $H_T^0 - H_{298K}^0 = a + bT + cT^2 + d/T$	161
Table 6.1: Comparison of T_g values by DSC and dilatometric method for PbBSG and SrApCl-10w20PbBSG	180
Table 6.2: Coefficients of fit equations, $H_T^0 - H_{298K}^0 = a + bT + cT^2 + d/T$	183
Table 6.3: Enthalpy increments and heat capacity data for SrApCl-10w-20PbBSG	183
Table 6.4: Enthalpy increments and heat capacity of PbBSG	184
Table 7.1: T_g values of glass-bonded composites measured by dilatometry and DSC	192

INTRODUCTION

1.1 Radioactive Wastes

Radioactive waste is waste product containing radioactive materials, usually the product of a nuclear process such as nuclear fission. The safe and effective management of radioactive waste is extremely important in nuclear industry. In India it covers the entire range of activities from handling, treatment, conditioning, transport, storage and final disposal. Radioactive waste [1] is generated at various stages of the nuclear fuel cycle, which includes the mining and milling of Uranium ore, fuel fabrication, reactor operation, spent fuel reprocessing and vitrification of waste products in suitable matrices. Besides these sources, radioactive wastes are also encountered by ever increasing uses of radioisotopes in other industries such as medicine industry and agriculture *etc.* These radioactive wastes are assumed to give special importance and different dimension owing to be very hazardous for the environment as day by day these nuclear activities are going to increase. Radioactive waste management is also associated with decontamination and decommissioning activity in nuclear power plants, fuel fabrication plants and reprocessing plants. Depending upon the level of radioactivity, the wastes are classified as Low-Level Waste (LLW), Intermediate Level-Waste (ILW) and High-Level Waste (HLW). As these are harmful for the biosphere as well as for the mankind, the underlying objective that governs the management of all such waste is to protect in the future. In India, the necessary codes and safety guidelines for achieving this objective are provided by the Atomic Energy Regulatory Board (AERB) in conformity with the principle of radiation protection as formulated by the International Commission on Radiation Protection (ICRP). Indian waste management facilities are co-

located with waste generating facilities *i.e.* nuclear reactor, reprocessing plant and fuel fabrication facility, so as to avoid any undue radiation exposure during transportation of waste from one place to another. The objective is to restrict radioactive exposure levels to As Low As Reasonably Achievable (ALARA) [2]. In India, we have many nuclear power plants and several fuel reprocessing plants.

The national policy for the radioactive waste management [3] is consistent with the universally accepted philosophy of:

- 1) Delay decay of short-lived radionuclides,
- 2) Concentrate and containment of radioactivity as much as practicable, and
- 3) Dilution and dispersion of low-level activity to the environment at levels well below the nationally accepted level, which are in line with international practices.

1.2 Classification of radioactive wastes

Classification of waste is very important from safety and process consideration. Important parameters to be taken into account include physical, chemical, radiological and biological properties as well as criticality aspects and origin of waste. Classification of waste into different categories is useful in their segregation, selection of appropriate treatment process, storage and disposal.

Radioactive wastes are generated in various forms like solid, liquid or gas [1]. Their classification of solid, liquid and gaseous waste according to International Atomic Energy Agency (IAEA) is as follows [4]:

Category	Solid	Liquid	Gaseous
	Surface dose (mGy/hr)	Activity level (Bq/m ³)	Activity level (Bq/m ³)
I	< 2	< 3.7 x 10 ⁴	< 3.7
II	2 – 20	3.7 x 10 ⁴ - 3.7 x 10 ⁷	3.7 – 3.7 x 10 ⁴
III	> 20	3.7 x 10 ⁷ - 3.7 x 10 ⁹	> 3.7 x 10 ⁴
IV	α- bearing	3.7 x 10 ⁹ - 3.7 x 10 ¹⁴	-
V	-	> 3.7 x 10 ¹⁴	-

In the nuclear fuel cycle, liquid waste and solid wastes constitute the most commonly generated from variety of process. The general classifications of the liquid radioactive waste are as follows

Radioactive level	Radioactivity (Bq/m ³)
Potentially active	< 3.7 x 10 ⁴
EW & VLLW	3.7 x 10 ⁴ - 3.7 x 10 ⁷
LLW	3.7 x 10 ⁷ - 3.7 x 10 ⁹
ILW	3.7 x 10 ⁹ - 3.7 x 10 ¹⁴
HLW	> 3.7 x 10 ¹⁴

(Specific activity of Radium = Activity of 1 g of Radium)

1.2.1 Exempt Waste (EW) and Very Low-Level Waste (VLLW)

Exempt waste and Very Low-Level Waste (VLLW) is radioactive waste which contains radioactive materials at a level which is not consider harmful to people or the surrounding environment and might be exempted from nuclear regulatory control *i.e.* although still radioactive from a physical point of view, but this waste may be safely

disposed off, applying conventional techniques and systems, without specifically considering its radioactive properties. It mainly consists of demolished material such as concrete, plaster, bricks, metal, valves, piping etc. produced during rehabilitation or dismantling operations at nuclear plant sites. Other industries, such as food processing, chemical etc. also produced VLLW as a result of the concentration of natural radioactivity present in certain minerals used in their manufacturing processes.

1.2.2 Low-Level Waste (LLW)

Low level wastes are limited amounts of long lived radionuclides. Such waste requires robust isolation and containment for periods of up to a few hundred years and is suitable for disposal in engineered near surface facilities. This class covers a very broad range of waste. LLW contains negligible amount of radionuclides, produced by peaceful nuclear activities in industry, medicine and research. These wastes include packages such as gloves, glass, small tools, paper and filters which have been contaminated by radioactive materials. Low-level Wastes are generated during operation of reactor coolant system clean up, decontamination and as secondary waste from treatment of HLW and ILW. The conditioning of these waste aims at removal of the major nuclide by suitable processing followed by immobilization of the concentrate and disposal of bulk quantity of aqueous waste. LLW may also include short lived radionuclides at higher levels of activity concentration, and also long lived radionuclides, but only at relatively low levels of activity concentration.

1.2.3 Intermediate-Level Waste (ILW)

Intermediate level wastes are particularly of long lived radionuclides, requires a greater degree of containment and isolation than that provided by near surface disposal

during the time for which institutional controls can be relied upon. Therefore, waste in this class requires disposal at greater depths, of the order of tens of meters to a few hundred meters. However, ILW needs no provision, or only limited provision, for heat dissipation during its storage and disposal. It may contain long lived radionuclides, in particular, alpha emitting radionuclides. Intermediate-Level Wastes contain higher amounts of radioactivity and requires some shielding. It typically comprises resins, chemical sludge and metal fuel cladding, as well as contaminated materials from reactor decommissioning. Liquid and sludge may be solidified in concrete or bitumen for disposal. It makes up some 7% of the volume and has 4% of the radioactivity of all radioactive waste.

1.2.4 High-Level Waste (HLW)

High level wastes are those wastes with levels of activity concentration high enough to generate significant quantities of heat by the radioactive decay process or waste with large amounts of long lived radionuclides that need to be considered in the design of a disposal facility for such waste. Disposal in deep, stable geological formations usually several hundred meters or more below the surface is the generally recognized option for disposal of HLW. High-Level Waste arises from the reprocessing of spent nuclear fuel discharged from nuclear reactor. In the aqueous PUREX process, it contains the fission products and trans-uranic elements generated in the nuclear core. HLW accounts for over 95% of the total radioactivity produced in the process of nuclear electricity generation [5]. The major components of high-level waste are [6]:

1. Fission products such as ^{90}Sr , ^{137}Cs , ^{144}Ce , ^{146}Nd , ^{147}Pr , and ^{151}Sm etc.
2. Actinides such as ^{241}Am , ^{244}Cm , un-recovered U and Pu etc.
3. Activated corrosion products of Fe, Ni, Cr, Mn etc from the structural materials.

4. Chemicals introduced in the reprocessing plant like HNO_3 , NaNO_2 , and traces of tributyl-phosphate (TBP) and its degradation products.

A graphical representation of radioactivity due to radionuclide in HLW from the reprocessing of spent nuclear fuel with time is given in Fig. 1.1.

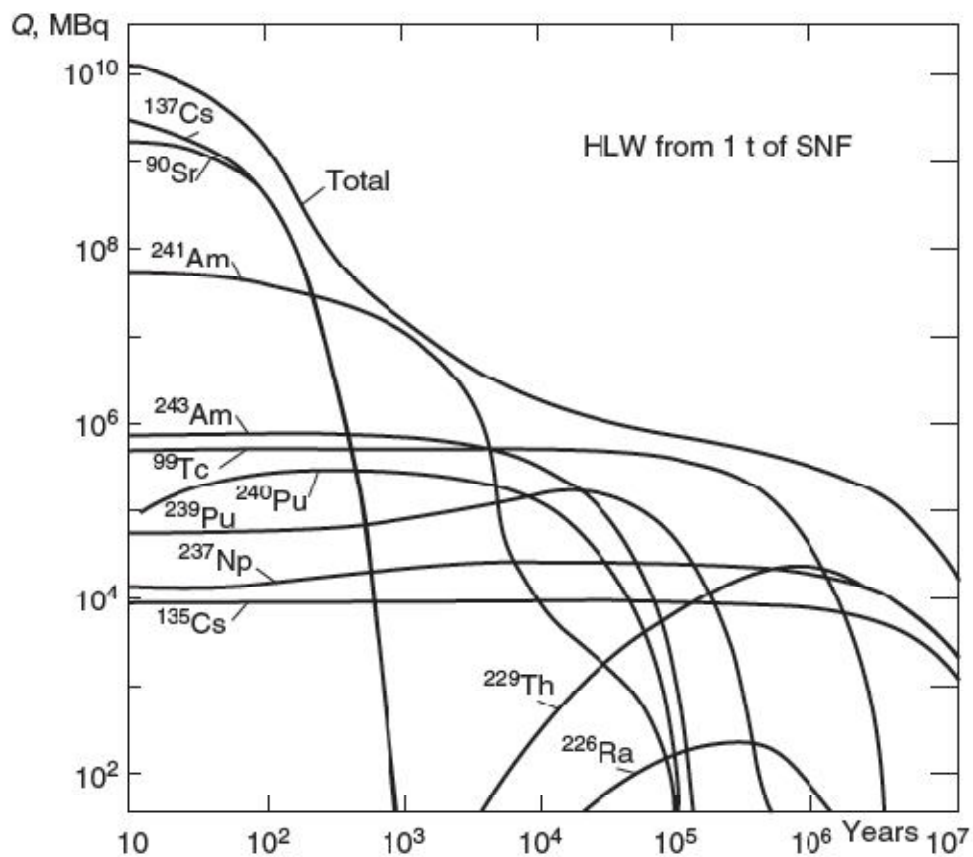


Fig. 1.1: Activity of radionuclides in HLW from the reprocessing of SNF with time after reprocessing [7]

High-Level Waste (HLW) is the most important type of nuclear waste. High level waste is very radioactive and therefore, requires special shielding during handling and transport. It also needs cooling, because it generates a great deal of heat. It is generally accepted that the final waste will be disposed of in a deep geological repository, and many

countries have developed plans for such a site, including France, Japan, and the United States.

Fast reactors in India in the near future will be fueled by metallic fuel, and these will be reprocessed by the Pyrochemical Process [8]. This is known as Non-aqueous process of reprocessing. In pyrochemical reprocessing molten LiCl (58.5 mol% or 45 wt. %) – KCl (41.5 mol% or 55 wt. %) eutectic is used as electrolyte which has a low eutectic temperature of 773 K.

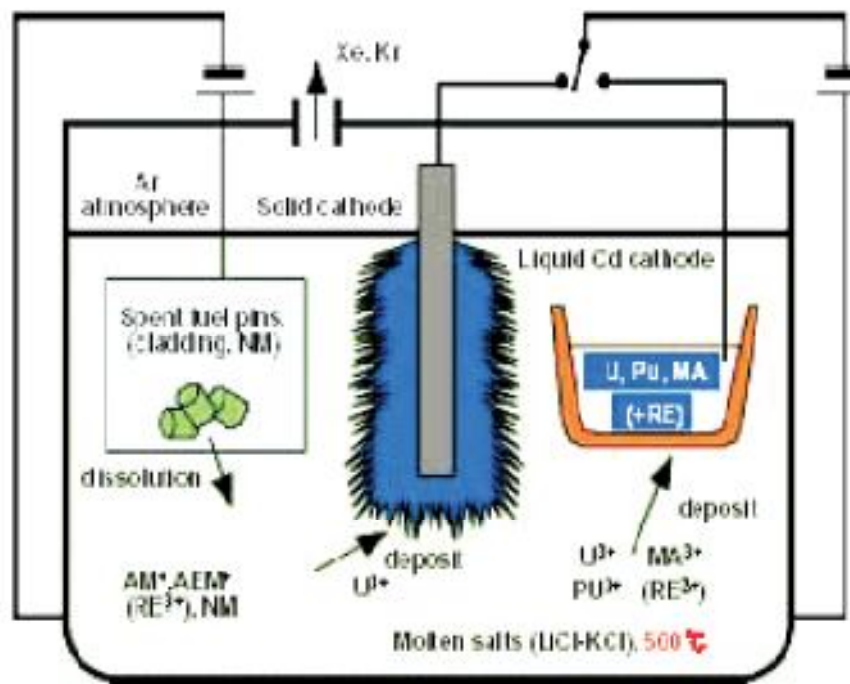


Fig. 1.2: Electrorefining process in pyrochemical reprocessing

The chopped spent fuel was taken into an anode basket as shown in the Fig. 1.2, the anode, cathode were immersed in molten salt electrolyte. U, Pu and some minor actinides (MA) were electrotransported and in molten salt medium on to the solid stainless steel / liquid cadmium cathode. Thus in this process, U, Pu and some minor actinides were recovered from the spent fuel, leaving behind novel metals, stainless steel clad and fission

products (rare earth, alkali, alkaline earth etc.) chlorides as radioactive-waste material. The radioactive waste generated from this process will be of two types: (a) Metal waste form and (b) ceramic waste form which are considered as high level waste (HLW).

a) **Metal waste form:** The sticking salts on the contents of anode basket are removed by distilling at 1100°C . Extra Zr is added and the metallic mixture is melted at 1600°C in Ar in a casting furnace, so as to form ingots of a durable stainless steel composition containing Zr to the extent of 15 wt. %. This constitutes the metal waste form, considered fit for disposal in geological repositories.

b) **Ceramic waste form:** This ceramic waste eventually consists of fission products chlorides of alkali, alkaline earth rare earth metals and electrolyte chloride of LiCl and KCl. This contains fission products such as ^{89}Sr , ^{137}Cs etc. which has long half-life ($t_{1/2}$ is ~ 30 years). Hence, these chloride wastes generated from pyrochemical reprocessing need to be immobilized in suitable matrices.

Advantages of Pyroreprocessing:

1. Satisfactory resistance to radiation damage of the inorganic molten salt used in pyrochemical reprocess allowing treatment of materials with minimum prior cooling, thereby reducing cooling period inventory costs.

2. By this process, metals are deposited in the cathode, which can be used directly in fuel fabrication; thereby reducing number of steps for fuel fabrication for metallic fuel compare to aqueous processes.

3. Lower criticality hazards due to the absence of water, which causes neutron ($0n^1$) moderation in the process (moderation of neutron leads to the criticality for chain reaction to start).

4. Minor actinides recycling are feasible in this pyrochemical reprocessing, which can be used in IFR to convert long lived minor actinides into short lived fission products.

5. In this process, the wastes generated were in the form of solid rather than liquid wastes which are easy to handle.

6. Fuel and target solubility in molten salt are good, thereby facilitating the electrorefining process.

7. Molten salt electrolyte is having a wide temperature range that amplifying the differences in thermodynamic stability, which control the good separation factors among compounds.

Disadvantages of Pyroprocessing:

1. Low separation factors compared with aqueous reprocessing.
2. Sophisticated technology is required by the high process temperature and need for operating under controlled atmosphere.
3. Maintaining an inert atmosphere at higher operating temperature is the primary condition in this process, which is a big challenge.
4. As we used molten salt chlorides, the process media is highly aggressive to process equipment leads to corrosion.

1.3 Radioactive waste management in India

The national policy for radioactive waste management [4] is broadly as follows:

- Discharge through gaseous, liquid and terrestrial routes are as low as reasonably achievable-technical, economic and social factors taken into account.
- Low and intermediate level solid/solidified waste are emplaced in near surface shallow land repository, specially engineered for this purpose.

➤ High-level and alpha contaminated liquid waste from spent fuel processing and other radio metallurgical operations are immobilized in a suitable matrix and stored in an interim storage facility with appropriate cooling and surveillance for a period as necessary. Thereafter, these solidified waste products will be emplaced in a suitably engineered deep geological repository.

➤ Alpha contaminated waste not qualifying for near surface disposal is provided suitable interim storage pending its disposal in a deep geological repository.

➤ Spent radiation sources are either returned to the original supplier or handed over to a radioactive waste management agency identified by the regulatory body.

➤ Co-location of near surface disposal facility with the nuclear installations.

➤ In the Indian context, spent fuel is a resource material and which can be processed for recovery and recycle of fissile material. Each reprocessing plant has, therefore, a co-located vitrification plant.

➤ The regulatory body determines the period for which active control of the shallow land repository (like monitoring, surveillance, and remedial work) of the repository should be maintained by the waste management agency. Thereafter, the passive control (like permanent markers and land use restrictions) will be passed on to the Central Government, the agency for institutional control. Institutional control may span a period of 300 years comprising, typically, 100 years of active control and 200 years of passive control so as to allow decay of most of the radionuclides present in the waste rendering them innocuous.

1.4 Immobilization of High-Level Waste (HLW)

Vitrification (fixing of radiological waste into a suitable host matrix) of high-level liquid waste is the well known process for the waste generated finally from the PUREX

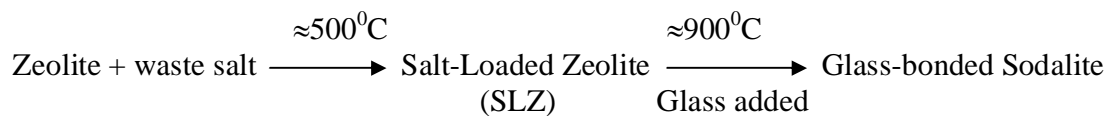
process which is followed most of the countries including India [9, 10]. But in case of Pyrochemical Reprocessing, the HLW will be mainly chloride waste [8]. This HLW can not be fixed with glass, because the solubility of chlorides in borosilicate glass matrix is very low and hence borosilicate glass can not accumulate the large amounts of halides present in the waste generated from the pyrochemical reprocessing [11].

The most commonly used matrices are:

1.4.1 Zeolites

Zeolites are crystalline aluminosilicates materials that have a high capacity for adsorption of various molecular species. Their structures are formed from the cross-linking of SiO_4 and AlO_4 tetrahedra. Chloride salts are occluded at around 500°C into the cross-linked cavity structure of Zeolite [12].

Glass bonded sodalite composite matrix- when zeolite were mixed with waste salts & glass forming reagents and heated to 900°C , then it is converted to glass- bonded sodalite composite matrix [13].



The disadvantages of this process are:

1. Dehydration step of Zeolite need to be carried out for long time.
2. During this process, nepheline phase was also formed along with glass-bonded sodalite, which is less leaching resistance.
3. Waste loading is $\sim 8 - 10$ wt%.
4. Processing temperature for this process is higher.

1.4.2 De-chlorination and immobilization in a glass matrix

De-chlorination of the respective salts was done and then the chloride free wastes are immobilized in a glass matrix. This process has some serious disadvantages like de-chlorination will be difficult.

1.4.3 Alternate mineral matrices capable of fixing halides: Immobilization of High-Level Chloride Waste in Apatite

Attempts were made to immobilize the chloride wastes in another type of matrix, namely apatites [8, 14]. Apatite is a group of naturally occurring phosphate minerals, usually referring to hydroxyapatite, chloroapatite, fluoroapatite etc. General formula of Apatite's is $M_{10}(AO_4)_6X_2$. M may be Ca, Sr, Ba, Rare Earth *etc*; X may be -OH, -Cl, -F *etc*; A may be P, S, Si *etc*. The most common sub-group in apatite is phosphate group. Phosphate apatite is not only a geological mineral, but is also a bio-ceramic. Hydroxyapatite is an important component of bone and teeth enamel. Alkaline earth metal hydroxyapatites can take chloride (as anions) in its co-ordination zone to form chloroapatites and it can also accommodate alkali and rare earth (as cations) in the metal coordination site to form non-stoichiometric analogs. Although, it may not be possible to immobilize the entire waste spectrum in chloroapatite alone; hence, studies were carried out on strontium chloroapatite and its glass-bonded composites for the immobilization of simulated chloride waste generated from pyrochemical reprocessing. This thesis consists of the synthesis of various glass-bonded ceramic composites of strontium chloroapatite and their thermophysical characterization by various techniques to explore the possibility of finding a suitable host matrix for the chloride waste immobilization. In this study, various apatite ceramics and glass-bonded ceramics are prepared, and characterized by XRD (phase identification), thermal analysis (thermal

stability) and SEM (surface morphology) - EDAX (qualitative amounts of the element present into the matrix).

1.5 Apatite: Crystal Structure

A schematic of apatite crystal structure is given in Fig. 1.3. Calcium hydroxyapatite has a complicated structure in which the unit cell contains two formula units of $\text{Ca}_5(\text{PO}_4)_3(\text{OH})$. In this compound Ca-ion exist in two different chemical environments, four Ca ions occupy one Ca_I site and other six occupy another structurally distinct Ca_II site [15].

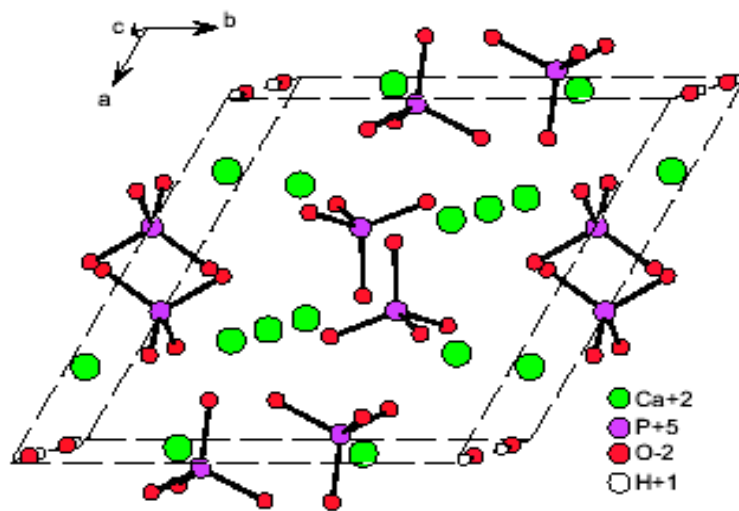


Fig. 1.3: schematic of $\text{Ca}_5(\text{PO}_4)_3(\text{OH})$

The important characteristics of apatites are:

- 1) Apatites are naturally occurring minerals and durable in nature for long time.
- 2) Thermally stable.
- 3) Leaching of elements from the apatite matrix is low (*i.e.* good chemical durability).
- 4) Resistant to radiation damage.
- 5) Easy to prepare the matrix.

1.6 Chemical durability of apatite and apatite glass-ceramic

Chemical durability refers to the relative resistance of a waste form against attack from aqueous solution or any other bio-sphere medium. Leaching means selective removal of some species or materials from one to another medium. The original advantage seen for the apatite was its very low leach ability in ground water compared to borosilicate glass. Apatite has a moderate hardness and is less susceptible to cracking. All phosphate minerals have very low solubility in water and fluoroapatite has the lowest solubility compared to hydroxyl- and chloro-apatite, which is confirmed by the lower solubility product of fluoroapatite [16-18]. The details of leaching studies were given in Chapter 2.

1.7 Solid state properties of Apatites and glass bonded apatites

1.7.1 TG-DTA and DSC method

Thermogravimetry (TG) is a technique by which weight of a sample is measured as a function of temperature or when expose to uniform heating or cooling. It records the weight changes in a sample with respect to the temperature. Changes refer either to desorption of volatile components from the sample (negative weight change) or to absorption of gaseous components from the atmosphere surrounding the sample (positive weight change). In a typical TGA experiment a sample within an Al_2O_3 crucible is placed on top of a thermocouple resting on a balance. The system is sealed into a chamber and heated with a constant heating rate.

Similarly, Differential Thermal Analysis (DTA) is a technique by which change in temperature between the sample and the reference material is measured as a function of temperature or time when exposed to uniform heating or cooling. It records the temperature of a sample as compared to a reference material. Positive and negative peaks on the

otherwise smooth DTA curve qualitatively reveal the thermodynamic nature (exo- or endo-thermic) of the changes occurring in the sample. In a typical DTA experiment a sample within an Al_2O_3 crucible and an empty Al_2O_3 crucible are placed on top of two thermocouples. The system is sealed into a chamber and heated with a constant heating rate.

On the other hand, Differential Scanning Calorimetry (DSC) is a thermoanalytical technique in which the difference in the amount of heat required to increase the temperature of a sample and reference is measured as a function of temperature. Both the sample and reference are maintained at nearly the same temperature throughout the experiment. It records the heat flux in and out of the sample as compared to a reference material. In addition to the information acquired through DTA, the specific heat capacities (C_p , $\text{J g}^{-1} \text{K}^{-1}$) of the materials as well as latent heats for the transitions can be quantified. In a typical DSC experiment a sample within a platinum crucible and an empty platinum crucible are respectively placed on two special thermocouple sensors, designed for monitoring heat fluxes. The system is then sealed into a chamber heated with a constant heating rate. The observed heat flux is proportional to the specific heat capacity of the sample. Three measurements are carried out: First a baseline with empty crucibles is recorded. Then a standard sample (normally sapphire) is introduced into the sample crucible and measured. Finally, the standard sample is replaced by the sample under investigation and the measurement is repeated a third time. The specific heat capacity of the sample as a function of temperature is eventually calculated from the ratio of the heat fluxes to the sample and the standard.

Differential scanning calorimetry can be used to measure a number of characteristic properties of a sample. Using this technique it is possible to

observe fusion and crystallization events as well as glass transition temperatures T_g . DSC can also be used to study oxidation, as well as other chemical reactions [19-21].

Glass transitions may occur as the temperature of an amorphous solid is increased. These transitions appear as a step in the baseline of the recorded DSC signal. This is due to the sample undergoing a change in heat capacity; no formal phase change occurs [19, 22].

As the temperature increases, an amorphous solid will become less viscous. At some point the molecules may obtain enough freedom of motion to spontaneously arrange themselves into a crystalline form. This is known as the crystallization temperature (T_c). This transition from amorphous solid to crystalline solid is an exothermic process, and results in a peak in the DSC signal. As the temperature increases the sample eventually reaches its melting temperature (T_m). The melting process results in an endothermic peak in the DSC curve. The ability to determine transition temperatures and enthalpies makes DSC a valuable tool in producing phase diagrams for various chemical systems.

1.7.2 Thermal Expansion

The expansion of materials under the influence of heat is the manifestation of the anharmonicity of the lattice vibrations. In case of harmonic / symmetric vibration, the mean position of the atoms in the crystal lattice would not change even though the vibrational amplitudes would increase with the increasing in temperature. The Condon - Morse curve which explains the change in potential energy with interatomic distance between a pair of atoms / partially charged atoms in a solid was given in Fig. 1.4, where r_0 represents the interatomic distance at T_0 K and r_1 , r_2 are the interatomic separations at T_1 and T_2 K respectively. A_1A_2 and B_1B_2 are the vibrational amplitudes at temperature T_1 K and T_2 K. The equilibrium distances (interatomic separation, $r_2 > r_1 > r_0$) increase with the increase in

temperature from T_0 to T_1 to T_2 K. The Debye theory of solids also confirmed that the lattice vibrational modes ranging from zero to a maximum value of ν_{\max} are also progressively excited. At the Debye temperature,

$$\theta_D = h\nu_{\max} / k \quad (1.1)$$

, the maximum of vibrational frequency and amplitude were attained.

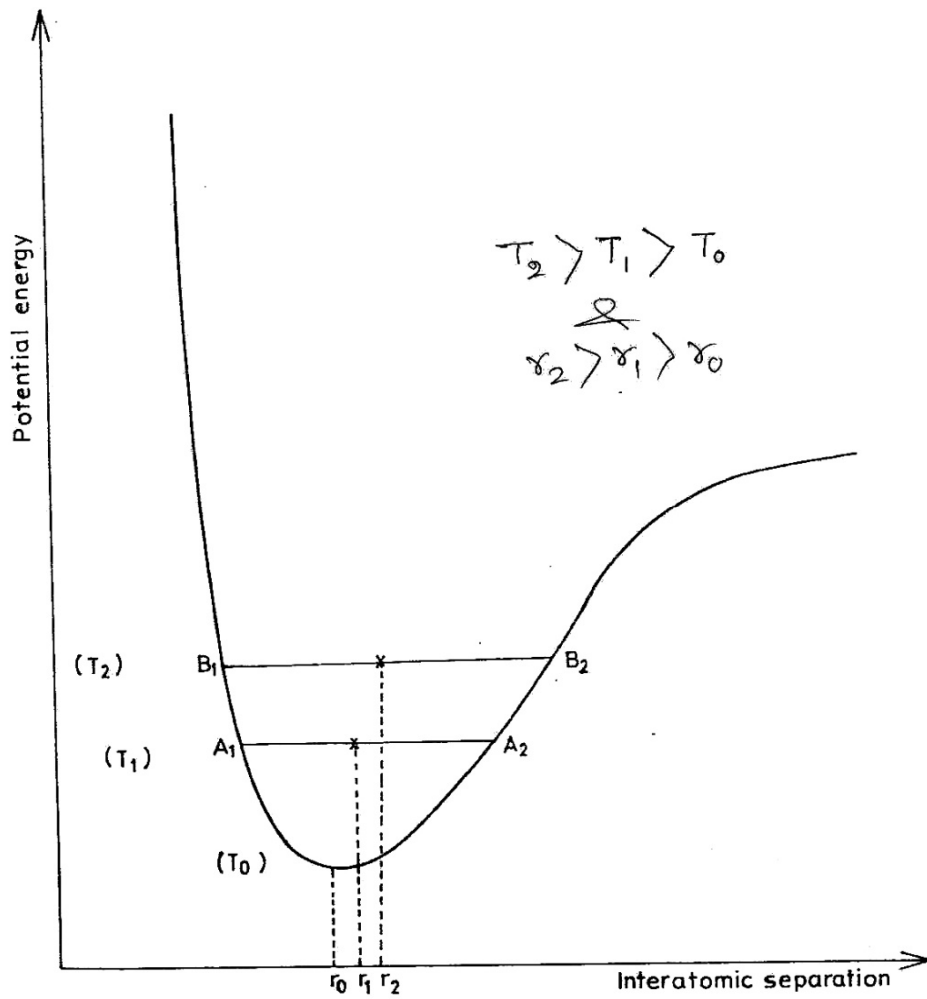


Fig. 1.4: Condon-Morse curve of potential energy vs. interatomic separation; where equilibrium interatomic separation increases with increase in temperature

The linear mean thermal expansion coefficient (α_m) *i.e.* thermal expansivity of materials is defined as the change in length ($\Delta L/L$) per unit increase in temperature (ΔT). It is often expressed in the unit of 10^{-6} K^{-1} . Depending upon the value of thermal expansion, Agarwal et al. [23] have broadly classified materials into three classes: (i) High expansion materials: $\alpha > 8 \times 10^{-6} \text{ K}^{-1}$, (ii) Intermediate expansion materials: $2 < \alpha < 8 \times 10^{-6} \text{ K}^{-1}$ and (iii) Low expansion materials: $\alpha < 2 \times 10^{-6} \text{ K}^{-1}$.

Low thermal expansion materials display high resistivity towards the heating by any external source and vice versa. Therefore, they may call high thermal shock resistance materials or refractory materials. They have many practical applications, from the mirror substrate in space satellite to the resistance to radiation damage due to the decay heat by the radioactive elements. These low thermal expansion materials are generally found in low symmetry crystal system such as tetragonal or hexagonal structure. Apatites are one such hexagonal crystal system.

1.7.2.1 Dependence of thermal expansion on crystal structure and bonding

The thermal expansion of materials primarily depends on the crystal lattice and bonding of that particular material. The stronger the bonding, lower will be the expansion and vice versa. For covalent bonding, the Condon-Morse potential energy curve is steeper and more symmetric when compared to the ionic and metallic bonding. Hence, the materials exhibit predominantly covalent bonding will have lower thermal expansion compared to the ionic or metallic bonding. ‘Open structure’ crystals are found to exhibit low thermal expansions because the changes in interatomic separation can be accommodated within the structure itself. Two main sources of thermal expansion have to be recognized: bond length effect and bond angle effect [24]. The bond length effect is related to the strength of the

bonds within the polyhedral, and the bond angle effect is related to the changes in angles between the coordination polyhedra. So, a combination of both two factors will determine the overall thermal expansion. Based on the several compounds, Hazen and Finger [25] have tabulated the expansion coefficients of a large number of compounds characterized mainly by oxide polyhedra, derived empirical relationship that a given cation-oxygen polyhedron (*e.g.* MO₆, MO₄ *etc.*) exhibit the same expansion coefficient in different compounds.

1.7.2.2 Dependence of thermal expansion on physical properties

For crystalline materials, dimensional changes were necessity along with temperature so as to minimize the free energy of the system. At moderate and high temperature the contributing to the free energy are mostly due to phonon vibration (quantized lattice vibrations), and thus are responsible for the thermal expansion.

The thermal expansion of a material is linked to its other physical properties, *e.g.* specific heat capacity, elasticity, melting point, IR and Raman spectrum, phase transformation, electro and magnetostriction and thermal conductivity. According to Grüneisen, the coefficient thermal expansion (α) can be expressed as,

$$\frac{3\alpha}{\chi_T} = \frac{\gamma C_v}{V} \quad (1.2)$$

Where, χ_T = isothermal compressibility of the solid, α = average thermal expansion (β = volume thermal expansion = 3α), C_v = specific heat capacity at constant volume, V = molar volume and γ = Grüneisen parameter.

The Grüneisen parameter represents the strength of the anharmonic forces operating in the crystal lattice and is temperature dependent, but is constant over limited ranges of temperature [26]. It has a numerical value of around 1.5 - 2.5 [27].

1.7.2.3 Importance of thermal expansion data

Some important applications of high temperature thermal expansion data are briefly discussed below.

1. Thermal expansion coefficients are needed to convert the experimentally observed C_p of materials to C_v by the thermodynamic expression (Eqn. 1.3) [28]

$$C_p - C_v = \frac{\beta^2 V T}{\chi J} \quad (1.3)$$

Where, β = volume expansion coefficient, V = molar volume, χ = isothermal compressibility and J = Joule's equivalent of heat.

2. The thermal expansion of nuclear fuel materials is responsible for the fuel-clad mechanical interaction [29]. The differential expansion between the fuel and clad can lead to gap closure in helium-bonded fuel pins, thereby affecting the gap conductance and hence the centre-line temperature of the fuel pin. A prior knowledge of the thermal expansion with temperatures helps in the calculation of fuel density as a function of temperature, which is essential information for studying the variation of its thermal conductivity with temperature.

3. In the development of multiphase mineral assemblages and glass-ceramic composites as radioactive waste forms for disposal, the thermal expansion coefficients of the phases should be mutually compatible. Large differences in thermal expansivity can cause cracking in the composites, which can lead to increase in leaching of the radioactive elements [30].

4. Measurement of thermal expansion coefficient as a function of temperatures helps in the study of phase transformations. Korner *et al.* [31] have carried out detailed phase diagram investigations on reduced cerium dioxide by thermal expansion measurements.

5. Thermal expansion data are important in designing materials of high thermal shock resistance (TSR).

$$TSR = \frac{\alpha_f k}{\alpha_1 E} \quad (1.4)$$

Where, α_f = fracture strength, k = thermal conductivity, α_1 = thermal expansion coefficient and E = Young's modulus.

6. Ceramic coatings are often applied on metallic components operating in extreme environments in order to protect them against corrosion and wear. The thermal expansion coefficients of the ceramic and the metallic substrate should match for high coating integrity, especially when temperature cycling operations are involved [32]. Likewise, in solid oxide fuel cells, the thermal expansion coefficients of the electrolytes and electrodes should match for the electrochemical processes to take place effectively [33].

1.7.2.4 Methods of measuring thermal expansion coefficients

The methods of thermal expansion measurement can be classified into two categories which are Microscopic method (Lattice expansion measurement), and Macroscopic methods (Bulk expansion measurements).

1.7.2.4.1 Microscopic method (Lattice expansion measurement)

High temperature X-ray diffraction constitutes the micro method which will be described in detail in Chapter 2.

Advantages of X-ray methods:

The x-ray method has the following advantages over the bulk methods,

(i) It is an absolute method for determination of the value of α , whereas most other methods make use of a reference standard at the temperature of the specimen.

(ii) It determines the dimensions of the crystal unit cell, unaffected by eventual impurity present in the crystal lattice. This is not so in case of a macroscopic measurement.

The knowledge of lattice thermal expansion is significant from the point of view of comparison with theory.

(iii) A small quantity of the specimen is sufficient to yield the required information. Therefore x-ray techniques are often the preferred method whenever the specimen is anisotropic because all the other methods require larger specimen size.

(iv) For anisotropic crystals, a single experiment yields complete information on the expansion coefficients along various direction.

(v) The powder technique is suitable to study variation of α with temperature through phase transitions, irrespective of the order of phase change.

Disadvantages of X-ray methods:

(i) One main disadvantages of x-ray method is that dynamic measurements (continuous study of the variation of lattice spacing as the temperature of the specimen is varied continuously) are not possible and this makes this method useless as tool to judge the nature of the expansion anomaly in a phase manner.

(ii) This method can't be applicable for the non-periodic substances like glass.

1.7.2.4.2 Macroscopic methods (Bulk expansion measurements)

The macro methods consist of optical and electrical methods where the expansions of bulk solids were measured. Some of these macroscopic methods are briefly explained below.

1.7.2.4.2.1 Optical Interferometry

The schematic diagram of an interferometer is given in Fig. 1.5 [35]. The test specimens, which can be as small as 200 μm thick, separate two quartz discs. The surfaces of the discs act as reflecting surfaces for monochromatic radiation from a helium light source.

When the path difference between the two reflected rays is an integral multiple of wavelength, interference rings can be seen.

When temperature increases, the upper disc is pushed up. This alters the path differences between the two reflected rays and the interference fringes appear to move. The number of fringes, n passing a reference mark in the eye-piece is counted. If, l is the length of the specimen and λ the wavelength of the radiation, the change in length can be expressed as

$$\delta l = \frac{n\lambda}{2l} + \frac{A}{l} \quad (1.5)$$

Where, A = correction factor, which has to added when the experiment is conducted in a medium other than vacuum. In direct reading interferometers, photomultiplier tubes are used to record the interference fringes.

This is an absolute technique which is very precise and accurate. With quartz as reflecting discs, measurement can be done upto 1273 K, whereas with sapphire, a maximum temperature of 2073 K can be attained.

1.7.2.4.2.2 Precision Optical Micrometry

The expansion of materials in this method is obtained directly by observing the position of two index marks on a long specimen by means of two calibrated telemicroscopes mounted on an invar (a Fe-Ni alloy of low thermal expansion coefficient) support [36]. These microscopes are kept focused on the index marks and can be made to follow their displacement when temperature is raised. The specimen used in the form of cylindrical from of length ~ 10 cm and dia ~ 5 -10 mm. This is also an absolute method and can go upto 2573 K with the help of graphite tube furnace.

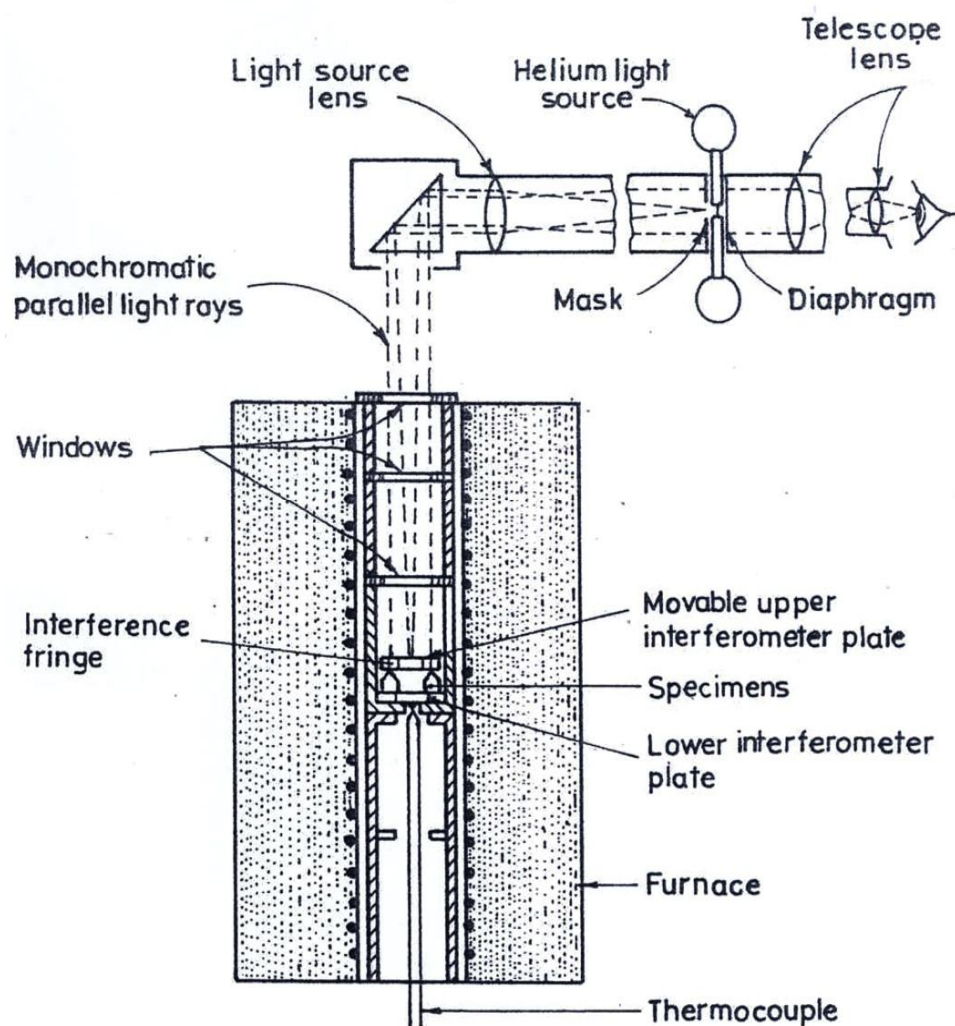


Fig. 1.5: Schematic diagram of an interferometer for the measurement of thermal expansion

1.7.2.4.2.3 Push-rod Dilatometry

In this method, the change in length with temperature is measured by using a linear variable differential transformer (LVDT). The details of this measurement are described in Chapter 2. The schematic of a push-rod dilatometer was shown in Fig. 1.6: (a) & (b). This method involved the measurement of dl between a quartz rod and the specimen plus a quartz rod. When the sample expands, the quartz rod is pushed up and the change in length, dl is measured by LVDT. By employing quartz rods, a maximum temperature of 1273 K and with

sapphire, a maximum temperature of 2073 K can be attained in this technique. Typical specimens used are of length 12-15 mm and dia 8-10 mm.

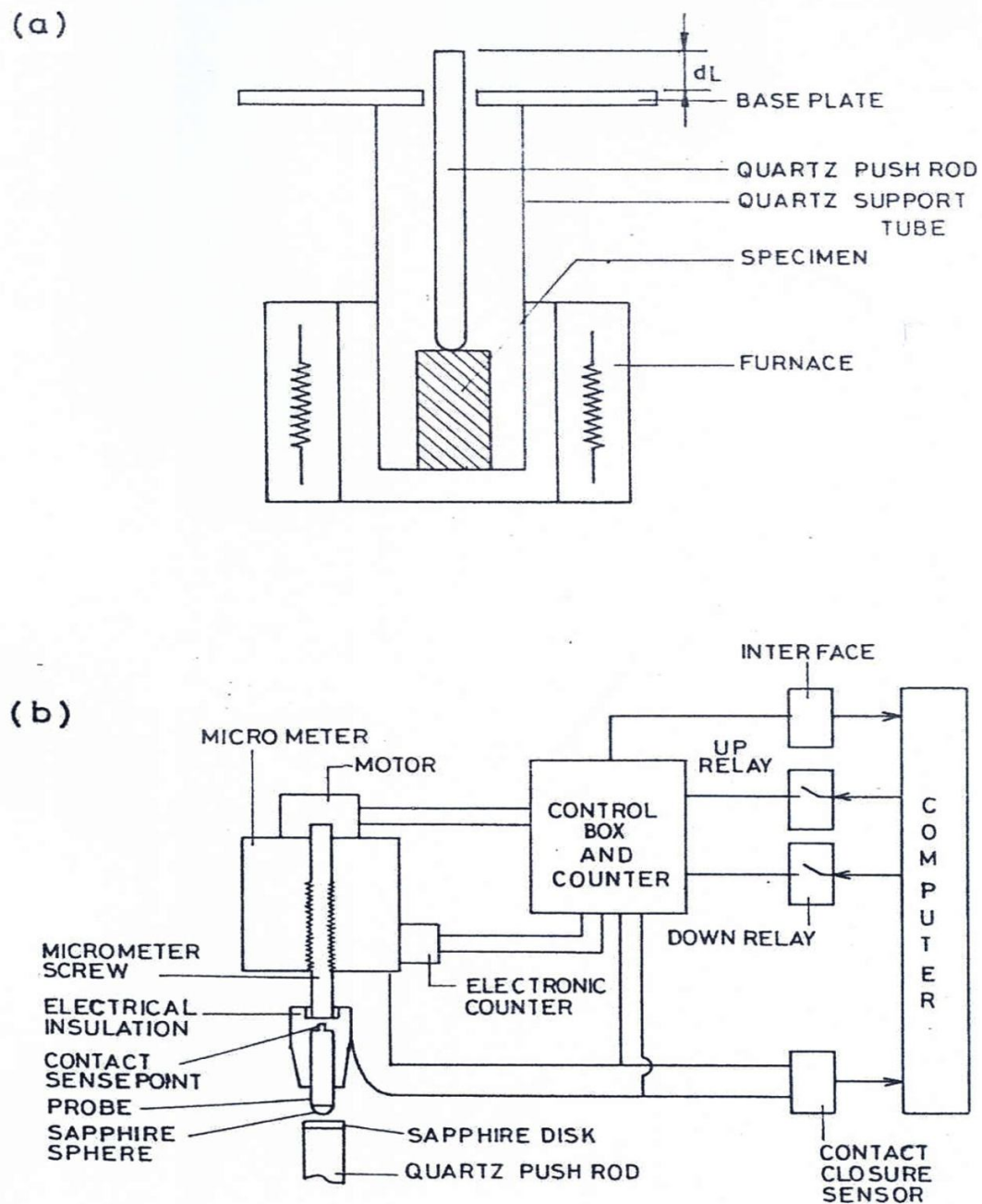


Fig. 1.6: Schematic diagram of a) sample assembly, b) measurement circuit of a push-rod dilatometer for the measurement of thermal expansion [37, 38]

1.7.2.4.3 Micro vs. Macro Methods

At high temperature, there can be some differences in thermal expansion coefficients measured by micro and macro methods; the macro methods giving perceptibly higher values. This is due to the effect of thermally generated vacancy (whose concentrations become appreciable at high temperature) in the solid. Since the x-ray probe only the average unit cell, the effect due to vacancies is not reflected in this technique.

Similarly, the effect of porosity in crystalline specimens will be manifest only in the macro methods. Polycrystalline samples have to be sintered to near theoretical densities for deriving reliable thermal expansion data by macro methods.

By employing the x-ray diffraction method for expansion measurement on a multiphase material, phase selectivity can be achieved and in the case of anisotropic crystal systems, axial selection can also be made. This is known as study of expansion anisotropy.

1.7.3 Heat Capacity

Heat capacity is the solids ability to absorb and retain heat and expressed as the amount of heat required to increase temperature of one mole of substance by one unit. Dulong-Petit conducted experiments in 1819 on 3-D solid crystals to determine the heat capacities of a variety of these solids. Dulong-Petit discovered that most of the solids had a heat capacity at constant volume is $\sim 6 \text{ C mol}^{-1} \text{ K}^{-1}$ at 298 K. They consider every atom inside the solid as an oscillator with six degrees of freedom and extended into 3-D space. Each atom has energy of $\frac{1}{2} k_B T$, where k_B is the Boltzmann constant and T is the absolute temperature. Thus,

$$C_v = \frac{6}{2} R = 3 R \quad (1.6)$$

The number 6 in this equation is the number of degrees of freedom for the molecule. However, the explanation for Dulong-Petit experiment was not sufficient when it was discovered that heat capacity decreased as temperature approached absolute zero. The degrees of freedom do not slow down or cease to move when the solid reaches a sufficiently cold temperature.

1.7.3.1 Einstein theory of heat capacity

Einstein assumed, firstly, the atoms in a crystal lattice undergo small oscillations (vibrations) about their equilibrium configuration. In fact an ideal crystal can be considered as a system of $3N$ non-interacting particles / atoms. Secondly, each atom vibrates independently of each other and has 3 independent vibrational degrees of freedom. Thus, the crystal may be treated as a system of $3N$ independent and distinguishable harmonic oscillators.

Einstein's model reveals the accuracy of heat capacity at high temperatures. When examining the extremely low temperature limit: $\theta_E / T \gg 1$, it can be seen:

$$C_v = 3N k_B \left(\frac{\theta_E}{T}\right)^2 e^{-\left(\frac{\theta_E}{T}\right)} \quad (1.7)$$

As temperature (T) goes to zero, the exponential portion of the above equation goes to zero and therefore C_v also approaches zero. This supports the experimental values as temperature approaches zero the heat capacity of the solid likewise decreases to zero.

However, Einstein's theory is not successful in predicting the C_v values in the lower and intermediate temperature range; the values predicted by it lower than the those actually observed.

1.7.3.2 Debye theory of heat capacity

Debye model estimated the phonon contribution to the heat capacity in a solid. It treats the vibration of the atomic lattice as phonons in a box. Debye avoided the most serious assumption of Einstein theory, namely, that the vibrations in a crystal lattice are independent. He recognised that the interatomic forces in a crystal are very strong and hence the atoms may not be treated as independent. Therefore, Debye assumed that “the properties of the crystal could be determined from a superposition of contributions due to each possible vibrational mode, rather than by summing the contributions made by individual atoms, which means that the atomic crystal to have $3N$ normal vibrations, each having a unique frequency”.

Debye model correctly predicts the low temperature dependence of the heat capacity, which is proportional to T^3 -known as Debye T^3 law. Just like Einstein model, it also recovers the Dulong-Petit law at high temperatures. But, due to simplifying assumptions, its accuracy suffers at intermediate temperatures.

The heat capacity at low- T is given by,

$$C_v = \frac{dU}{dT} = \frac{16 \pi^4 k_B^4}{5 h^3 C_s^3} T^3 \quad (1.8)$$

Debye temperature is the temperature of crystal highest normal mode of vibration, ($\theta_D = h \nu_m / k$), *i.e.* the highest temperature that can achieved highest single normal mode of vibration.

1.7.3.3 Free electron model of metals for heat capacity

Up to this point, we have only considered contributions to the heat capacity from vibrations within the solid. In metals, the free conduction electrons also contribute to the heat capacity. In the free electron model of metals, the conduction electrons are treated as a perfect gas obeying Fermi-Dirac statistics. Interactions of the electrons with the positively charged atomic ions and with the other electrons are neglected.

The heat capacity per electron turns out to be

$$C_v = \frac{\pi^2}{2} k_B \frac{T}{T_F} \quad (1.9)$$

At room temperature this is a very small contribution to the overall heat capacity (on the order of a few percent). However, at very low temperatures the electronic heat capacity dominates, since it is linear in temperature while the lattice heat capacity is proportional to T^3 .

1.7.3.4 Requirement of heat capacity

Heat capacity of the host matrix as well as the waste loaded host matrix is of the important parameter for choosing a matrix for immobilization especially in nuclear waste immobilization. The heat capacity of the composite matrix should be high enough so that it

can accommodate the decay heat release by radioactive particularly long lived fission products as well as by the short lived fission products.

1.7.4 Electrical conductivity

Electrical conduction of solids is due to the migration of electrons or ions under the influence of an applied potential gradient. Conducting solids where majority of charge carriers are ions (cations or anions), are called ionic conductors. Solid ionic conductors have seen rapid growth with the discovery of new crystalline, glassy, polymer and composite materials [39-43]. Ionic conductors exhibiting Na^+ , Li^+ , Ag^+ , F^- and O^{2-} ions conduction are well known and typical examples are Na^+ ion in sodium zirconium silico phosphates, sodium borosilicate glasses; Li^+ ions in LiI / lithium ion batteries; F^- in CaF_2 , calcium fluoroapatite; and O^{2-} in calcia stabilized zirconia (CSZ, $\text{Ca}_x\text{Zr}_{1-x}\text{O}_{2-x}$) respectively.

1.7.4.1 Mechanism of ionic conduction

Ionic transport in crystals can be described by a vacancy or an interstitial model / mechanism, or by a combination of both. The vacancy mechanism involves the motion of a vacancy through the crystal lattice by successive jump in the direction opposite to the vacancy motion. The best example was observed in the case of Schottky defects crystal lattice in which either cations (+ve ion) or anions (-ve ion) leave their normal sites to create vacancies. In the interstitial model, the ions moves through a series of interstitial sites present in the crystal lattice. This was observed in Frankel defects crystals lattice, where, the ions merely jump from one interstitial site to another. Whereas in combination of vacancy and interstitial mechanism called as Interstitialcy mechanism; an interstitial ion jumps to a normal site, pushing the ion to another interstitial site and thereby creating a vacancy at the

interstitial site as well as an interstitial. Such type of vacancy and interstitial can also be responsible for the ionic conduction in solids.

1.7.4.2 Temperature dependence of ionic conductivity

The behavior of a mobile ion can be identified as diffusion processes; such as vacancy diffusion (though mobility of vacancies) and interstitial diffusion (through the mobility of interstitial). These are thermally activated phenomenon and the current carriers move under the influence of an external field. The dependence of ionic conductivity, σ in crystals can be represented by the Arrhenius Eqn. 1.10,

$$\sigma = \frac{A}{k_B T} e^{-(E_a/k_B T)} \quad (1.10)$$

Where, A=pre-exponential factor which depends on the charge and concentration of the mobile ion, E_a =activation energy for the successful jumps of mobile ions, which can be expressed as a sum of two terms: the binding energy of the ion to the crystal lattice and the energy required to overcome the structural constraints constituted by the coordination polyhedra [44]. E_a in most of the ionic conduction was generally varied from 0.8-1.2 eV. k_B is the Boltzmann constant and T is the absolute temperature (K). The pre-exponential factor, A is given by

$$A = \frac{1}{3} (Ze)n d^2 \omega_0 \quad (1.11)$$

Where, d is the unit jump distance (normally the distance between the closest ion pair) and ω_0 is the jump attempt frequency.

The corresponding diffusion coefficient, D is defined as

$$D = D_0 e^{-(E_a/k_B T)} \quad (1.12)$$

and D_0 is given by

$$D_0 = \frac{A}{(Ze)^2 n} \quad (1.13)$$

From the equations (1.11), (1.12) and (1.13), conductivity, σ is obtained as

$$\sigma = n (Z e)^2 \frac{D}{k_B T} \quad (1.14)$$

The equation 1.14, relating conductivity to diffusion coefficient is called the Nernst-Einstein equation.

From equation 1.14, it is clear that in order to have large ionic conductivity; the number of vacancies must be large enough so that the effective number of ions contributing to the diffusion has to be large. That means, if, the number of available sites is larger than the number of diffusing ions, the ions can distribute over these available sites at relatively low temperatures, thus leading to higher conductivity.

1.7.4.3 Effect of carrier concentration and Ionic transport number on electrical conductivity

The electrical conductivity (σ) of a solid irrespective of the nature of the charge carriers can be expressed as

$$\sigma = n (Ze) \mu \quad (1.15)$$

Where, n = the number of j-type carriers, Z = the number of electronic charges e on the carrier, and μ = the mobility of the j-type species ($\text{m}^2 \text{s}^{-1} \text{V}^{-1}$). To get higher conductivity, n and μ should be high. The number of current carrying species is constant for a dopant concentration at low temperatures (extrinsically created current carriers by substitution). Thus for a particular dopant material, conductivity depends on the ionic mobility, whose temperature dependence can be expressed as

$$\mu = \mu_{\max} e^{-(E_m/k_B T)} \quad (1.16)$$

Where, E_m is the activation energy of migration of ions or vacancies.

If, conductivity depends on both the ions / carriers concentration and mobility, then it is given by combining equations (1.15) and (1.16);

$$\sigma = n (Ze) \mu_{\max} e^{-(E_m/k_B T)} \quad (1.17)$$

At higher temperatures, the concentration of thermally induced current carriers (cations or anions or polarons *etc.*) is greater than the carrier concentration associated with the dopant. Hence, the number of current carriers is temperature dependent and can be expressed as;

$$n = n_{\max} e^{-(E_f/2k_B T)} \quad (1.18)$$

Where, $E_f/2$ is the activation energy required for formation of one mole of vacancies (current carriers), i.e half the energy required to form one mole of Schottky defects.

By substituting Eqn. 1.18 in Eqn. 1.17, we obtained the expressions for conductivity and is given by

$$\sigma = n_{\max} (Ze) \mu_{\max} e^{-(E_m + E_f/2)/k_B T} \quad (1.19)$$

From eqn. 1.19, it is understood that high conductivity is obtained when $(E_m + E_f/2)$ is small and when n_{\max} and μ_{\max} are as large as possible in solid materials. A low E_a value is obtained when every individual move of mobile ions lead them to sites energetically equivalent to the initial sites [45].

Consequently, if two carriers of identical charges are present in equal concentrations, it would be their mobilities that would decide which mode of charge transport would dominate. In oxide materials, the mobilities of electrons are approximately 10^2 to 10^3 times greater than those of ions, and therefore, a relatively small concentration of electrons can have large effect on the total conductivity. The fraction of total current carried by any mobile

species is called the transport number of that species. The ionic transport number (t_{ion} , expressed as t_+ or t_-) is defined as

$$t_{ion} = \frac{\sigma_{ion}}{\sigma_{ion} + \sigma_{electron}} \quad (1.20)$$

For a good solid electrolyte, t_{ion} should be > 0.99 ; whereas the contribution from all other mobile species should be < 0.01 . The transport number of a species can change upon the temperature and pressure (*e.g.* the partial pressure of oxygen in case of oxide ions).

1.7.4.4 Criteria for solid state ionic conductivity

A large value of the pre-exponential factor and a low value of the activation energy ensure high ionic conductivity. The structural characteristics favoring high ionic conductivity at temperatures well below the melting point of the materials are:

1. A large number of mobile ions,
2. A large numbers of voids (“open” structure),
3. Nearly equal potential energy for the occupied and vacant lattice sites. William van Gool proposed that, and
4. A rigid structure constituted by small polyhedra of highly charged ions (covalently bonded metal-nonmetal system) which is permeated by 2-D channels or 3-D tunnels through which the ionically bonded mobile species can migrate.

1.7.4.5 Methods of measuring ionic conductivity

Ionic conductivity of the materials was measured either by DC methods or by AC methods / Impedance measurement.

1.7.4.5.1 DC methods

Ideally, DC conductivity of the samples should be measured in order to make sure that the measured values pertain to the long range migration of ions, and not to any dielectric

losses associated with the localized rattling of ions within the cages in the structure. It did not quantify the capacitance effect present in the materials. However, the difficulty in making DC measurements is in finding an electrode material that does not give polarization effects at the electrode-electrolyte interface. Therefore DC methods are incapable of separately indicating the grain interior and grain boundary conductivities of the polycrystalline materials.

1.7.4.5.2 AC methods

By using AC-impedance method, the above are often resorted to [45]. DC conductivity values can be extracted from AC data collected over a wide range of frequencies at various temperatures. In favorable cases, it is possible to obtain information on the grain interior and grain boundary resistances and capacitances; electrode resistances and capacitances; and the amount of electrical conductivity present. AC measurements are usually carried out by a Wheatstone bridge concept in which the sample resistance and capacitance are balanced against variable resistors and capacitors. There are four basic formalisms that can be used to represent and analyze AC data which are complex resistance, complex admittance, complex permittivity and complex electric modulus. The details of complex plane impedance analysis are discussed in Chapter 2.

In both AC and DC measurements, in addition to normal two-probe arrangement, special electrode arrangements like three-probe and four-probe methods can be employed in order to eliminate high conduction paths along the surface and the effect of electrode-electrolyte contact resistance [47].

1.8 Scope of the present studies

Apatite ceramic matrices are capable of immobilizing various cations (alkali, alkaline earth *etc.*) and anions (Cl^- , F^- *etc.*) into its crystal lattice and stable upto very high temperature. The special feature of apatite is that it can immobilize volatile fission products into its crystal lattice at low temperature. Apatite can also immobilize rare earths, Mo, Tc elements into its crystal lattice at low temperature. Since the immobilization is carried out at low temperature, it is easy to handle the process and also the process becomes cost effective. The use of apatite glass-ceramics for the immobilization of wastes can increase the amount of waste loading. The apatites bind highly soluble chlorides fission products into its lattice at room temperature and further on treating with glass forming agents they form glass-ceramic matrices. The glass-ceramic matrices can take up more waste loading by distributing the waste elements in crystalline as well as glass phase in intimate contact. The thesis, describes the detailed experimental procedures for the preparation of glass-ceramic composites and their characterization by various techniques. Leaching studies were carried to examine the chemical durability of the composites at extreme conditions. Thermal expansion of the composites was measured by HTXRD and dilatometry. Heat capacity was measured by drop calorimetry and DSC up to 773 K. Glass transition temperature (T_g) of the composites was determined from DSC, Dilatometry (Thermo-Mechanical Analysis) and electrical conductivity studies. The measurement of thermo-physical properties of the waste loaded glass-bonded chloroapatite composites containing pyrochemical waste is reported for the first time.

References:

1. W. Lutze, R. C. Ewing, Radioactive waste forms for the future, In editor: Elsevier Science publishing Company, Inc. Amsterdam, North Holland.
2. "Radiation Protection"- https://en.wikipedia.org/wiki/radiation_protection, 1st June, 2016 at 08:55h.
3. "Radioactive waste management"- www.uic.com.au/wast.html, 15th March, 2016 at 06:55h.
4. K. Raj, K. K. Prasad, N. K. Bansal, Radioactive waste management practices in India, Nucl. Engg. Design, 236 [7-8] (2006) 914-930.
5. A. E. Ringwood, F. R. S. Kelly, P. M. Kelly, Immobilization of high-level waste in ceramic waste forms, Phil. Trans. R. Soc. Lond. A, 319 (1986) 63-82.
6. "Fission products (by element)", [https://en.wikipedia.org/wiki/Fission_products_\(by_element\)](https://en.wikipedia.org/wiki/Fission_products_(by_element)), 6th April, 2016 at 06:15h.
7. M. I. Ojovan, W. E. Lee, An introduction to nuclear waste immobilization, Elsevier, University of Sheffield, Sheffield, England, 2005.
8. G. Leturcq, A. Grandjean, D. Rigaud, P. Perouty, M. Charlot, Immobilization of fission products arising from pyrometallurgical reprocessing in chloride media, J. Nucl. Mater. 347 (2005) 1-11.
9. C. Y. Chan, Radioactive waste management: an International perspective, IAEA Bulletin, March, 1992.
10. K. Raj, M. S. Sonavane, R. G. Yoetikar, Recent developments in the treatment of Radioactive Waste, NUCAR, 1995.

11. I N Donald, Book on Waste Immobilization in Glass and Ceramic based Hosts, Wiley, 2009.
12. S. Priebe, The ceramic Waste Form Process at Idaho National Laboratory, Int. conference on incineration and thermal treatment technologies, May 2007.
13. I. W. Donald, B. L. Metcalfe, S. K. Fong, L. A. Gerrard, D. M. Strachan, R. D. Scheele, A glass-encapsulated calcium phosphate wasteform for the immobilization of actinide-, fluoride-, and chloride-containing radioactive wastes from the pyrochemical reprocessing of plutonium metal, J. Nucl. Mater. 361 (2007) 78-93.
14. A. K. De, B. Lucksheiter, W. Lutze, G. Malow, E. Schiewer, Development of glass ceramics for the incorporation of fission products, Ceramic Bulle. 55 (1976) 500.
15. M. I. Kay, R. A. Young, A. S. Posner, Crystal Structure of Hydroxyapatite, Nature, 204 (1964) 1050-1052.
16. H. G. McCann, The solubility of fluoroapatite and its relationship to that of calcium fluoride, Archives of Oral Biology, 13 [8] (1968) 987-1001.
17. H. McDowell, T. M. Gregory, W. E. Brown, Solubility of $\text{Ca}_5(\text{PO}_4)_3\text{OH}$ in the System $\text{Ca}(\text{OH})_2\text{-H}_3\text{PO}_4\text{-H}_2\text{O}$ at 5, 15, 25, and 37°C, J. Research of the National Bureau of Standards - A. Physics and Chemistry Vol. 81A, Nos. 2 & 3, March – June, 1977.
18. E. C. Moreno, T. M. Gregory, W. E. Brown, Preparation and Solubility of Hydroxyapatite, J. Research of the National Bureau of Standards - A. Physics and Chemistry Vol. 72A, No. 6, November – December, 1968.
19. J. A. Dean, The Analytical Chemistry Handbook, New York: McGraw Hill, Inc. ISBN 0-07-016197-6, 1995, pp. 15.1–15.5.

20. E. Pungor, A Practical Guide to Instrumental Analysis, Florida: Boca Raton, 1995, pp. 181–191.
21. M. J. O'Neill, The Analysis of a Temperature-Controlled Scanning Calorimeter, Anal. Chem. 36 [7] (1964) 1238–1245.
22. D. A. Skoog, F. J. Holler, T. Nieman, Principles of Instrumental Analysis (5th Edi.), New York, ISBN 0-03-002078-6, 1998, pp. 805–808.
23. D. K Agarwal, C. Y Huang, H. A. McKinsty, NZP: A new family of low-thermal expansion materials, Int. J. Thermophys. 12 (1991) 697-710.
24. H. D. Megaw, crystal structures: A working approach, W.B. Saunders Publishing Company, Philadelphia, 1973, pp.422.
25. R. M. Hazen, L. W. Finger, Comparative crystal chemistry, John Wiley & Sons, Chichester, 1982, pp.125.
26. J. G. Collins, G. K. White, Thermal expansion of solids, Prog. Low. Temp. Phys. 4 (1964) 450-479.
27. G. K White, Thermal expansion of solids: A review, High temperatures-High Pressures, 18 (1986) 509-516.
28. R. S. Krishnan, R. Srinivasan, S. Devanarayanan, Thermal expansion of crystals, Pergamon Press, Oxford, 1979.
29. H. J. Mattzke, The science and Engineering – a first course, Prentice Hall of India, New Delhi, 1989.
30. F. S. Lau, Radioactivity and Nuclear waste disposal, Research studies press Limited, Letchworth, 1987, pp. 359.

31. R. Körner, M. Ricken, J. Nötling, I. Riess, Phase transformations in reduced ceria: Determination by thermal expansion measurements, *J. solid state chem.* 78 (1989) 136-147.
32. S. Rangaswamy, S. Safai, H. Herman, In "Thermal expansion – 8", T. A. Hahn (Ed.), Plenum press, 1984, pp. 93.
33. H. Nagamoto, I. Mochida, K. Kagotani, H. Inoue, Change of thermal expansion coefficient and electrical conductivity of $\text{LaCo}_{1-x}\text{M}_x\text{O}_3$ (M = Fe, Ni), *J. Mater. Res.* 8 [12] (1993) 3158-3162.
34. H. P. Kirchner, Thermal Expansion Anisotropy of Oxides and Oxide Solid Solutions, *J. Am. Ceram. Soc.* 52 [7] (1969) 379-386.
35. I. E. Campbell, E. M. Sherwood (Eds.), High temperature materials and Technology, John Wiley & Sons, London, 1967, pp. 890.
36. J. B. Al-Dabbagh, I. K. Al-Faluji, Y. B. Hashim, Thermal Expansion in Ferromagnetic Fe-Ni INVAR Alloy, *Int. J. Engg. Sci.* ISSN: 2278-4721, 1 [1] (2012) 48-51.
37. T. G. Kollie, D. L. McElroy, J. T. Hutton, W. M. Ewing, In "Thermal expansion-1973", edited by R. E. Taylor, G. I. Denman, AIP, New York, 1974, pp. 129.
38. M. E. Brown, Introduction to Thermal Analysis: Techniques and Applications, Chapman and Hall, New York, 1988, pp. 25-63.
39. S. Chandra, Superionic solids, North-Holland, Amsterdam, 1981.
40. P. Hagenmuller, W. Van Gool (Eds.), Solid Electrolytes, Academic press, New York, 1978.
41. P. Vashishta, J. N. Mundy, G. K. Shenoy (Eds.), Fast ion transport in solids, Elsevier, North-Holland, New York, 1979.

42. A. L. Laskar, S. Chandra (Eds.), Superionic solids and solid electrolytes, Academic press, Boston, 1989.
43. T. Takahashi (Ed.), High conductivity solid ionic conductors, World scientific, Singapore, 1989.
44. P. Hagemuller, In "Superionic solids and solid electrolytes", edi. by A. L. Laskar, S. Chandra, Academic press, Boston, 1989.
45. W. V. Gool, Structural aspects of anomalously fast ionic conductivity in solids, J. Solid State Chem. 7 [1] (1973) 55-58.
46. A. R. West, Solid state chemistry and its applications, John Wiley & Sons, Chichester, 1984, pp. 479.
47. R. A. Rapp, D. A. shores, In "Physicochemical measurements in metals research", Part-2, R. A. Rapp (edi.), Interscience, New York, 1970, pp. 135.

EXPERIMENTAL

2.1 Introduction

This chapter deals with the procedures and techniques used for the preparation of the glass bonded composites. Detailed description of the chemicals / reagents used for the preparation, instrumental techniques and principles of various experimental methods used for the characterization of the strontium chloroapatites and its glass-bonded composites has been given. These synthesized products were characterized by powder X-ray diffraction (XRD) and thermal analysis such as Thermogravimetry Analysis (TGA) -Differential Thermal Analysis (DTA), Scanning Electron Microscopy (SEM) - Energy Dispersive X-ray Analysis (EDAX). The chemical stability / leaching behavior of the matrices were studied by Static method (hydrothermal / autoclave technique) and dynamic methods (Sohxlet method). High temperature X-ray diffractometry was used to measure the thermal expansion of chloroapatites and its glass-bonded composites. The thermal expansion of these composites was also measured by Thermomechanical Analysis (TMA) / Dilatometry. Thermophysical properties such as thermal expansion, glass transition temperatures, heat capacity and electrical conductivity were also measured by various experimental techniques like Differential Scanning Calorimetry (DSC), Drop calorimetry, AC-impedance measurement. These experimental methods are discussed in this chapter.

2.2 Chemicals and Reagents

All the chemicals and reagents used in this study were easily available and low cost. The list of chemicals used was given below in Table 2.1.

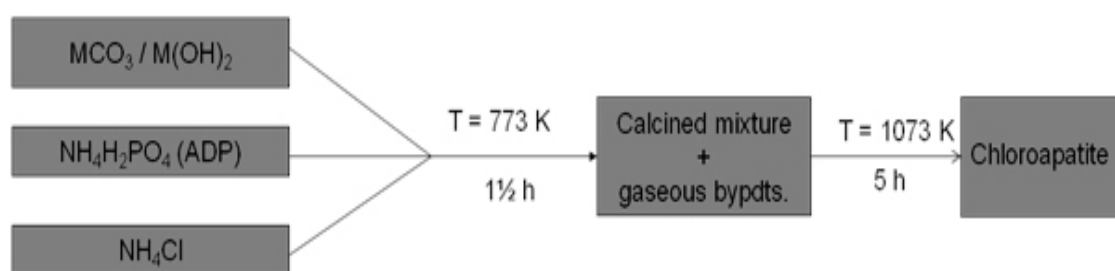
Table 2.1: Chemicals name, formula, company name

Ser. no.	Chemicals name	Formula	Company name
1.	Strontium carbonate	SrCO_3	Sigma-Aldrich
2.	Ammonium dihydrogen phosphate	$\text{NH}_4\text{H}_2\text{PO}_4$	sd fine Chem. Limited
3.	Ammonium Chloride	NH_4Cl	-do-
4.	Silicon dioxide, extra pure	SiO_2	Albert Vector
5.	Boron trioxide	B_2O_3	sd fine Chem. Limited
6.	Sodium carbonate	Na_2CO_3	-do-
7.	Sodium chloride	NaCl	-do-
8.	Lithium chloride	LiCl	Sigma-Aldrich
9.	Potassium chloride	KCl	Central Drug House, New Delhi
10.	Cesium chloride	CsCl	Alfa-Aesar
11.	Barium chloride	$\text{BaCl}_2 \cdot 2\text{H}_2\text{O}$	Burgoyne-Burbidges & Co, Mumbai
12.	Neodymium chloride	NdCl_3	Sigma-Aldrich
13.	Cerium chloride	CeCl_3	Sigma-Aldrich
14.	Aluminium oxide	Al_2O_3	E. Merck
15.	Potassium carbonate	K_2CO_3	Sigma-Aldrich
16.	Calcium carbonate	CaCO_3	Burgoyne-Burbidges & Co, Mumbai
17.	Calcium hydroxide	Ca(OH)_2	J. T. Baker Chemicals
18.	Strontium hydroxide	Sr(OH)_2	-do-
19.	Magnesium oxide	MgO	E. Merck

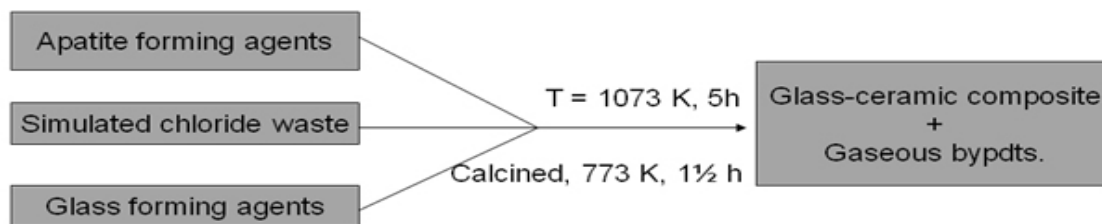
20.	Zirconium oxide	ZrO ₂	NFC, Hyderabad
21.	Barium carbonate	BaCO ₃	E. Merck
22.	Barium hydroxide	Ba(OH) ₂ . 8H ₂ O	AnalaR, Glaxo Laboratory
23.	Lead dioxide	PbO	sd fine Chem. Limited

2.3 Experimental procedure

The chloroapatites and their glass-bonded composites were synthesized by solid state reaction route. In this method, chloroapatites were prepared by taking stoichiometric amounts of MCO₃ / M(OH)₂ (M = Ca, Sr, Ba *etc.*), ammonium dihydrogen phosphate (abbreviated as ADP) and ammonium chloride in a mortar-pestle, mixed well for half an hour to get a homogeneous mixture. The mixture was added with ~ 2-3 ml of acetone and then mixed well until the acetone dried up. The homogeneous mixture was then calcined at 773 K in an alumina crucible for 1½ h so that the gaseous by-products such as ammonia, moisture were removed from that reaction mixture. After that, the calcined mixture was heated to 1073 K / 5h in alumina crucible at air ambience. The products were then characterized by various techniques. The schematic of the preparation flow sheet is shown below



Similarly, the simulated waste loaded glass-ceramic composites were prepared by adding simulated chloride waste and borosilicate glass (abbreviated as BSG) forming reagents with the apatite forming reagents. The flow sheet is given as follows



2.4 Instrumental techniques and principles

2.4.1 X-ray Diffraction (XRD)

X-ray diffraction (XRD) is a non-destructive technique for the quantitative and qualitative analysis of the crystalline materials in the form of powder or solid. It is based on the fact that each crystalline compound crystallizes in a particular crystal structure characteristic of the compound, giving rise to a unique X-ray diffraction pattern.

2.4.1.1 X-ray Generation and properties

X-rays are electromagnetic radiation with typical photon energies in the range of 100 eV - 100 keV. For diffraction applications, only short wavelength X-rays (hard X-rays) in the range of a few angstroms (1 keV) are used [1-4]. Because the wavelength of x-rays is comparable to the size of atoms, they are ideally suited for probing the structural arrangement of atoms and molecules in a wide range of materials. The energetic X-rays can penetrate deep into the materials and provide information about the bulk structure.

X-rays are produced generally by either X-ray tubes or synchrotron radiation. In a X-ray tube, which is the primary X-ray source used in laboratory X-ray instruments, X-rays are generated when a focused electron beam accelerated across a high voltage field bombards a stationary or rotating solid target. As electrons collide with atoms in the target and slow down, a continuous spectrum of x-rays are emitted, which are termed ***Bremsstrahlung radiation***. The high-energy electrons also eject inner shell electrons in atoms through the

ionization process. When a free electron fills the shell, an X-ray photon with energy characteristic of the target material is emitted. Common targets used in x-ray tubes include Cu and Mo, which emits 8 keV and 14 keV X-rays with corresponding wavelengths of 1.54 Å and 0.8 Å, respectively. (The energy E of an X-ray photon and its wavelength is related by the equation, $E = hc/\lambda$, where h is Planck's constant and c the velocity of light).

2.4.1.2 XRD Equipment

In this study, the heat treated pellet was ground well to a fine powder in a mortar and pestle for half an hour and a small amount of the powder was placed on a zero background single crystal quartz plate and made as a thin paste using organic liquid. The plate was mounted in the sample holder and fixed with colodion. The phase formation and the crystal structure of the products have been investigated by employing a PANalytical X'Pert powder diffractometer using Cu- K_α radiation monochromatized by a curved graphite crystal placed in front of the NaI (Tl) scintillation detector. Scans were made in the 2θ range of 10 - 80 deg. with a scan rate of 0.05 deg. per second and a counting time of six second per step. In order to eliminate systematic errors in the scattering angles, the observed angles were corrected with those obtained with Si standard.

The scintillation detector is the most common detector used which utilizes the ability of X-rays to cause certain substances to fluoresce in visible light. The amount of light emitted is proportional to the X-ray intensity and can be measured by means of a phototube. Since the amount of light emitted is small, a special kind of phototube called photo multiplier has to be employed in order to get a measurable current output. The substance generally used to detect X-rays is NaI crystal activated with small amount of thallium. It emits blue light under X-ray bombardment. The light, which causes the ejection of the electrons, is transmitted to

the photo cathode of the photomultiplier tube. These electrons are then permitted to strike the first dynode of the tube. There is multiplication at each dynode, and the resulting multiplication can reach well in excess of 10^6 and are finally collected at the anode. The current pulse is amplified and fed through an analyzer or discriminator to a scalar and / or rate meter. The XRD instrument used for the characterization purpose is shown in Fig. 2.1.



Fig. 2.1: PANalytical X'Pert powder diffractometer for XRD measurement

2.4.1.3 Powder X-ray Diffraction

Powder XRD (X-ray Diffraction) is perhaps the most widely used x-ray diffraction technique for characterizing materials. As the name suggests, the sample is usually in a powdery form, consisting of fine grains of single crystalline material to be studied. The technique is also used widely for studying particles in liquid suspensions or polycrystalline solids (bulk or thin film materials).

The term 'powder' really means that the crystalline domains are randomly oriented in the sample. Therefore when the 2-D diffraction pattern is recorded, it shows concentric rings of scattering peaks corresponding to the various d -spacing in the crystal lattice. The positions

and the intensities of the peaks are used for identifying the underlying structure / phase of the material. For example, the diffraction lines of graphite would be different from diamond even though they both are made of carbon atoms. This phase identification is important because the material properties are highly dependent on structure.

Powder diffraction data can be collected using transmission or reflection geometry, as shown in Fig 2.2, because the particles in the powder sample are randomly oriented, these two methods will yield the same data.

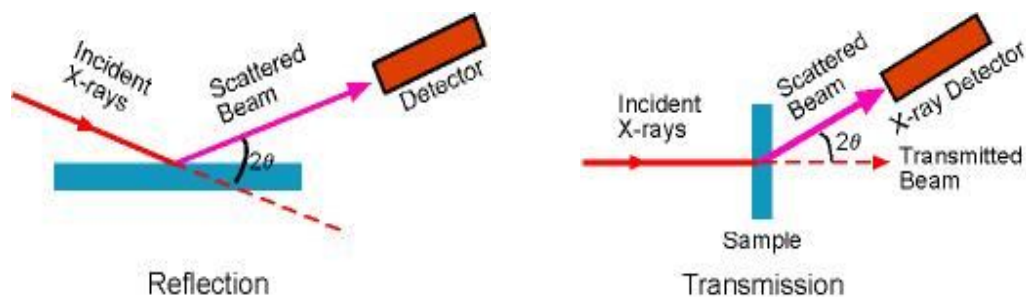


Fig. 2.2: Reflection and Transmission geometry in XRD

2.4.1.4 Bragg's Law

The Bragg law embodies the principle of X-ray diffraction analysis, it allows us to make accurate quantification of the results of experiments the carried out to determine crystal structure. It was formulated in 1912 by W. L. Bragg, in order to explain the observed phenomenon that crystals only reflected X-rays at certain angles of incidence. X-rays primarily interact with electrons in atoms. When X-ray photons collide with electrons, some photons from the incident beam will be deflected away from the direction where they originally travel, much like billiard balls bouncing off one another. This phenomenon is called *Scattering*.

If the wavelength of these scattered X-rays did not change the process is called elastic scattering (Thompson scattering) in that only *momentum* has been transferred in the scattering process. These are the X-rays that we measure in diffraction experiments, the scattered X-rays carrying information about the electron distribution in materials. The superposition of the waves scattered by individual atoms will result in diffraction. The x-rays scattered from the atoms of a crystal combine in an additive way in certain direction, and this is called *coherent scattering or X-ray diffraction*. On the other hand, in the inelastic scattering process (Compton scattering), X-rays transfer some of their energy to the electrons and the scattered X-rays will have different wavelength than the incident X-rays.

The concept used to derive Bragg's law is very similar to that used for the Young double slit experiment. When X-rays incident upon a sample, they will either be transmitted, or scattered by the electrons of the atoms in the material (Fig. 2.3). All the atoms in the path of the X-ray beam scatter X-rays. In general, the scattered waves destructively interfere with each other, with the exception of spatial orientations at which Bragg's law is satisfied (Bragg angles).

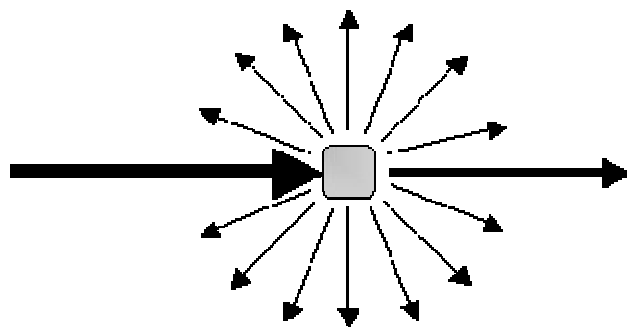


Fig. 2.3: Interaction of X-rays with matter

Consider a simple crystal such as illustrated in (Fig. 2.4), with lattice planes separated by a distance d_{hkl} . As illustrated above the scattered X-rays from this crystal will travel in random directions.

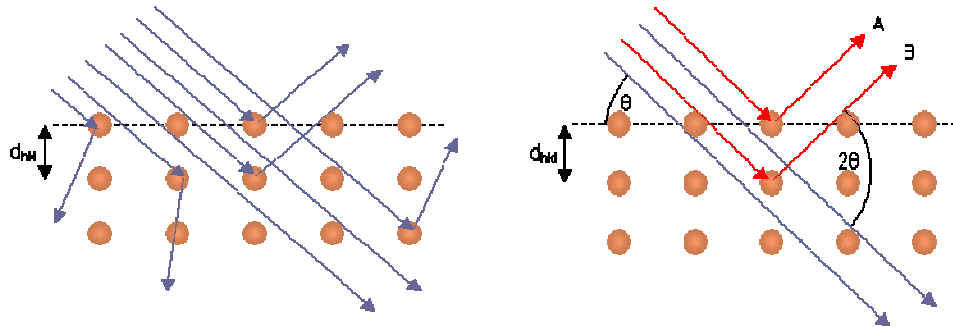


Fig. 2.4: Incidence and diffraction of x-rays on to the lattice

The Bragg condition is such that the scattered rays from two parallel planes interact with each other in such a way as to create constructive interference. For this to happen the extra distance travelled by ray C' as shown in (Fig. 2.5) must be an integral multiple of the wavelength of the radiation. This means that the crests and troughs of each wave are aligned with each other (coherence).

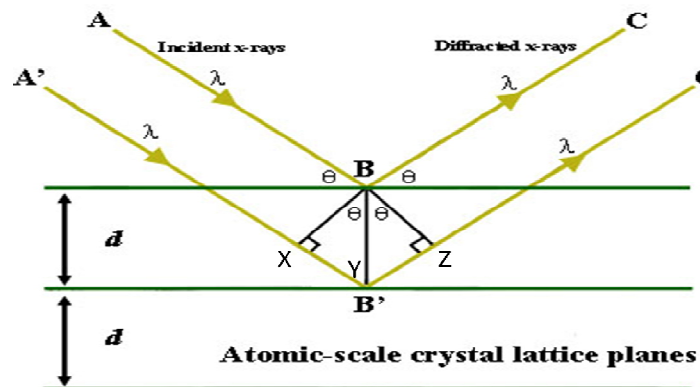


Fig. 2.5: schematic of diffraction from parallel plane of a crystal

The geometry of the Bragg condition is remarkably simple, and leads to the powerful result of the Bragg law: The extra distance that ray C' must travel is the distance $X-Y-Z$.

Thus,
$$X-Y-Z = n \lambda \quad (2.1)$$

But,
$$X-Y = Y-Z = d \sin \theta \quad (2.2)$$

Hence,
$$n \lambda = 2 d \sin \theta \quad (2.3)$$

This is the Bragg's law of XRD.

In order to consider the general case of hkl planes, the equation can be rewritten as:

$$\lambda = 2 d_{hkl} \sin \theta_{hkl} \quad (2.4)$$

Since, the d_{hkl} incorporates higher orders of diffraction i.e. n greater than 1.

2.4.1.5 High Temperature X-ray powder Diffractometry

This is a powerful technique to study the changes occurring in crystal structures at high temperatures in solids [4-5]. The classical method of studying such transformations, like quenching to low temperatures and characterizing the structure at room temperature assuming retention of the high temperature phase at the room temperature, will not help when the structural changes takes place very fast. In situ X-ray diffraction analysis will be highly beneficial in such cases. By measuring the unit cell dimensions as a function of temperature, the thermal expansion coefficients of the materials can also be measured by this technique. Electrical resistive heating is commonly employed method to heat the samples at higher temperature in this technique.

2.4.1.5.1 Experimental Set-up

The schematic diagram of a commercial high temperature X-ray powder diffractometer is shown in Fig. 2.6. The high temperature attachment is mounted on the

vertical goniometer of an X-ray diffractometer. The high temperature stage consists of a cylindrical one end closed, double-walled brass chamber provided with a long beryllium window on the body of the incidence and emergence of X-ray in the 2θ range of $0 - 180^\circ$. The powder sample is placed as a thin layer flat strip of a refractory metal like tungsten or molybdenum, which is connected to two electrodes. The sample carrier strip is subjected to electrical resistance heating at programmed rates. The surroundings of the sample are also heated by another resistor so that the radiative heat losses from the sample will be minimized. The cooling water was circulated through the annular space between the chamber walls and also through the electrodes. Temperature measurement was carried out by means of a thermocouple at the back of the sample carrier strip. The thermocouple output is also used to control the supply of current to the heating strip so as to keep the sample temperature profile coincident with the temperature programmed function. The thermocouple and electrodes connections enter the chamber through high vacuum-tight feed-through points on the chamber flange so that heat can be carried out in a high vacuum atmosphere. The flange carrying the electrodes was held in a position on the chamber by means of two guided pins, so that the samples always remain on the focusing circle of the diffractometer.

2.4.1.5.2 X-ray Diffraction at high temperatures

The x-ray diffraction patterns of a substance at higher temperatures would be different than that of at the room temperature even though there is no phase change occurring during the experiment. This is due to the increase in interplanar spacings at higher temperatures (expansion of crystal lattice of a material), the diffraction angle shift to lower values and also decreased in intensity due to the increase in vibration of the lattice at higher temperatures. Although, there will be an increase in background level due to the thermal

diffusion scattering. Due to thermal diffuse scattering, some general coherent scattering occurs in all directions. This may be attributed to the fact that with increase in temperature, the lattice vibration increases; the crystal becomes less and less ideal leading to the contribution of the non-Bragg's angle towards the intensity at higher temperatures.

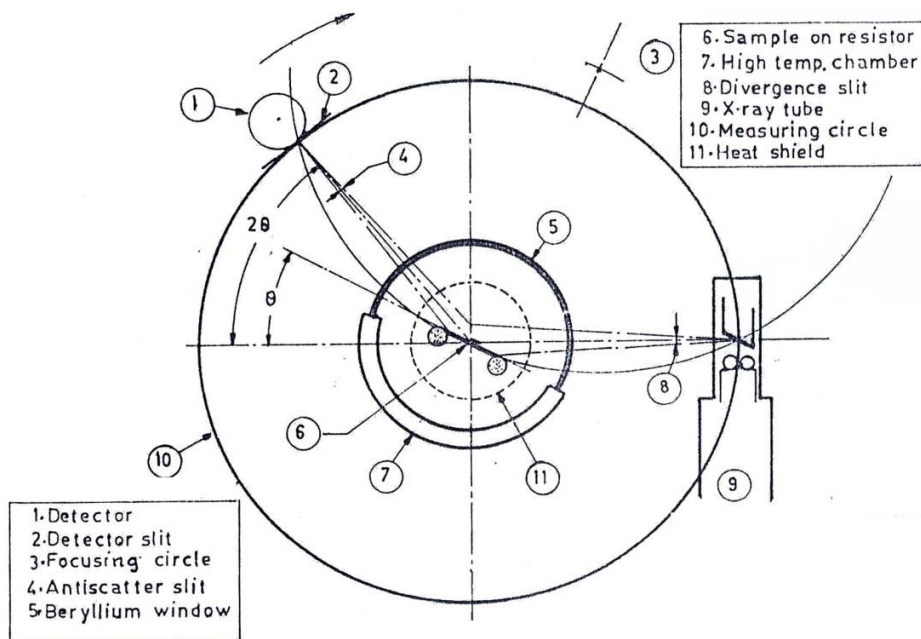


Fig. 2.6: schematic of X-ray diffraction geometry including the high temperature measurement attachment

2.4.1.5.3 Thermal expansion measurement by high temperature XRD (HTXRD)

The interatomic equilibrium distance in a substance increases with the increase in temperature due to the anisotropic anharmonicity in lattice vibrations. This change in interatomic distances will be manifested in the lattice parameters. Thereby, thermal expansion coefficient of such crystalline materials can be derived by measurement of lattice parameters as a function of temperature. This technique is popularly known as micro method of thermal expansion. In this method, XRD diffraction patterns need to record accurately and from these data's, the precise lattice parameters can be calculated by any standard methods or

by any standard software package application. The coefficient of thermal expansion (α) in various directions (x, y, z) can be calculated by using the expression

$$\alpha = \frac{1}{l} \cdot \frac{dl}{dT} \quad (2.5)$$

Where, l = the lattice parameter at RT and dl/dT = the change in lattice parameter with respect to T of l vs. T curve.

The main advantage of this method of thermal expansion measurement is that a few mg of sample is enough to carry out the experiment and it will give coefficient values for all the direction of least symmetric crystals. The details of advantages of micro method vs. macro methods were already discussed in chapter-1.

The calibration of a high temperature x-ray diffractometer was done by using standard samples like ThO_2 , MgO . The experiments were carried out with these standard samples and the % measured thermal expansions were found to be good in agreement with that reported in the literature. The temperature calibration in the high temperature chamber was also performed by monitoring the melting temperature of Au as indicated by sudden degradation of its sharp diffraction pattern upon melting [6].

2.4.2 Thermal Analysis

Thermal analysis is the study of various properties of materials as they change with temperature. Several methods are commonly used - these are distinguished from one another by the property which is measured:

2.4.2.1 Thermogravimetric Analysis (TGA) [7]

Thermogravimetry is a technique of monitoring the change in mass of a sample as a function of temperature or time (at constant temperature). Mass-loss due to dehydration or decomposition can be accurately followed by this technique. The empirical chemical formula

can be determined from the data when combined with the evolved gas analyses. The basic instrumental requirement for thermogravimetry is a precision balance with a furnace programmed for a linear rise of temperature. In the present studies, dynamic thermogravimetric curves were obtained by plotting mass-loss as a function of temperature. The mass-loss was further examined by heating the samples at RT – 1273 K temperature range in air / Ar atmospheres at a heating rate of 5 K/min or 10 K/min.

2.4.2.2 Differential Thermal Analysis (DTA) [7]

Differential thermal analysis (DTA) on the other hand measures the differential temperature between the sample and reference material, both of which are heated under identical conditions. The reference material used is thermally inert $\alpha\text{-Al}_2\text{O}_3$. The thermocouple output in μV is plotted as a function of temperature. A positive value of ΔT indicates exothermic reaction and the negative value indicates endothermic reaction.

2.4.2.3 Differential Scanning Calorimetry (DSC)

Differential Scanning Calorimetry (DSC) is a versatile technique of thermal analysis in which the sample and a reference material are subjected to a continuously increasing programmed temperature of uniform heating / cooling. Heat is added to the sample or to the reference by external means as necessary to maintain the sample as well as the reference at identical temperatures. The added heat, which was recorded, compensates for that lost or gained as a consequence of exothermic (abbreviated as “exo”) or endothermic (abbreviated as “endo”) reactions occurring in the sample. DSC is very much similar to DTA and gives same sort of informations. However, DSC is more often used for quantitative measurements of energy changes, hence the name differential scanning calorimetry. It differs from DTA in that instead of allowing temperature difference to develop between the reference and sample

materials, DSC measures the energy that needs to be applied to keep the temperatures identical [8].

2.4.2.3.1 Experimental set up for DSC measurement

A schematic diagram of a differential scanning calorimeter [9, 10] is given in Fig. 2.7. Likewise in DTA, the sample and the reference in DSC were also provided with individual heaters. It is convenient to think of the system as divided into two control loops [9], as shown in Fig. 2.7a schematically. One is for average temperature control, so that the temperature of the sample and the reference will be increased at a predetermined rate. On the other hand, second loop will adjust the power input to remove the difference, if a temperature difference develops between the sample and the reference due to the exothermicity or endothermicity in the sample. This is called the null balance principle. Thus, the temperature of the sample holder is always maintained a constant value as that of reference holder by continuous and automatic adjustment of the heater power. A signal proportional to the difference between the heat input to the sample and that to the reference, dH/dt , was fed into the recorder, which was also used for data acquisition of the average temperature of the sample and reference. Thus, DSC thermogram records the heat flow vs. temperature. One such thermogram was shown in Fig. 2.8 [9, 11]. The area under the peak gives the heat change associated with the physical or chemical change took place in the sample.

2.4.2.3.2 Application of DSC

One of the most important applications is the study of phase transitions and evaluation of phase diagrams. This was also very much useful for the determination of heat capacity and other processes like glass transition temperature (T_g), crystallization, fusion, desolvation, dehydration, adsorption, degradation and solid state reactions. A wide range of

inorganic compounds, ceramic, glass, glass-ceramic, clays, polymers can be studied by this DSC technique.

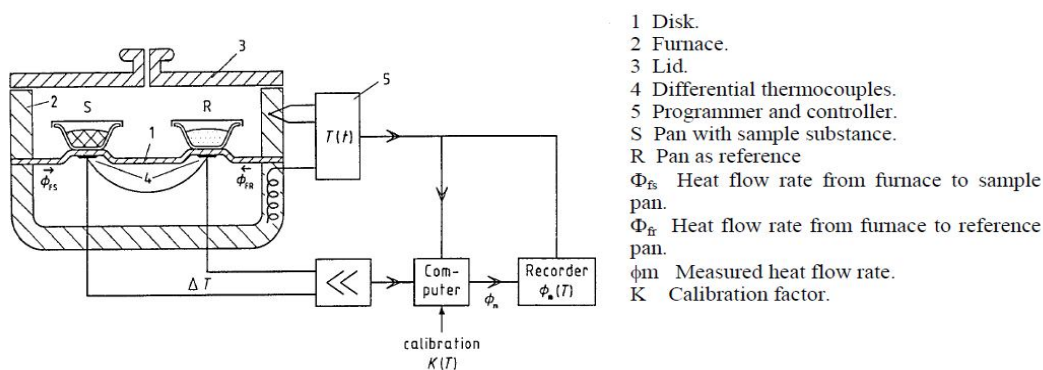


Fig. 2.7: Schematic of a Differential Scanning Calorimeter

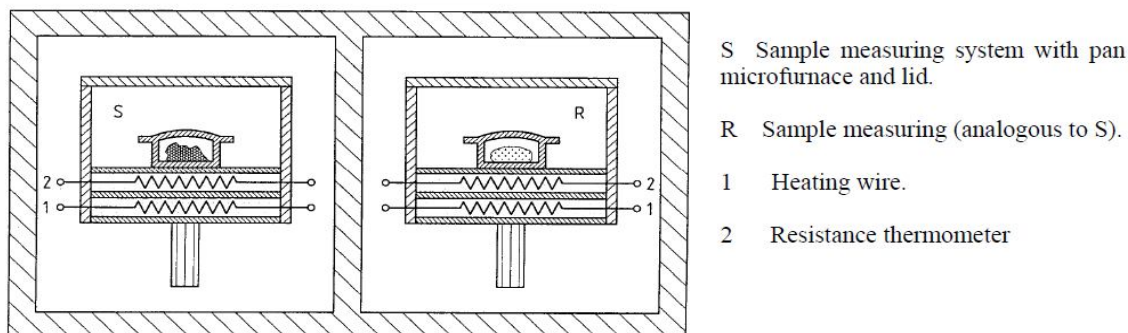


Fig. 2.7a: Temperature control loop where the sample and reference are always kept at same T ; this employs the null balance principle.

The DSC thermogram for a typical organic polymer was shown in Fig. 2.8 [11, 12]. Most of the solids polymers were formed by the quenching from the melt to low temperatures and thus the products will be initially in a glassy state. The transition temperature at which solid glass becomes a rubber like glassy state (glass transition temperature, T_g) is an example of a second order transformation. Such transitions were accompanied with a change in heat capacity, but change in enthalpy ($\Delta H = 0$). The transition thus appears on the DSC as a shift of the baseline to the endothermic peak at the glass

transition temperature (T_g). Afterthat, as the temperature was slowly increased, the polymer may recrystallize (exotherm) before melting (endotherm) occurs. Further, at higher temperatures, the polymer sample may degrade or oxidize depending upon the surrounding atmosphere.

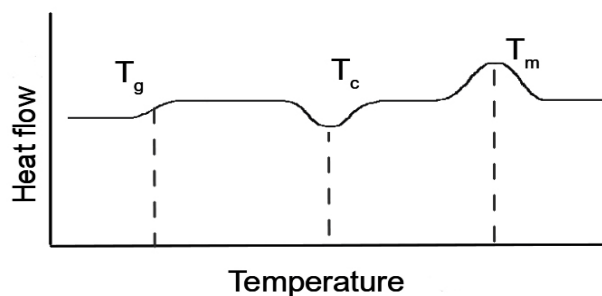


Fig. 2.8: A typical DSC thermogram of polymer sample

2.4.3 Scanning Electron Microscopy (SEM)

Electron microscopes function the same way as their optical (magnification 500x to 1000x) counterparts except that they use a focused beam of electrons instead of light to image the specimen and gain information as to its structure and composition. SEM studies of the materials can provide information on surface texture (topology), morphology (shape, size and arrangement of the particles that are lying on the surface etc.) and composition of the particles on the surface. When the beam strikes the sample and dwells for a few microseconds interactions occur on the sample and are detected. The interactions of the e-beam with sample produce various processes such as (i) back scattering of incident electrons after colliding with an atom in the specimen, (ii) secondary electron emission (iii) X-ray and cathode luminescence (iv) Auger electron emission (v) unscattered electrons (transmitted electrons) *etc.* SEM utilizes the backscattered and secondary electrons to examine the surface of the specimen. These signals are collected and displayed in the monitor after proper amplification and processing. In this study, SEM XL 30, Philips (LaB₆ filament and

resolution 2 nm) was used to examine the surface of the apatite ceramic samples. Energy Dispersive X-ray Spectroscopy (EDAX) was carried out on some of the samples to find out the elemental compositions of the material.

2.5 Leaching studies for chemical durability

Chemical durability (Leaching studies) is one the important pre-requisite that a matrix should satisfy to qualify for a better nuclear waste immobilization host matrix. Higher the durability better would be its resistance to retain all the radioactive elements in its structure. Leaching studies of these glass-ceramic composites were carried out in two different methods, (a) Static method by hydrothermal autoclave technique and (b) Dynamic method by Soxhlet measurement.

2.5.1 Static method by hydrothermal Autoclave technique

About 1gm of each powder sample were taken in teflon cell, added 10 ml of deionized water. The cell was then closed by using the teflon lid. Then the teflon cell was put into an autoclave. The autoclave was then heated to 423 K for 1 day in a PID controlled furnace at air ambience. After the heating the autoclave was taken out from the furnace and the decanter was filtered by using Whatman 42 filter paper. The filtrate solution was collected in a 100 ml volumetric flask and made upto 100 ml by adding distilled water. The filtered solution was then analyzed by AAS for alkali and alkaline earth elements; ICP-OES for rare earth elements and Ion Selective Electrode for Cl.

2.5.2 Dynamic method by Soxhlet measurement

In the soxhlet method, 500 ml of de-ionized water is taken in the round bottom flask and is heated at 373 K on a heating mantle. The apparatus used for soxhlet measurement was given in Fig. 2.9. The pellet / powder sample was kept in a small bucket / cup like structure

above the water level in the round bottom flask as shown in Fig. 2.9. The round bottom flask was heated by a heating mantle controlled by a temperature controller. The water boils and the vapour condenses at the top of the condenser. This condensed water (fresh water) falls on the sample that is kept in the bucket with a flow rate of (0.4 - 0.5) litre / day, thereby simulating an infinitely dilute condition. After 24 – 48 hours, 30 ml of the leachate is pipetted out for the analysis and replaced by fresh 30 ml of de-ionized water, so that the total volume of leachate always remains a constant. The experiment is carried out continuously upto a maximum number of 28-30 days for all the compounds synthesized. The leachate solutions were then analyzed by AAS for alkali and alkaline earth elements; ICP-OES for rare earth elements and Ion Selective Electrode for Cl.



Fig. 2.9: Apparatus set-up of Soxhlet measurement for leaching studies

The Normalised Leach Rate (NLR, in $\text{g cm}^{-2} \text{d}^{-1}$) for each element was calculated from the Leachate concentration of the species such as Cl, Li, Na, K, Cs, Sr, Ba, Nd, Ce *etc*, for every compositions / composite as stated previously by using the following equation [13, 14].

$$\text{NLR} = (A_i \times V) / (f_i \times S \times t) \quad (2.6)$$

Where, A_i = concentration of the leachate i^{th} species ($\mu\text{g/ml}$ or *ppm*), V = volume of distilled water taken for analysis (ml), f_i = mol fraction of i^{th} element/species, S = surface area (cm^2) and t = time (d).

2.6 Thermal expansion Measurement by Thermomechanical method (Dilatometry)

Thermal expansion measurements of glass-ceramics sintered bulk pellets around 10 mm dia. and 10 mm height were carried out by dilatometry in the temperature range 298–900 K in air, by using a home-built apparatus [15, 16]. Linear Variable Differential Transformer (LVDT) was used as the displacement sensor. The instrument was calibrated by measuring % thermal expansion of known standard single crystal of MgO [17] and ThO₂ pellets [18]. The experimentally measured value of MgO was interpolated at 2 K interval and plotted against temperature. The % thermal expansion was fitted to a polynomial equation of 3rd order. The % expansion obtained at various temperatures by using literature data and experimental data are compared within the measured temperature range. The difference in % thermal expansion reported in the literature (fitted value of equation reported in the literature) and experimentally measured for MgO is added to the experimentally measured value of ThO₂. The corrected value of ThO₂ is compared with the ThO₂ literature value by Belle and Berman [19]. The following equations (eqn. 2.7 and 2.8) are used to find out the corrected value of ThO₂ using MgO as the standard.

$$\text{MgO correction value} = \% \text{ expansion of MgO using literature equation} - \% \text{ expansion experimental value of MgO using interpolation} \quad (2.7)$$

MgO corrected % expansion of ThO₂ = Experimental % expansion of ThO₂ + MgO correction value as given in Eqn. 2.7 (2.8)

The MgO corrected ThO₂ value is compared with literature value given by Belle and Berman.

The literature value and corrected values of ThO₂ are found to be in good agreement. Same procedure is applied to cross check the % thermal expansion of MgO by adding difference of ThO₂ (fitted) and ThO₂ experimental and compared with MgO (literature value /fitted). In this study, the difference in fitted value and experimentally measured value of standard MgO single crystal is taken as the correction factor for the samples studied. The densities and dimensions of the pellets were once again measured after the thermal expansion measurements were complete. The dimensions were found to be unchanged. The percentage of average/mean linear thermal expansion is calculated using eqn. 2.9.

$$\% \text{ TE} = (\Delta L/L) \times 100 \quad (2.9)$$

The coefficient of thermal expansion (Average CTE = $\alpha_m = \alpha_{av}$) of the compounds was calculated by using the formula given in eqn. 2.10.

$$\text{Average or mean CTE} = \alpha_m = (\Delta L/L) \times (1/\Delta T) \quad (2.10)$$

Where, ΔL = change in length, L is the length of the pellet, ΔT = change in temperature (K).

2.7 Enthalpy increment Measurement by Drop Calorimetry

The heat capacity is an important thermophysical property [19] of materials. Drop calorimetry is a well known technique of measuring enthalpy increment. These data are routinely utilized in the processing and performance evaluation of materials. Heat capacity

was computed from these enthalpy increment data measured by using drop calorimetric technique.

2.7.1 Description of the Drop Calorimeter

The in-house built drop calorimeter (shown in Fig. 2.10) was used to measure the enthalpy increment of the samples [20, 21]. The calorimeter consists of (1) Furnace with precise temperature controller, (2) Sample dropping assembly, (3) Calorimetric vessel assembly containing sensitive heat flow sensor, (4) Chilled water circulation and temperature measurement facility and (5) Data acquisition, display and analysis system.



Fig. 2.10: Photograph of home-built calorimeter

2.7.2 Enthalpy increment measurement procedure

The specimen usually in the form of small pellet (6 mm dia) is placed inside sample holder situated in uniform hot zone of the furnace. The sample heated to a desired temperature, then dropped in to the calorimetric vessel and the signal is recorded and processed by using a PC. Each drop is stored in a file with a unique name which contains details about sample name, temperature, weight, date, month and year. The sequence of measurement followed was standard, sample and standard. The standard chosen is alumina supplied by NBS, USA. The ASCII data obtained is analyzed through the software “analyze data” to get the area under the curve. One such area under the curve is shown in Fig. 2.11.

The area under the curve is proportional to the enthalpy change associated with the process of cooling of the specimen from higher temperature (T_1) to the temperature T_2 (298 K). The enthalpy increment of the sample is calculated as,

$$\left(H_T^0 - H_{298}^0\right)_{\text{Sample}} = \frac{A_{\text{Sample}}}{A_{\text{Standard}}} \left(H_T^0 - H_{298}^0\right)_{\text{Standard}}$$

Where, A_{sample} and A_{standard} are the area under the curve for the sample and the standard respectively. The measurement is conducted for a minimum of six times at each temperature to check the consistency of the values. The temperature range covered during enthalpy increment measurement is from 323 to 1023 K.

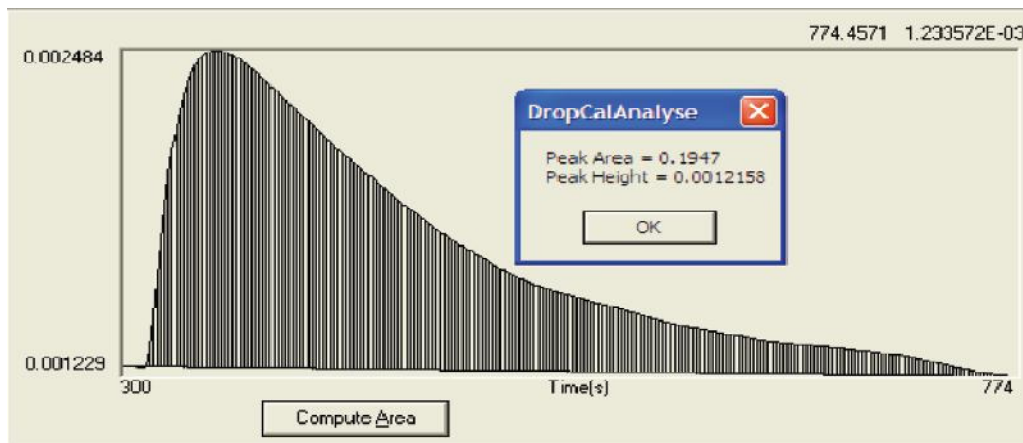


Fig. 2.11: Area under the curve for enthalpy increment measurement

These enthalpy increment data were then fitted to a 4-term equation, $H_T^0 - H_{298K}^0 = a + bT + cT^2 + d/T$ and by using least square method, the coefficients: a, b, c, d can be found out. The heat capacity of the sample was evaluated from the first derivative of the above fitted enthalpy increment equation.

2.8 Electrical conductivity measurements

The electrical conductivity was measured by DC as well as by AC-impedance measurement.

2.8.1 AC impedance spectroscopy

This technique is an important method of measuring the ionic conductivity of materials. Generally, conductivity measurements on ceramic as well as glass were done by using DC methods on the sintered pellets of the samples. However, this method can lead to error in measurement due to the variation in contribution of the grain boundaries and electrodes [22]. The major challenge in making DC measurements is to find electrode materials that are compatible with the solid electrolyte and that do not give polarization effects at the electrode-electrolyte interface throughout the experiment. The conductivity of materials due to the grain interior and grain boundary can vary as the microstructure of a polycrystalline material is greatly influenced by the condition of materials synthesis and fabrication and thereby depend upon the nature of grain boundaries. The DC measurement methods also were incapable to separate the various grain interior contributions towards the conductivity. Electrochemical impedance spectroscopy (EIS) can overcome these difficulties in conductivity measurements. In this method, the electrical impedance of materials is measured within a suitable AC frequency range. From the frequency response spectrum, the grain interior resistance, grain boundary resistance and information on the electrode-electrolyte charge transfer process can be obtained [2, 23].

2.8.2 Analysis of impedance spectrum

In impedance measurement, the imaginary part ($-Z''$) on the complex impedance (Z) of a specimen is plotted against the real part (Z') in the form of Nyquist plot for a wide range of frequency, typically 1 MHz – 1 Hz. The plots may form various combinations of R and C depending upon the materials. One such parallel combination of R and C were in the Fig. 2.12.a. The spectrum consists of three semicircles; the number of such semicircles that can

appear depends on the sample characteristics, temperature and the AC frequency range used. Bauerle *et al.* [24] has analyzed that kind of plot by assigning an equivalent circuit consisting of parallel combinations of resistors (R) and capacitors (C) as shown in Fig. 2.12.b, where each combination gives rise to a different semicircle.

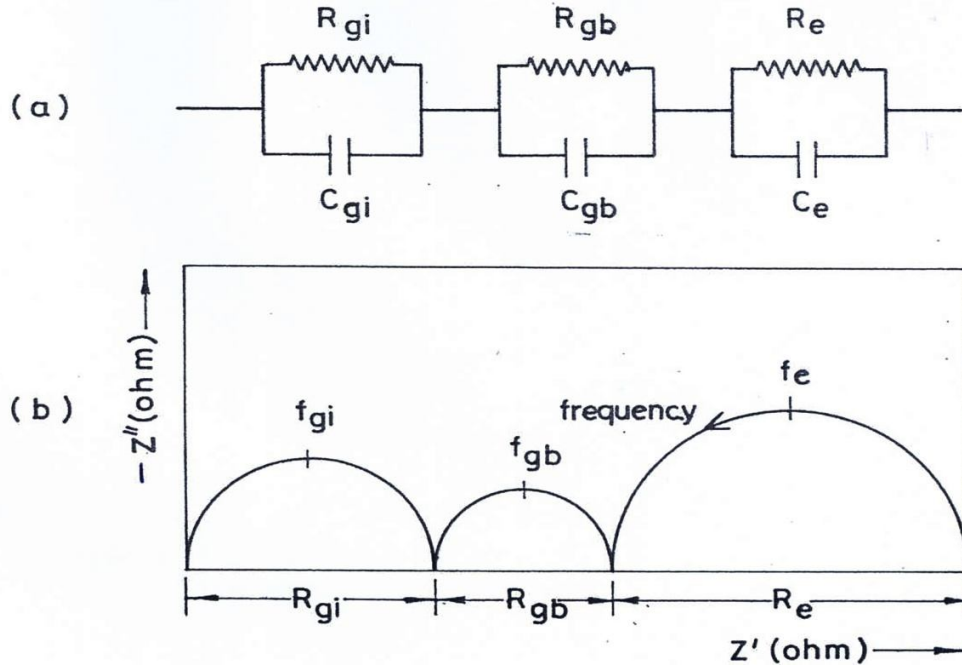


Fig. 2.12.a): Equivalent circuit of a ceramic electrolyte consisting of series combination of parallelly connected resistors (R) and capacitors (C) according to Bauerle. b): Complex impedance plot showing semicircles corresponding to the grain interior (gi), grain boundary (gb) and electrode (e) polarization; f is the relaxation frequency of the process

First, let's focus on a single RC parallel circuit. The current (I) through the resistor (R) under an applied potential (E) is given by ohm's law as

$$I = \frac{E}{R} \quad (2.11)$$

, and this is independent of AC frequency.

The capacitor (C) does not allow the passage of a direct current through it, but it does allow a frequency-dependent AC current, given by the following expression,

$$I = j\omega CE \quad (2.12)$$

Where, ω = the angular frequency ($\omega = 2\pi f$) and $j = \sqrt{-1}$. The current through the capacitor is imaginary and this indicates that there is a phase difference of 90 degree between the sinusoidal current and voltage; by convention, the currents leads to voltage by 90° . Therefore, Eqn. 2.11 and 2.12 can be written as

$$Z = \frac{E}{I} \quad (2.13)$$

Where, Z is the impedance. The total impedance Z^* (which is a complex number) of the RC circuit can be related to R and C by the expression,

$$\frac{1}{Z^*} = \frac{1}{R} + j\omega C \quad (2.14)$$

Therefore,
$$Z^* = \frac{R}{1+(\omega RC)^2} - j \frac{\omega R^2 C}{1+(\omega RC)^2} \quad (2.15)$$

The Eqn. 2.15 can be written in the form,

$$Z^* = Z' - j Z'' \quad (2.16)$$

Where,
$$Z' = \frac{R}{1+(\omega RC)^2} \quad (2.17)$$

and
$$Z'' = \frac{\omega R^2 C}{1+(\omega RC)^2} \quad (2.18)$$

From the above equations, by proper substitutions and eliminations of j by taking the complex conjugate, an equation of the following can be derived.

$$(Z' - R/2)^2 + (Z'' - 0)^2 = (R/2)^2 \quad (2.19)$$

The Eqn. 2.19 represents the equation of a circle with radius R/2 and origin (R/2, 0).

Thus, each semicircle in Fig. 2.12.b represents the impedance spectrum due to an RC parallel combination which corresponds to grain interior, grain boundary or electrode-electrolyte interface. The RC has a unit of time (s) and it represents the relaxation time or time domain of the particular process. The frequency corresponding to the crest of each semicircles gives the relaxation frequency of the concerned process and is represented by,

$$\omega_{\max} = (RC)^{-1} \quad (2.20)$$

The relative values of R and C for each component (grain interior or grain boundary or electrode) determine the frequency range of the semicircle. For widely studied ceramic oxides specimens, the low frequency semicircle is due to electrode dispersion, the intermediate semicircle due to the grain boundaries and the high frequency due to the grain interior. The individual resistances can also be found out for each component which was shown in Fig. 2.12.b. Thus, it is possible to separate the grain interior and grain boundary resistances by impedance spectroscopy.

2.8.3 Frequency response analyser

Most of the presently available instruments have a sufficiently wide frequency range of around 10^{-4} - 10^7 Hz. The impedance measurement carried out by using the Frequency response analyser (AUTOLAB instrument) having frequency 1 MHz – 1Hz. The schematic diagram of an impedance spectrometer has shown in Fig. 2.13 [23]. The sample was kept in a controlled temperature cell assembly, also shown in Fig. 2.14, which is connected to a Frequency response analyser (FRA) via a high impedance adaptor. All the three instruments are interfaced to a computer which controls the measurements and plot the results in real time. The FRA generates and transmits a sinusoidal voltage of specified frequency and amplitude to test the sample, and measured the in phase and 90^0 out of phase components of

the voltage applied to the two inputs designated as X and Y. The results are expressed as two complex voltages $V_x = V_x' + j V_x''$ and $V_y = V_y' + j V_y''$, which are communicated to the computer along with the measurement frequency f . If, R_s is a standard resistor (impedance Z_s) in the circuit, then the unknown impedance can be expressed by, $Z_u = V_y Z_s / (V_y - V_x)$.

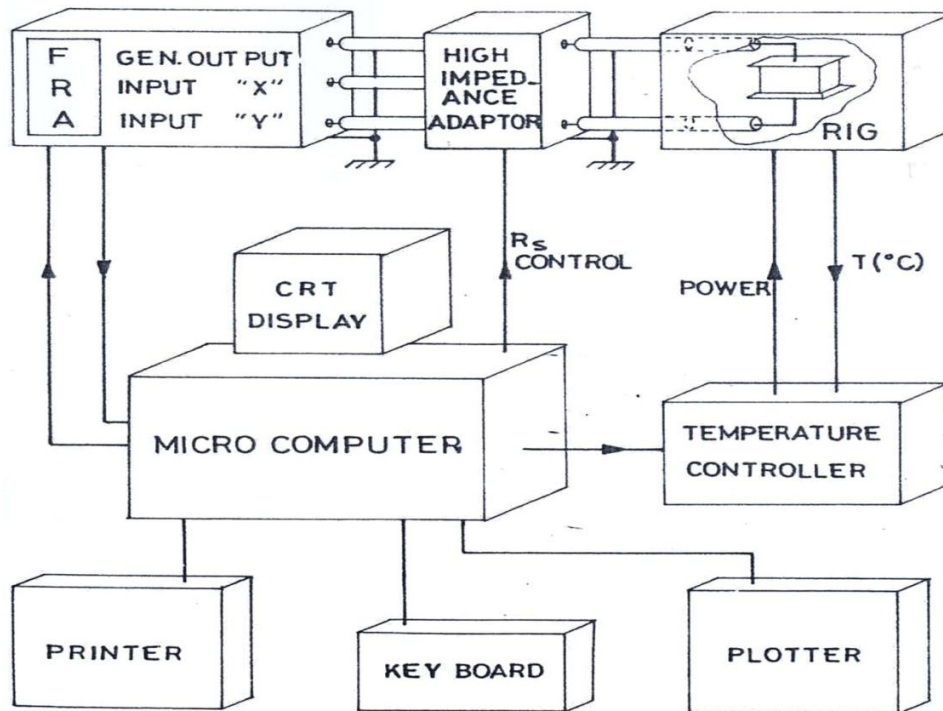


Fig. 2.13: Schematic of impedance measurement

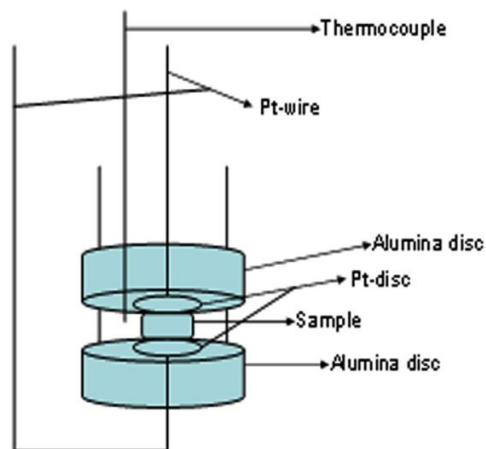


Fig. 2.14: Schematic of cell assembly for the electrical conductivity measurement

2.8.4 Applications of impedance measurements

The wide frequency range of a FRA instruments ($10^{-4} - 10^7$) enables the measurement of impedances in the range of $10^1 - 10^7 \Omega$. This means that the technique can be used for the measurement of electrical conductivity even for low conducting materials like ceramics, semiconducting solids or organic coatings for the corrosion of protection of metals other than solid electrolytes [23].

A combination of impedance spectroscopy and electron microscopy can bring out the microstructural information that is not accessible to electron microscopy alone. The microstructural features that can be investigated include the grains, grain boundary of differing compositions, segregation of one phase on another and porosity. Microstructural features will be reflected in the impedance spectrum in the form of large or small grain boundary arcs, or in the partial / total absence of one of them depending on which impedance predominates.

Solid electrolyte chemical sensors, secondary rechargeable batteries, photoelectrochemical devices and semiconductor-insulator-electrolyte sensors can also be characterized by impedance spectroscopy. The advantage here is the possibility to determine the entire time constant associated with a given interface in one experiment i.e. it is possible to determine the diffusive, electrochemical and chemical rate constants from a single impedance measurement. Further, a DC bias voltage can be superimposed on the AC signal so that the impedance and kinetic information can be collected under various conditions. By measuring the impedance in such systems as a function of the applied DC bias voltage, it is possible to ascertain the importance of the electrochemical reaction step to the overall rate of

reaction, because the applied DC potential influences the rate of electron transfer at the interface.

Electrical conductivity at high temperature is used for this type of composites to determine the diffusion coefficient of ion mostly in glass phase of the composites. Glass transition temperature, T_g measured by this method was compared with T_g obtained in DSC and dilatometry measurements.

References

1. B. D. Cullity, Elements of X-ray Diffraction, 2nd Ed., Addison-Wesley, 1978.
2. A. R. West, Solid State Chemistry and its Applications, Wiley India publications, 1985.
3. E. W. Nuffield, X-ray Diffraction Methods, John Willey & Sons, Chichester, 1996.
4. E. F. Kaelbe, Handbook on X-rays, Ed, McGraw-Hill, 1967.
5. S. Rajagopalan, K. V. G. kuty, H. K. Jajoo, S. K. Ananthakrishnan, R. Asuvathraman, Thermal expansion and phase transformation studies on some materials by high temperature x-ray powder diffractometry, IGCAR, Kalpakkam, India, IGC report no. 96, 1988, pp. 27.
6. D. D. L. Chung, P. W. DeHaven, H. Arnold, D. Ghosh, X-ray diffraction at elevated temperatures, VCH Publishers, New York, 1992.
7. D. A. Skoog, F. J. Holler, T. A. Nieman, Principles of Instrumental Analysis, 5th Edition, Saunders College Publishing, Philadelphia, 1998.
8. J. W. Dodd, K. H. Tonge, Thermal methods, John Wiley & Sons, Chichester, 1987.
9. J. L. McNaughton, C. T. Mortimer, Differential scanning calorimetry, In International Reviews in Science: Phys. Chem. Series 2, H. A. Skinner (Edi.), Butterworth's, London, 1975, pp.1-14.

10. P. Von Macromolekülen, Differential scanning calorimetry investigation of polymers, Advanced Lab. Institute Für Physic, Berlin, Germany, 1984, pp. 7.
11. L. Fröberg, Thermal analysis, Process Chemistry Centre, ÅBO Academy University, 1982.
12. M. E. Brown, Introduction of thermal analysis, Chapman and Hall, London, 1988.
13. J. M. Juoi, M. I. Ojovan, Characterization and durability of glass composite waste from immobilising spent clinoptilolite, WM'07 conference, Tucson, AZ, 2007.
14. N. V. Ojovan, I. V. Startceva, A. S. Barinov, M. I. Ojovan, D. H. Bacon, B. P. McGrail, J. D. Vienna, Product consistency test of fully radioactive high-sodium content borosilicate glass K-26, Sym. Proc. Mat. Res. Soc. Vol. 824, 2004.
15. K. V. G. Kutty, R. Asuvathraman, M. V. Krishnaiah, V. Ganesan, R. Parthasarathy, D. S. Subalakshmi, B. Suhasini, K. C. Srinivas, K. A. Gopal, P. V. Kumar, Design, fabrication and commissioning of a push rod dilatometer for thermal expansion studies on solids, IGC Report No. 283, 2006, pp. 23.
16. H. Jena, R. Asuvathraman, K. V. G. Kutty, P. R. V. Rao, Comparison of Electrical Conductivity and Thermal Properties of Borosilicate Glass with and without Simulated Radioactive Waste, J. Therm. Anal. Calorim. 115 (2014) 367-374.
17. E. F. Kaelble, MgO thermal expansion, In: E. F. Kaelble, editor, Handbook of X-rays, Chapter 13, Mc-Graw Hill, New York, 1967, pp. 15.
18. J. Belle, R. M. Berman, Thorium dioxide: properties and nuclear applications, thermal expansion chapter. DOE/NE-0060, US Department of Energy, In: J. Belle, R. M. Berman (editors), Washington DC: Govt. Printing Office, 1984, pp. 169.

19. G. Grimvall, Thermophysical properties of materials, Revised Edition, North-Holland, B. V. Elsevier Science, 1999.
20. M. V. Krishnaiah, Study of the thermophysical properties of some materials of interest in nuclear technology, PhD Thesis, University of Madras, 2000, pp. 96–104.
21. M. V. Krishnaiah, R. Asuvathraman, K. Joseph, B. Suhasini, K. V. G. Kutty, Drop Calorimeter for the measurement of enthalpy increment of solids: Design, Fabrication and Commissioning, IGC report no.-319, 2013.
22. J. A. Kilner, B. C. H. Steele, In “Non-stoichiometric oxides”, O. T. Sorensen (Ed.), Academic press, New York, 1981.
23. J. R. Macdonald (ed.), Impedance spectroscopy, John Wiley & Sons, New York, 1987.
24. J. E. Bauerle, Study of Solid Electrolyte Polarization by a complex admittance method, J. Phys. Chem. solids, 30 [12] (1969) 2657-2670.

Synthesis, characterization and thermophysical property measurement on strontium chloroapatite and its borosilicate glass-bonded composites with simulated pyrochemical chloride waste

3.1 Introduction

The metal fuelled fast reactors envisage closed fuel cycle in which pyrochemical reprocessing is the most important step to re-process the spent fuel. Molten salt electrorefining is used to separate U and Pu from the spent fuel by electro-deposition in molten salt medium [1]. In the molten salt electrorefining process; the electrolyte (45 wt. % LiCl + 55 wt. % KCl eutectic composition) needs to be periodically treated for recycling or reducing the loading of several fission products which would affect the electrolyte salt composition. Further, the radioactive waste elements added upto the electrolyte salt and are in the chloride form. The solubility of chlorides in the borosilicate glass is very small and would lead to corrosion of the matrix container. Therefore, various matrices are being tried worldwide for the fixation of chloride waste. Currently, glass-bonded sodalites are being studied for the immobilization of pyrochemical waste [2-4]. Apart from zeolites, apatites were also explored for immobilizing radwaste [5-14]. Apatites are naturally occurring minerals with a general formula of $M_{10}(PO_4)_6X_2$, where (M = Ca, Sr, Ba *etc.*; X = OH, Cl, F *etc.*); depending on the M and X-constituents, the apatite is named as hydroxy, chloro, fluoro apatite [5, 6]. In these materials, halides are part of the crystal structure. Apatites can also incorporate alkaline earth and various other aliovalent cations into its crystal structure. Apatites crystallize in hexagonal crystal system (SG = $P6_3/m$) [15, 16] and can accommodate cation and anion vacancies in its structure. Apatites are also known to have high resistance to leaching of the constituent elements under geological conditions [17]. It may not be possible to immobilize the whole

spectrum of the pyrochemical waste in a single phase Sr-chloroapatite. Therefore, attempts were made to explore the optimum waste loading into a composite matrix comprised of Sr-chloroapatite (crystalline phase) and a borosilicate glass phase. The glass encapsulated SrApCl can immobilize most of the radwaste elements in the composite matrix, thus utilizing the immobilization efficiency of both the ceramic and BSG phase [12, 18]. In this chapter, preparation of various composites were carried out in which the amount of BSG was kept constant (20 wt. %) and % waste loading was varied from 10 to 16 wt. %. The nuclear waste contains many radio nuclides (*i.e.* ^{90}Sr , ^{137}Cs *etc.*) that produce heat because of radioactive decay process. The radioactive decay heat is deposited to the host matrix consequently increasing the temperature of the matrix up to ~ 700 K. The thermophysical data such as thermal expansion, heat-capacity and glass transition temperature *etc.* of these matrices are not available in the literature. These data are very important to decide the optimum waste loading and their thermal stability for the long term storage and disposal. Therefore it is essential to evaluate the thermal expansion of the waste loaded matrices up to temperatures higher than 700 K. Thermal expansion measurements were carried out to measure % thermal expansion of the composite matrices by dilatometry. Thermo-mechanical Analysis (TMA) or dilatometry is used to determine the glass transition (T_g) temperature of the glassy phase. Therefore, dilatometric measurements were carried out at temperatures higher than the glass transition temperature of these composite matrices. Thermal expansion of the composites was also measured by high temperature XRD (HTXRD). The results obtained from two different techniques were compared. T_g of the composites were determined from dilatometry data as well as by DSC (Differential Scanning Calorimetry). The data on thermal expansion and T_g of these composites are reported for the first time. The HTXRD of the glass bonded

composites also gives an insight into the detection of in situ reactions (if any) during the heat treatment of the composite phases. The enthalpy increment values of these glass-bonded composites were also measured by home built Drop Calorimeter from which the heat capacity values of these composites were computed. The results of the experimental findings are discussed in this chapter.

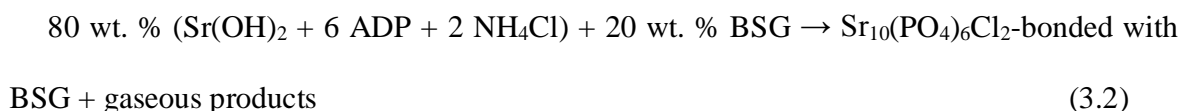
3.2 Experimental

3.2.1 Synthesis of the Sr-chloroapatite ceramic and glass-bonded simulated waste loaded Sr-chloroapatite composites

(i) Sr-Chloroapatite ($\text{Sr}_{10}(\text{PO}_4)_6\text{Cl}_2$ abbreviated as SrApCl) was synthesized using solid state reaction route by mixing stoichiometric concentrations of $\text{Sr}(\text{OH})_2$, $\text{NH}_4\text{H}_2\text{PO}_4$ (ADP) and NH_4Cl ; reactants were ground thoroughly and calcined at 773 K / 5 h then heated at 1023 K for 5 h in air in platinum boat/crucible. The chemical reaction is shown in Eq. 3.1



(ii) Similarly, 20 wt. % BSG bonded Sr-chloroapatite (abbreviated as SrApCl-20BSG) was prepared by mixing apatite forming reagents and borosilicate glass forming reagents (57 wt. % SiO_2 , 25 wt. % B_2O_3 and 18 wt. % Na_2O) [12] and calcined at 773 K / 5 h then heated at 1023 K for 5 h in platinum boat/crucible in air ambience. The chemical reaction is shown in Eq. 3.2



(iii) Waste loaded Sr-chloroapatite (abbreviated as SrApCl-10w) was prepared by weighing out required amounts of apatite forming reagents and a simulated chloride waste composition (2.63 wt. % CeCl_3 + 12.08 wt.% NdCl_3 + 1.38 wt. % BaCl_2 + 1.74 wt. % CsCl +

11.23 wt. % NaCl + 70.91 wt% LiCl-KCl eutectic) derived from the salt composition resulting in processing of EBR-II driver fuel [2], in appropriate ratios (Tables 3.1 and 3.2), mixed, ground thoroughly and heated at 773 - 1023 K for 5 h in air ambience in platinum boat/crucible. The chemical reaction is shown in Eq. 3.3

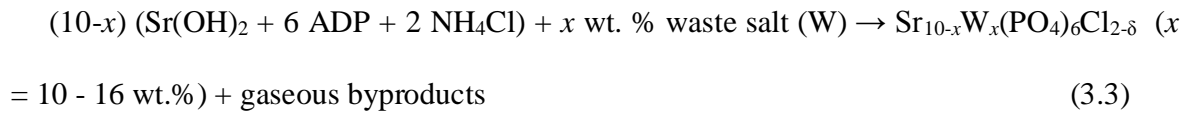


Table 3.1: compositions of simulated glass waste

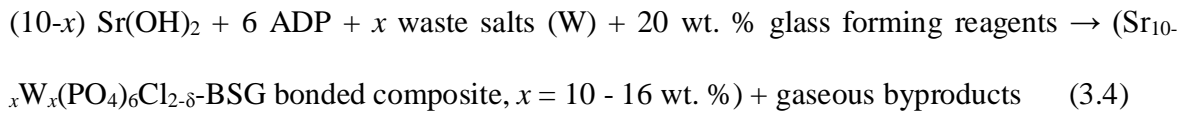
Name of compound	LiCl	KCl	NaCl	CsCl	BaCl ₂	CeCl ₃	NdCl ₃
Mass %	31.92	39.01	11.23	1.74	1.38	2.63	12.08
Mol %	48.67	33.90	12.49	0.67	0.43	0.70	3.14

Table 3.2: Composition of Sr-chloroapatite glass composite with simulated waste shown in mass and mol % for a 10 g target matrix (with 10 wt. % waste + 20 wt. % BSG + 70 wt. % SrApCl composite)

Name of compound	LiCl	KCl	NaCl	CsCl	BaCl ₂	CeCl ₃	NdCl ₃	SiO ₂	B ₂ O ₃	Na ₂ O	SrApCl	Total
Mass %	3.19	3.90	1.12	0.17	0.14	0.26	1.21	11.40	5.00	3.60	70.00	100
Total mass%	10 wt. % simulated waste salt							20 wt. % glass			70wt. %	
Mol %	14.46	10.05	3.69	0.20	0.13	0.21	0.93	36.49	13.81	11.17	8.87	100
Total mol%	29.67							61.47			8.87	
Cations	Li ⁺	K ⁺	Na ⁺	Cs ⁺	Ba ²⁺	Ce ³⁺	Nd ³⁺				Sr ²⁺	
Mol % in cation sub-lattice in Sr _{10-x} W _x (PO ₄) ₆ Cl _{2-δ}	12.21	8.49	3.12	0.17	0.11	0.17	0.78	Glass is not considered for lattice substitution, because it is second phase			74.95 mol % Sr ²⁺	100 mol % cations only

(iv) Lastly, Waste loaded BSG bonded apatite compositions (abbreviated as SrApCl-10w20BSG, SrApCl-13w20BSG and SrApCl-16w20BSG) were prepared by weighing out

required amounts of apatite forming reagents, glass forming reagents [12] and a simulated chloride waste composition [2] in appropriate ratios, mixed, ground thoroughly and heated at 773 - 1023 K for 5 h in air ambience in platinum boat/crucible. The chemical reaction is shown in Eq. 3.4



The prepared Sr-chloroapatite and its glass-bonded composites were shown in the following Table 3.3.

Table 3.3: synthesized Sr-chloroapatite and its glass-bonded composites

Glass-bonded compositions	Strontium chloroapatite (SrApCl, wt. %)	Simulated chloride waste (W, wt. %)	Borosilicate glass (BSG, wt. %)
SrApCl	100	-	-
SrApCl-20BSG	80	-	20
SrApCl-10w	90	10	-
SrApCl-10w20BSG	70	10	20
SrApCl-13w20BSG	67	13	20
SrApCl-16w20BSG	64	16	20

The nominal waste loadings were in the range 10 - 16 wt. %. The products were characterized by X-ray diffraction (XRD), Thermogravimetry Analysis (TGA) / Differential Thermal Analysis (DTA), Scanning Electron Microscopy-Energy Dispersive X-ray Analysis (SEM-EDAX).

3.2.2 Fabrication of pellets of Sr-chloroapatite with varying amounts of chloride waste and BSG

The powder samples of Sr-chloroapatite (SrApCl), 20 wt. % BSG encapsulated Sr-chloroapatite (SrApCl-20BSG), Sr-chloroapatite with 10 wt. % simulated (SrApCl-10w) and Sr-chloroapatites + x wt. % chloride waste + 20 wt. % BSG (SrApCl- x w20BSG, $x = 0 - 16$) were fabricated into cylindrical pellets of 10 mm diameter and 10 mm height using tungsten carbide die and plunger. The powder was pressed under ~ 2 -tons of load in the die and plunger using a pellet press (Hydraulic pellet press, Ms. Kimaya Engineers, India). The pellets were heat-treated at 1123 K for 8 -15 h in air on a platinum boat/crucible to improve the density of the pellets. The following compositions were thus fabricated (a) Sr-chloroapatite (SrApCl) (b) SrApCl + zero waste + 20 wt. % BSG (SrApCl-20BSG) (iii) SrApCl + 10 wt. % waste + zero BSG (SrApCl-10w) (iv) SrApCl + 10 wt. % chloride waste + 20 wt. % BSG (SrApCl-10w20BSG) (v) SrApCl + 13 wt. % chloride waste + 20 wt. % BSG (SrApCl-13w20BSG) (vi) SrApCl + 16 wt. % chloride waste + 20 wt. % BSG (SrApCl-16w20BSG), as shown in Table 3.3. The theoretical density of the composites was calculated by using volume fraction procedure. The major phases considered for theoretical density calculation of the composites are borosilicate glass and apatite phase. $V_{BSG} = M_{BSG} / \rho_{BSG}$; where, V_{BSG} = Volume of BSG, M_{BSG} = mass of BSG = Weight of BSG taken for the experiment, ρ_{BSG} = theoretical density of BSG (from literature for the specified composition used in this study). Similarly, $V_{SrApCl} = M_{SrApCl} / \rho_{SrApCl}$, Volume fraction of BSG = $V_{f-BSG} = V_{BSG} / (V_{BSG} + V_{SrApCl})$ and Volume fraction of SrApCl = $V_{f-SrApCl} = V_{SrApCl} / (V_{BSG} + V_{SrApCl})$. $V_{f-BSG} + V_{f-SrApCl} = 1$ for a composite with two components. Therefore, $\rho_{composite} =$

$(V_{f\text{-BSG}} \times \rho_{\text{BSG}}) + (V_{f\text{-SrApCl}} \times \rho_{\text{SrApCl}})$. The measured density of the pellets was nearly 82 - 85 % of the theoretical density. These glass bonded composites can achieve maximum 85 % of theoretical density under the preparation conditions followed in this work. This may be attributed to the inherent porous nature of the material.

3.2.3 Leaching studies on the simulated waste loaded samples by hydrothermal condition (Autoclave) and Soxhlet method

1 gm of each powder sample were taken in teflon cell / bowl, added 10 ml of deionized water. The cell was then closed by using the teflon lid. Then the teflon cell was put into an autoclave. The autoclave was heated to 423 K for 1 day in a PID controlled furnace at air ambience. The details of this method were described in chapter-2. Comprehensive leaching studies were done on the composites under soxhlet condition at 363 K (or 90°C) for 28 days. The details of this method were also described in chapter-2. In both of these methods, the analysis of the leachate solutions were done by AAS for alkali and alkaline earth elements; ICP-OES for rare earth elements and Ion Selective Electrode for Cl. From the leachate solution, concentration of Cl, Li, Na, K, Cs, Sr, Ba, Nd, Ce *etc.* were determined. Then the normalised leach rate (NLR, $\text{g cm}^{-2} \text{d}^{-1}$) was calculated for each element mentioned above by using the following equation [19, 20].

$$\text{NLR} = \frac{A_i \times V}{f_i \times S \times t} \quad (3.5)$$

Where, A_i = concentration of the i^{th} species in the leachate solution ($\mu\text{g/ml}$), V = volume of distilled water taken for analysis (ml), f_i = mol fraction of i^{th} element / species, S = surface area (cm^2) and t = time (d). The normalised leach rate obtained in this study was found to be in the order of $10^{-6} \text{g cm}^{-2} \text{d}^{-1}$ which is close to the literature data [18, 21].

3.2.4 Thermal expansion measurements on the glass bonded composites by high temperature X-ray diffraction (HTXRD)

The % linear axial expansion of the powders was measured by using Philips X'pert-Pro MPD model XRD machine with high temperature attachment. The powder samples were loaded onto a tantalum / platinum strip sample holder. The strip also acted as heater to heat the sample to various pre-set temperatures. The temperature of the sample was controlled by an Eurotherm temperature controller (900 EPC model) with an accuracy of ± 1 K. The sample was heated on the Ta-strip and the temperature of the sample was measured by K-type thermocouple attached/spot welded to the bottom of the Ta-strip heater. The Ta-strip was attached to the electrodes and the strip with powder sample was heated in a vacuum of 10^{-5} torr. The XRD patterns of the samples were recorded at room temperature (RT) then the temperature of the sample was increased to 373 K, 473 K, 573 K and 673 K by programmed heating and cooling with a heating / cooling rate of 5 K min^{-1} . XRD pattern of the sample was recorded at preset temperatures. The lattice constants of the samples were calculated from the XRD pattern recorded at various temperatures by using X'pert Plus software package supplied by Philips. The % linear expansion along a -axis and c -axis was measured by using the following formula [22, 23].

$$\% \text{ expansion along } a - \text{axis} = \frac{a_{673} - a_{RT}}{a_{RT}} \times 100 \quad (3.6)$$

$$\text{Similarly, \% expansion along } c - \text{axis} = \frac{c_{673} - c_{RT}}{c_{RT}} \times 100 \quad (3.7)$$

The mean or average coefficient of thermal expansion ($\text{CTE} = \alpha_m$) was calculated by using the following formula

$$\text{Along } a - \text{axis; CTE} = \frac{a_{673} - a_{RT}}{a_{RT}} \times \frac{1}{\Delta T} \quad (3.8)$$

$$\text{along } c - \text{axis; CTE} = \frac{c_{673} - c_{RT}}{c_{RT}} \times \frac{1}{\Delta T} \quad (3.9)$$

3.2.5 Thermal expansion and glass transition temperature (T_g) measurements by dilatometry

Thermal expansion and glass transition temperature measurements on pellets of 10 mm diameter and 10 mm height were carried out by dilatometry in the temperature range 323 - 800 K in air, by using a home-built apparatus [24]. A Linear Variable Differential Transformer (LVDT) was used as the displacement sensor (M/s. Syscon Pvt. Ltd., Bangalore). The accuracy of displacement measurement by LVDT was $\pm 1 \mu\text{m}$. A chromel-alumel (type-K) thermocouple was used to measure the temperature of the sample and was placed very close to the sample. Programmed heating, cooling and data acquisition of the sample was done through a computer programme and necessary electronics required for data processing and control. The heating and cooling rates used for these measurements were 2 K min^{-1} and 5 K min^{-1} respectively. The instrument was calibrated by measuring percentage thermal expansion of standard MgO single crystal and ThO₂ pellet. The % linear expansion of MgO pellet was measured and compared with the values reported in the literature [25]. Similarly, the percentage thermal expansion of the ThO₂ pellet was measured and compared with the values reported by Belle and Berman [26]. The difference in fitted value and experimentally measured value of standard MgO single crystal is taken as the correction factor for the samples studied. The density and dimension of the pellets were once again measured after the thermal expansion measurements were complete and were found to remain unchanged. The % linear expansion for each composition was measured in the

temperature range below the glass transition temperature of the encapsulated glass phase.

The % linear expansion was calculated by using the following formula [22, 23].

$$\text{Percentage linear expansion} = \frac{\Delta L}{L_0} \times 100 \quad (3.10)$$

Where, ΔL = change in length = $L_{i+1} - L_1$, for $i = 0, 1, 2 \text{ etc.}$; L_1 = initial length (where $i = 0$) recorded on the displacement sensor of the dilatometer at nearly room temperature. On raising the temperature of the pellet to higher values the pellet expands and length is expressed as L_{i+1} . Therefore, the change in length is measured by subtracting L_1 from L_{i+1} . However, L_0 is different from L_1 . L_0 is the original length of the pellet at room temperature.

The average or mean coefficient of linear thermal expansion (CTE) of the matrices was measured below the glass transition temperature of the glass phase. The coefficient of thermal expansion was calculated by using the formula

$$\text{CTE} = \alpha_m = \frac{\Delta L}{L_0} \times \frac{1}{\Delta T} \quad (3.11)$$

Where, ΔL = change in length = $L_{i+1} - L_1$, L_0 = length of the pellet at room temperature, $\Delta T = T - T_i$ = change in temperature in K, where T = highest temperature of each measurement.

The instantaneous coefficient of thermal expansion (α_i) was determined by using the following formula [22, 23].

$$\alpha_i = \frac{1}{L_0} \times \frac{dL}{dT} = \frac{1}{L_0} \times \frac{L_{i+1} - L_1}{T_{i+1} - T_1} \quad (3.12)$$

Where, L_0 = length of the sample at room temperature, L_{i+1} = length of the pellet when temperature of the sample is T_{i+1} , L_1 = length of the sample at temperature (T_1) when heating is started at the beginning of heating cycle of the experiment. The onset of the

instantaneous CTE *vs.* T (K) will give the glass transition temperatures of the corresponding glass-bonded Sr-chloroapatites composites. The T_g values obtained from the dilatometry measurement were compared with that the value obtained from Differential Scanning Calorimetry (DSC).

3.2.6 Glass transition temperature (T_g) and heat capacity (C_p) measurements by DSC

The measurements on heat capacity and glass transition temperatures were carried out using differential scanning calorimeter (DSC) (Model No.: DSC821e/700 of M/s. Mettler Toledo GmbH, Switzerland). Temperature calibration was carried out by determining the melting temperatures of indium, tin, lead and zinc, supplied by National Institute of Standards and Technology, USA (NIST), at heating rates of 2, 5, 10 and 20 K min⁻¹. The onset temperature of melting at different heating rates was plotted against the heating rate and extrapolated to zero heating rates. The extrapolated onset temperature at zero heating rates was used for temperature calibration. The calibration curve was obtained by fitting the difference between the known melting point of the calibration substances and the extrapolated onset temperatures to a second-order polynomial. This provides instrument calibration under steady-state condition. The slope of melting point against heating rate curve gives the τ -lag, the difference between the time for the temperature sensor and sample to attain a given temperature under dynamic conditions. The calibration curve for the τ -lag was also obtained by fitting τ -lag at different temperatures to a second-order polynomial. The typical value of τ -lag is 1–3 s. Heat calibration was carried out by measuring the enthalpy of melting of indium, tin, lead and zinc at 10 K min⁻¹. Heat rate calibration was performed prior to each

heat capacity measurement with a disc of sapphire supplied by M/s. Mettler Toledo GmbH, Switzerland using the heat capacity data of sapphire from NIST, USA.

60 mg samples in the form of pellets were weighed accurately and hermetically sealed in 40-L aluminium pans. The flow rate of the purge gas (ultra high pure argon) was 50 mL min⁻¹. A three-segment temperature programme was used. The first segment was isothermal lasting for five minutes at the initial temperature; the second segment was from the initial temperature to the final temperature at a heating rate of 10 K min⁻¹ and the final segment lasting for 5 min was again an isothermal one at the final temperature. Each heat capacity measurement consisted of a set of three runs, namely: a blank run with empty pans on both sample and reference sides, a sapphire run with empty pan on the reference side and the pan with disc of sapphire on the sample side and finally the sample run with empty pan on the reference side and the sample in the form of pellet on the sample side.

3.2.7 Enthalpy increment and C_p measurement by Drop Calorimetry

Enthalpy increments of these glass-bonded ceramic composites were measured by using a home built drop calorimeter [27, 28] at the temperature range of 373 – 773 K with a step size of 50 K. Synthetic sapphire (SRM-720, α -Al₂O₃), obtained from NIST, USA was used as the standard reference material. In a typical measurement, the sample or the reference is placed in a furnace and equilibrated at the desired temperature and then dropped into the calorimeter vessel maintained at 298 K. The furnace temperature was controlled using a temperature controller within ± 1 K. The change in temperature of the calorimetric vessel as a function of time was continuously monitored by a thermopile detector and the signal logged to the computer. The signal increases sharply when the sample is dropped into the calorimeter vessel and decreases steadily to the initial background value. A typical screen

shot of the drop calorimeter's data acquisition system for the measurement of peak area as shown in Fig. 2.11 (chapter-2). The enthalpy increment ($H_T^0 - H_{298K}^0$) of the sample was derived by using Eqn. 3.13.

$$\frac{\text{Enthalpy increment of sample}}{\text{Enthalpy increment of standard}} = \frac{\text{Area under the curve per gm of sample}}{\text{Area under the curve per gm of standard}} \quad (3.13)$$

At each temperature, the standard and sample were dropped alternatively for 4-6 times, and the average value was taken. Details on the calorimeter system and the measurements are given elsewhere [27, 28].

The enthalpy increment data were fitted to an equation (Eqn. 3.14) of the form

$$H_T^0 - H_{298K}^0 = a + bT + cT^2 + d/T \quad (3.14)$$

, using the non-linear least square fitting program written in Matlab software. Two linear constraints were imposed on the coefficients to get a meaningful fitting as shown in Eqn. 3.15 and 3.16.

$$(i) \quad (H_T^0 - H_{298K}^0)_{298} = 0 \quad (3.15)$$

$$(ii) \quad \left(\frac{d}{dT} (H_T^0 - H_{298K}^0)_{298} \right) = (C_p)_{298} \quad (3.16)$$

The heat capacity, C_p was derived from the enthalpy increment data by differentiating the fitted equation (eqn. 3.14) as given in Eqn. 3.17.

$$C_p = b + 2cT - d/T^2 \quad (3.17)$$

The validation of the home-built drop calorimeter was done by measuring the enthalpy increments of standard MgO single crystal procured from Crystec, USA. A set of six experiments were carried out involving sequential drop of alumina and MgO alternatively at each temperature starting from 323 to 1023 K. The results were plotted in Fig. 3.1. The measured enthalpy increment data obtained by using the home built dilatometer and the

derived molar heat capacity data of MgO available in the literature [29] are in good agreement. The standard error between the measured values and fit values for standard MgO was found to be 0.3%.

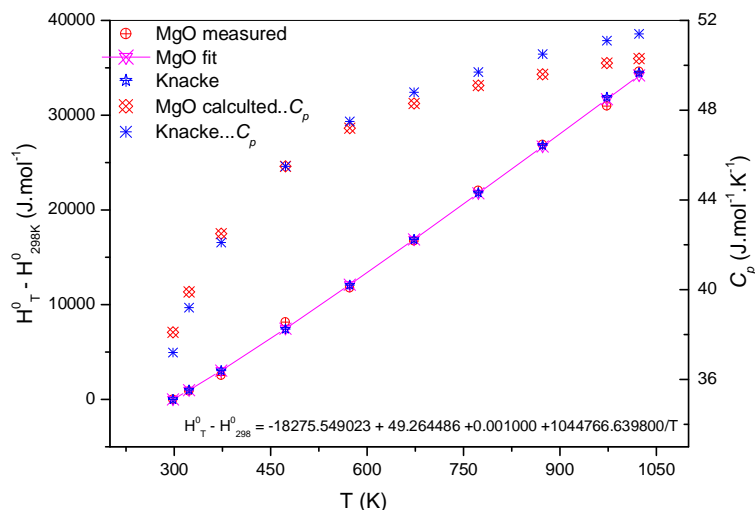


Fig. 3.1: Measured and fit enthalpy increments values and heat capacity of standard MgO compared with the Knacke *et. al.*

3.2.8 Electrical conductivity measurement by AC and DC technique

The electrical conductivity of SrApCl, SrApCl-10w, glass (BSG) and their glass-bonded composite (SrApCl-20BSG, SrApCl-10w20BSG, SrApCl-13w20BSG and SrApCl-10w16BSG) were carried out by AC impedance techniques. For the electrical conductivity measurements, the cylindrical pellets of pristine glass was prepared by melting of the synthesized glasses at 1273 K and then the melt was transferred or poured into a graphite crucible (12 mm dia and 15 mm length) to fabricate pellets of required dimension. The graphite crucible was cut to open and remove the glass pellets. These pellets (10 mm dia and 6 mm length) were annealed at 800 K in a platinum crucible for 15 h in air. The pellets were

characterized by powder-XRD once again to confirm amorphous character and subsequently used for electrical resistivity measurements. Whereas, in case of measurements of electrical conductivity of glass-bonded glass ceramic composites, the pellets (10 mm dia and 2 mm length) were fabricated and subsequently heated to 1073 K for 10 h in air ambience. The pellets were characterized by powder-XRD once again to confirm the presence of crystalline Sr-chloroapatite phase in the composite matrix and used for electrical resistivity measurements. The top and bottom flat surfaces of pellets were metalized using Ag-paste. The metalized pellets were loaded in the high temperature conductivity cell and the cell was put inside the furnace well. The details of the high temperature electrical conductivity cell are reported elsewhere in those of the earlier studies [30]. The temperature of the furnace was controlled by a programmable PID temperature controller with ± 1 K accuracy. The sample temperature was measured with a K-type (chromel–alumel) thermocouple placed at about 2 mm from the sample in the conductivity measurement cell. Resistances of the sample were measured at each 25 K interval. The impedance (Z) measurements were carried out using an Autolab frequency response analyser (FRA) (AUTOLAB, ECO CHEMIE BV, Serial no.: AUT83524) in the frequency range of 100 Hz –1 MHz. The impedance / resistance of the samples at various temperatures was determined by fitting the data of $-Z''$ (ohm.cm) versus Z' (ohm.cm) Nyquist plot using fit and simulates functions available in the Autolab FRA system. The real part of the semicircle ($-Z''$ vs. Z') is taken as the resistance of the sample at a particular temperature. The fitting of the semicircle was performed by trial and error method on assigning various equivalent circuit models available with the software provided by Autolab. The equivalent circuit that fits all the points on the semicircle with minimum error is taken as the accepted model and the values of R and C calculated by the model for a

particular temperature were taken as the accepted value. The DC resistance measurements were performed by Agilent 34401A model. The conductivity of samples was calculated using the formula as given in Eq. 3.18.

$$\sigma = \frac{L}{A} \times \frac{1}{R} \quad (3.18)$$

Where, σ is the conductivity in $S\ cm^{-1}$, R is the resistance in ohms, L is the length or thickness of the pellet (cm) and A is the cross sectional area of the pellet (cm^2).

3.3 Results and discussions

3.3.1 Characterization by powder-XRD and SEM-EDAX studies

Fig. 3.2 shows the formation of crystalline phases of $Sr_{10}(PO_4)_6Cl_2$ in all cases including substitution of simulated fission products and borosilicate glass-bonded composites. The XRD patterns in Fig. 3.2 show the presence of SrApCl as the crystalline phase, the XRD pattern was matching with the pattern reported in the literature [14-15, 31]. No crystalline (impurity) phases other than SrApCl were observed in the XRD patterns of the composites. However, XRD pattern of SrApCl-16w20BSG shows the formation of impure crystalline phases as indicated in Fig. 3.2 other than Sr-chloroapatite. A few reflections corresponding to $Sr_3(PO_4)_2$ appeared in the XRD patterns of the samples, when the powders were heat-treated above 1223 K for longer durations. However, this aspect was taken care by adding little excess of NH_4Cl to compensate the chloride loss during the preparation of the sample. However, in the waste loaded samples, chloride loss was compensated by the chloride (Cl^-) present in the waste compounds itself ($LiCl$, KCl , $NaCl$ *etc.*) and separation of $Sr_3(PO_4)_2$ phase was not observed in the XRD patterns. The XRD patterns shown in Fig. 3.2 corresponding to waste loaded and glass bonded composites match with the XRD pattern of $Sr_{10}(PO_4)_6Cl_2$ [14-15, 31]. The waste loaded compositions can be written as Sr_{10} -

$_xW_x(PO_4)_6Cl_{2-\delta}$ -BSG bonded composite. Therefore, an optimum waste loading upto 13 wt. % is possible to form single crystalline phase of strontium chloroapatite among these composites.

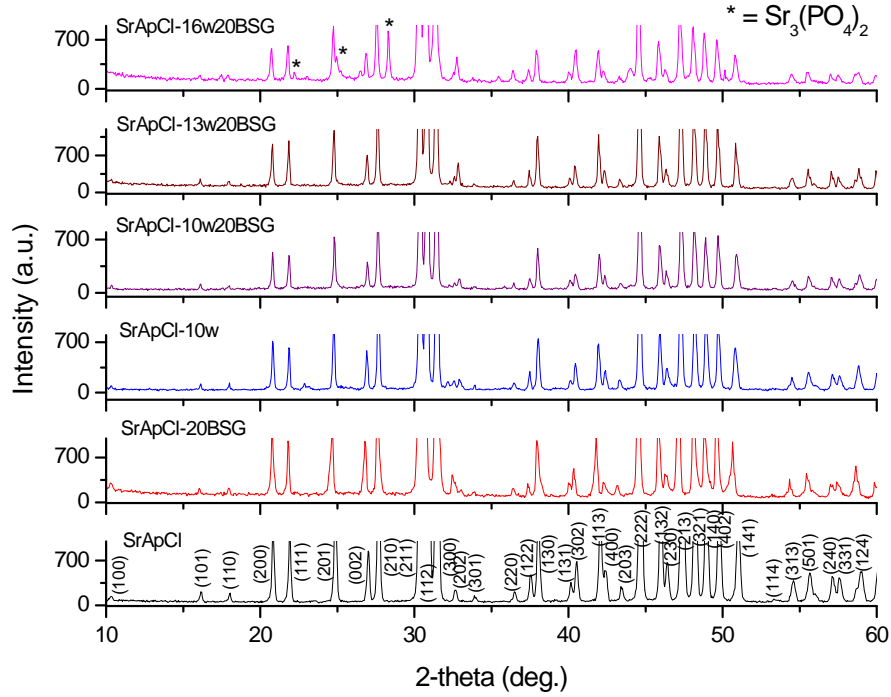


Fig. 3.2: Room temperature XRD patterns of SrApCl + x wt. % Waste + y wt. % BSG composites, (x = 0 - 16, y = 0 - 20).

Waste elements/cations (Li^+ , K^+ , Nd^{3+} , Ce^{3+} etc.) can substitute at Sr-sublattice and Cl^- at Cl-sublattice of SrApCl within the solubility limit of the material by forming dilute solid solutions. The second possibility is the distribution of waste elements among the crystalline (SrApCl) and BSG phases of the composite depending on their thermodynamic stability, ionic radii, charge etc. leads to the formation of SrApCl-glass bonded composite matrix within 16 wt. % waste loading without affecting crystal structure of Sr-chloroapatite. On converting the 10 wt. % concentration of simulated waste elements to mol % cations and

anions for SrApCl-10w20BSG composite as shown in Table 3.2, it is observed that the nominal concentration of total cations is around 25 mol% [$12.21 (\text{Li}^+) + 8.49 (\text{K}^+) + 3.12 (\text{Na}^+) + 0.17 (\text{Cs}^+) + 0.11 (\text{Ba}^{2+}) + 0.17 (\text{Ce}^{3+}) + 0.78 (\text{Nd}^{3+}) = 25 \text{ mol\%}$]. 25 mol% cation substitutions at Sr-sub-lattice in SrApCl are not feasible. Therefore, 10 mol% of cations (within solubility limit) might have been substituted to the Sr-sublattice in SrApCl crystalline phase and rest 15 mol % might have entered into the glass matrix that is in intimate contact with the crystalline phase. Similarly, in case of 13 to 16 wt. % nominal waste loading the cations might have been distributed among the crystalline and glass phases. The formation of 1 mol of $\text{Sr}_{10}(\text{PO}_4)_6\text{Cl}_2$ needs 10 mol of Sr^{2+} , 6 mol of PO_4^{3-} and 2 mol of Cl^- ions from the reactants. The amount of chloride ions furnished by the 10 wt. % waste salt for the above mentioned composite is much higher than required as per the chemical reaction shown in Eqn. 3.3. On calculating the total Cl required for the above said composition, it is observed that only ~ 28 wt fraction of Cl is retained or utilized for the formation of SrApCl. The excess Cl and salts might have escaped from the reaction medium while heat-treating the samples at 1123 K. However, the Cl released on heating above 773 K may react with the NH_3 (Eqns. (3.1) - (3.2)) leading to the formation of NH_4Cl in the reaction medium. All these byproducts decompose at the heat-treatment temperature and escape from the reaction medium. Therefore, the impurity phases are not observed in the XRD patterns. Further investigations may be required to find out the clear mechanism of these gas phase reactions. The substitution of aliovalent cations smaller or bigger in size (ionic radii) compared to Sr^{2+} into the various lattice positions may affect the intensity of reflections in the XRD pattern of the compound. However, a decrease in intensity was observed on the waste loaded samples compared to pristine SrApCl (Fig. 3.2). The decrease in intensity of certain peaks *i.e.* (200),

(111) etc. in the XRD pattern may happen if low Z elements (low atomic number elements compared to Sr) are substituted to the lattice positions corresponding to those Miller planes. However, waste loaded composites need to be examined by various other experimental techniques such as EXAFS *etc.* (Extended X-ray Absorption Fine Structure) for the comprehensive understanding of the systems.

$\text{Sr}_{10}(\text{PO}_4)_6\text{Cl}_2$ has hexagonal crystal structure (SG = $P6_3/m$) [5, 14, 15]; the crystal structure of $\text{Sr}_{10}(\text{PO}_4)_6\text{Cl}_2$ is shown in Fig. 3.3.

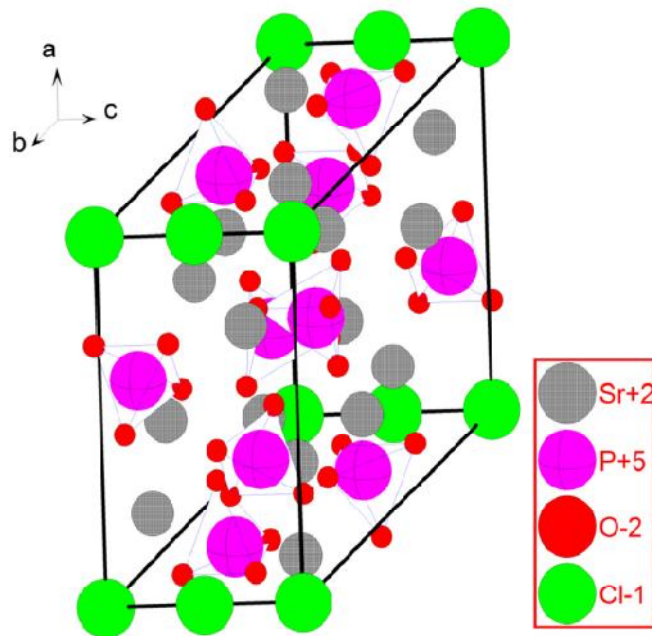


Fig. 3.3 The crystal structure of $\text{Sr}_{10}(\text{PO}_4)_6\text{Cl}_2$

The Sr-cation forms two types of Sr-O coordination in SrApCl lattice. Sr-I type coordination has 9-oxygen atoms around Sr, the second type of coordination (Sr-II) in which Sr-is bonded to 6-oxygen atoms and one Cl. The P- forms PO_4 tetrahedra as shown in Fig. 3.3. The Cl-atoms are at the edge of the unit cell.

The waste elements which form solid solutions with Sr-chloroapatite and glass matrix are given in Table 3.1. The waste elements substitute at Sr-sublattice but not into the P-site in PO_4 tetra-hedra. Therefore, it is assumed that PO_4 tetra-hedra are unaffected by waste element substitution. The incorporation or immobilization of the simulated waste elements in the composite matrix was also investigated by examining the surface of the samples by SEM-EDAX (Fig. 3.4(a, b)). In Fig. 3.4(a) the SEM image of the fractured surface of the sample pellet is shown and the corresponding EDAX is shown in Fig. 3.4(b). The SEM image shows the segregation of glassy phase at the grain boundary of SrApCl crystalline phase. The SEM-EDAX shows the incorporation of Cl in the glass bonded composite (Fig. 3.4(b)).

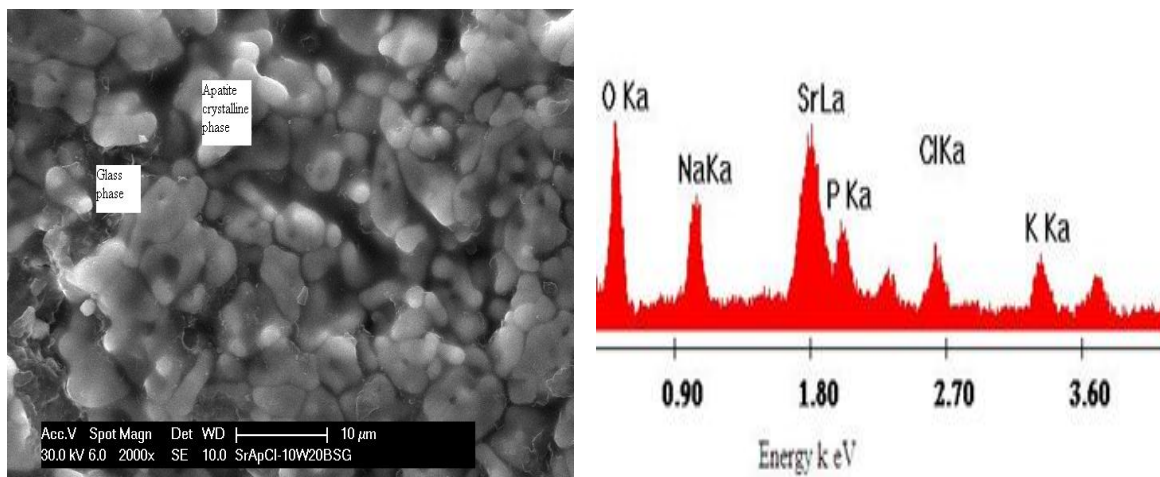


Fig. 3.4: (a) SEM image of SrApCl-10w20BSG showing the Crystalline and glass phases and (b) Corresponding EDAX of the SEM image shown in (a); showing the retention of Cl in the glass ceramic matrix along with various other constituents.

3.3.2 Leaching studies by autoclave and soxhlet method

The concentrations of leachate species by autoclave method were measured by various analytical techniques and the normalised leach rate were also calculated by using the

Eqn. 3.5 as shown in Fig. 3.5. All the concentration of the leachate species are in the range of *ppm* level. The leachate concentration of chloride in SrApCl is 20.5 ± 1.0 *ppm*. This may be attributed to the loosely bound chloride into the surface of the pure strontium chloroapatite. The concentration of chloride in SrApCl-0w20BSG (1.82 ± 0.09 *ppm*) is lower than that of pure SrApCl. This may be supposed to lower chloride content as well as an extra layer of protection by glass over the apatite. However, the chloride concentrations are found to be 2.28 ± 0.11 *ppm* for SrApCl-10w and 4.16 ± 0.21 *ppm* SrApCl-10w20BSG. The concentration of chloride increases from SrApCl-10w0BSG (4.16 ± 0.21 *ppm*) to SrApCl-13w20BSG (15.9 ± 0.80 *ppm*) to SrApCl-16w20BSG (378.0 ± 18.9 *ppm*). This is due to the increasing chloride content as we increase the waste percentage (10 wt. % to 16 wt. %) into the immobilized matrix. The normalised leach rates for the Cl in the waste loaded glass ceramic composites are in the range of 0.05×10^{-6} to 1.06×10^{-6} $\text{g cm}^{-2} \text{d}^{-1}$ which shows a very much resistance to leaching behavior from these matrices and also within the acceptable limits.

The leaching of Na is also increasing from SrApCl-10w to SrApCl-16w20BSG because of higher sodium content as we increase the waste loading. The source of sodium is from NaCl (a part of waste content) as well as from Na₂O (a modifier of glass). The normalised leach rates for Na for the matrices are in the range of 0.22×10^{-6} - 1.54×10^{-6} $\text{g cm}^{-2} \text{d}^{-1}$ which is well below the acceptable limits.

The leachate concentration of Li in SrApCl-10w0BSG (10.4 ± 0.5 *ppm*) is higher than that of SrApCl-10w20BSG (5.9 ± 0.3 *ppm*). This may be attributed to the higher Li content (source of Li as LiCl) in the SrApCl-10w than SrApCl-10w20BSG and also an extra protection layer is given by glass. After that, the leachate concentrations of Li are increasing as usual from SrApCl-10w20BSG (5.9 ± 0.3 *ppm*) to SrApCl-16w20BSG (36.0 ± 1.8 *ppm*)

because of higher Li content into the glass-bonded ceramic compositions. The normalised leach rate for the Li was found to be in the range of 0.28×10^{-6} to $1.08 \times 10^{-6} \text{ g cm}^{-2} \text{ d}^{-1}$ for these glass ceramic composites.

The leaching behavior of K and Cs are in the range of $(9.3 \pm 0.5 \text{ ppm}$ to $22.84 \pm 1.14 \text{ ppm}$), $(0.28 \pm 0.01 \text{ ppm}$ to $37.55 \pm 1.88 \text{ ppm}$) respectively and follows the same trend as that of Li in these matrices. Normalised leach rate are also very much in the acceptable range of $(0.11 \times 10^{-6}$ to $0.21 \times 10^{-6} \text{ g cm}^{-2} \text{ d}^{-1})$ and $(0.05 \times 10^{-6}$ to $4.07 \times 10^{-6} \text{ g cm}^{-2} \text{ d}^{-1})$ for K and Cs respectively.

On the other hand the concentrations of Ba, Ce and Nd in the leachate are below detection limits ($< 0.4 \text{ ppm}$) and the normalised leach rates for these ions were found to be 0.02×10^{-6} , 0.01×10^{-6} and $0.002 \times 10^{-6} \text{ g cm}^{-2} \text{ d}^{-1}$ respectively. Hence, these elements can be retained by the proposed glass-ceramic composite matrices.

The leaching behaviors of the waste loaded strontium chloroapatite and its glass bonded composites were also carried out by sohxlet methods. The results of the leachate species concentrations with time (h) were measured and the corresponding normalised leach rates were given in Fig. 3.6.

From the leachate concentrations of the species, it was found that the leachate concentration of Li, Na K, Cs, Ba and Cl are within 15 ppm and the variation of their concentration with time was negligible, whereas the concentration of Nd and Ce were found to be below detection limits (*i.e.* $< 0.4 \text{ ppm}$). The error involved in these measurements was about $\pm 5\%$ of the measured value. However, the concentration of Si was found to be slightly higher compared with that of the other elements. The normalised leach rate were also evaluated from these leachate concentrations of these elements and found to be in the range

of $6.5 \times 10^{-6} - 0.02 \times 10^{-6} \text{ g cm}^{-2} \text{ d}^{-1}$. Normalised leach rate were found to be higher at the initial days of leaching; then it decreases with time and eventually get saturated. NLR values are well within the permissible limit (the acceptable limit of NLR is around $10^{-6} \text{ g cm}^{-2} \text{ d}^{-1}$).

Here, chemical durability (leach resistance property) of SrApCl-10w20BSG sample was carried out by autoclave (static method) as well as by soxhlet measurement (dynamic method). The normalised leach rate was lower in case of autoclave measurement than that of soxhlet measurement due to the effect of common ion effect in the former case.

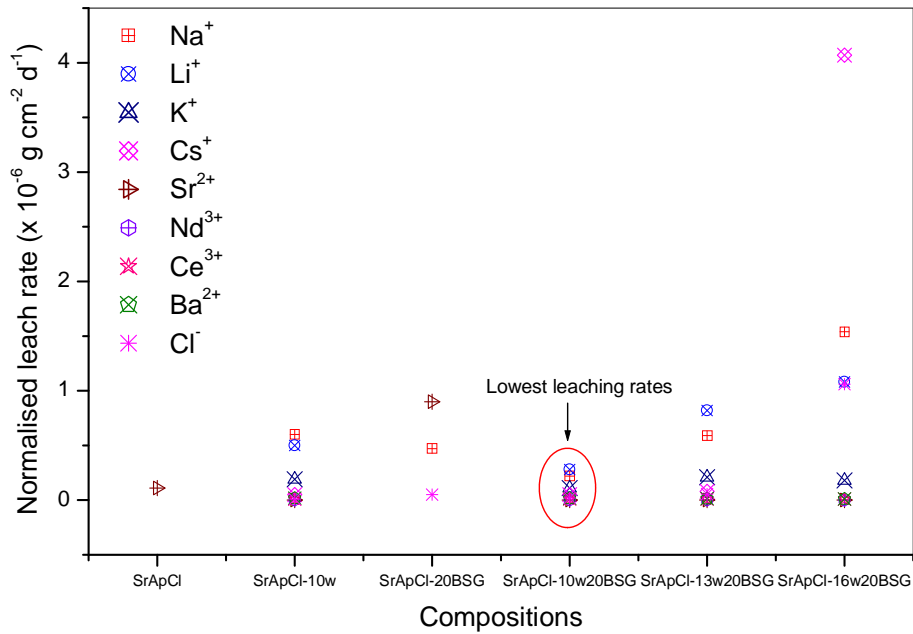


Fig. 3.5: Plot of normalised leach rates vs. compositions of glass-bonded composites

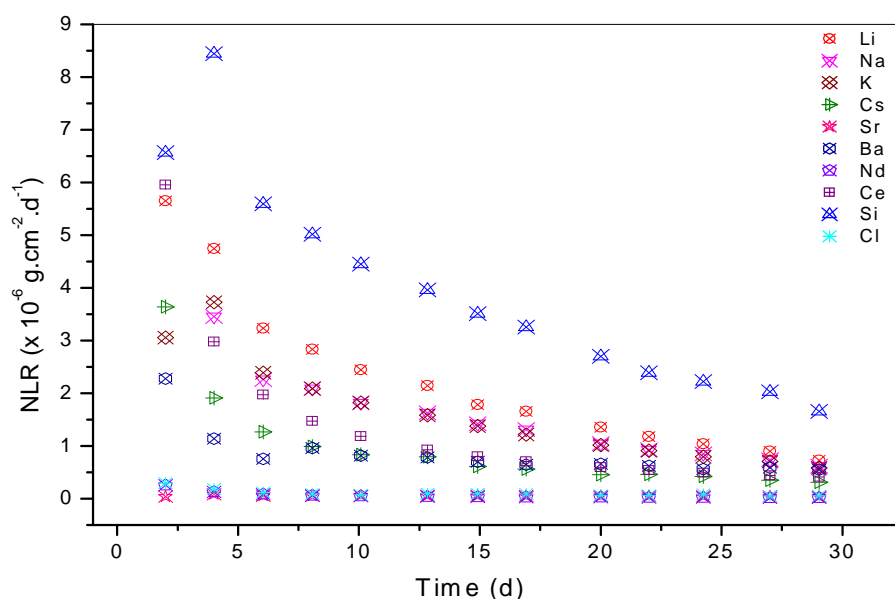


Fig. 3.6: Normalised leach rate (NLR, $\text{g cm}^{-2} \text{d}^{-1}$) vs. Time (d) for SrApCl-10w20BSG by soxhlet method

3.3.3 Thermal expansion by HTXRD

Fig. 3.7 shows the High Temperature XRD (HTXRD) patterns recorded at various temperatures (298 - 673 K) for SrApCl-13w20BSG as a typical example. The lattice constants were calculated from the XRD patterns at elevated temperatures. The lattice constants were found to increase on increasing temperature. Structural transition was not observed for the crystalline phase on heating the sample from 298 to 673 K in air. All the measurements were carried out below glass transition temperature of the composites. However, glass transition temperatures of the composites were observed above 773 K. The sample material did not react with the Pt-strip used as sample holder as well as heating element within the temperature range of measurement.

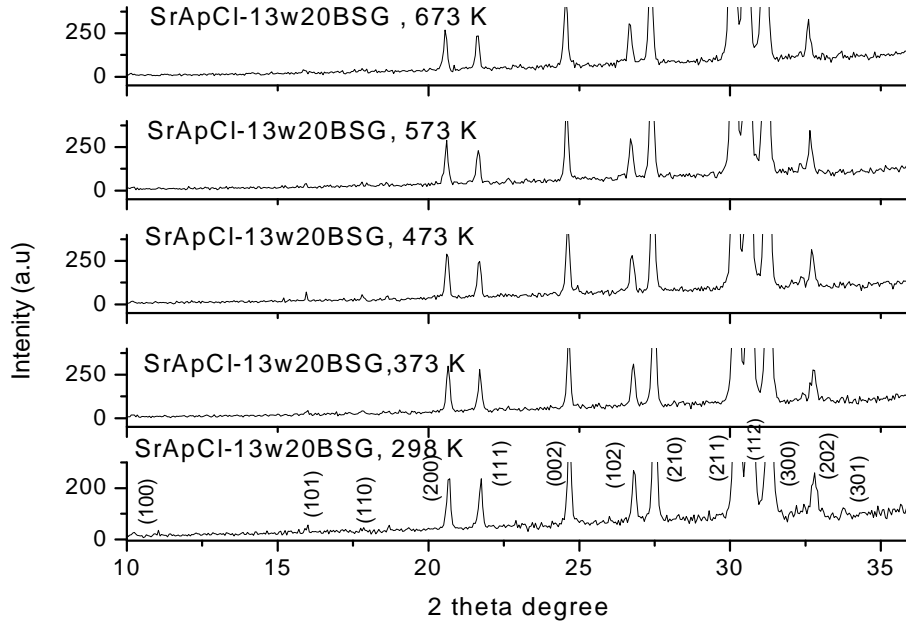


Fig. 3.7: High temperature XRD patterns of the SrApCl + 13 wt. % waste + 20 wt. % BSG composites at temperatures mentioned in the pattern

Fig. 3.8 shows the variation of lattice constant along a -axis of the unit cell. The lattice constants plotted in Fig. 3.8 shows slight decrease in a value for SrApCl-10w0BSG composition compared to pristine SrApCl. This may be attributed to the substitution of smaller cations, $r^{\text{VIII}}(\text{Li}^+) = 0.9 \text{ \AA}$, $r^{\text{VII}}(\text{Na}^+) = 1.12 \text{ \AA}$, $r^{\text{IX}}(\text{Na}^+) = 1.24 \text{ \AA}$, $r^{\text{VII}}(\text{Sr}^{2+}) = 1.21 \text{ \AA}$, $r^{\text{IX}}(\text{Sr}^{2+}) = 1.31 \text{ \AA}$ in the Sr-sublattice [32]. However, there is a slight increase in a -value for the composition SrApCl-13w20BSG above 600 K. The variation in lattice constants is within the experimental error (± 0.02). Therefore, less than 16 wt. % waste loading is possible on the basis of solid solution formation of the waste elements with Sr-chloroapatite (SrApCl) lattice.

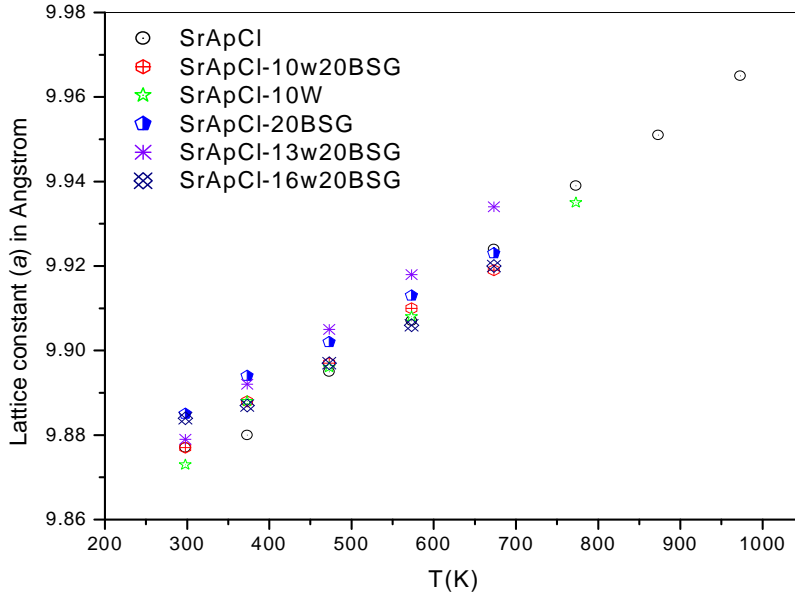


Fig. 3.8: Comparison of lattice constants (a -axis) vs. T (K) of the compositions

Similarly, the c -parameter was also measured and is shown in Fig. 3.9. SrApCl-20BSG shows higher value of c compared to c value in pristine SrApCl. This was observed when there were no waste elements added to the matrix except glass forming agents. On the contrary, when waste elements were added to the composite; a decrease in lattice constant along c -axis is observed. 10 to 13 wt. % waste loading shows a slight decrease in lattice constant compared to pristine SrApCl. However, on increasing the waste loading to 16 wt. % a significant decrease in c -value was observed. The increase in lattice constant (c -axis) for the composition SrApCl-20BSG may be attributed to the substitution of glass forming agents along the c -axis in the lattice, which is yet to be confirmed by various other experimental evidence.

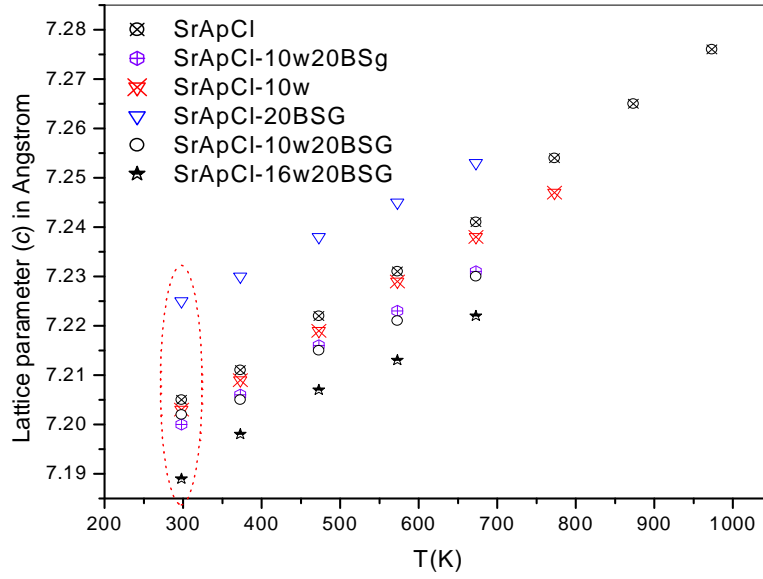


Fig. 3.9: Comparison of lattice constants (*c*) vs. *T* (K) of the compositions from HTXRD data

In Fig. 3.10, the mean coefficients of thermal expansion (CTE or α_m) vs. *T* plots along *a*-axis measured by HTXRD are shown. The coefficient of thermal expansion (α_m) was found to decrease on increasing waste element concentration into the glass bonded SrApCl composite matrices (Fig. 3.10). The α_m along *a*-axis for SrApCl is found to be $2.40(1) \times 10^{-7}$ to $9.51(2) \times 10^{-6} \text{ K}^{-1}$ in the temperature range of 300 - 700 K. The thermal expansion of pristine SrApCl was measured up to 1000 K whereas, for the glass bonded compositions thermal expansion was measured below the glass transition temperature of the composites (< 800 K). Therefore, for the sake of comparison all the values were plotted up to 700 K only. From the plots in Fig. 3.10, it was observed that CTE of the composites are found to decrease on increasing temperature. The decrease in CTE may be attributed to the interaction of substituent cations with SrApCl ceramic as well as with the borosilicate glass network

(network formers (Si) and modifiers (Na)). The ceramic (SrApCl) shows higher CTE compared to waste loaded and BSG bonded composites.

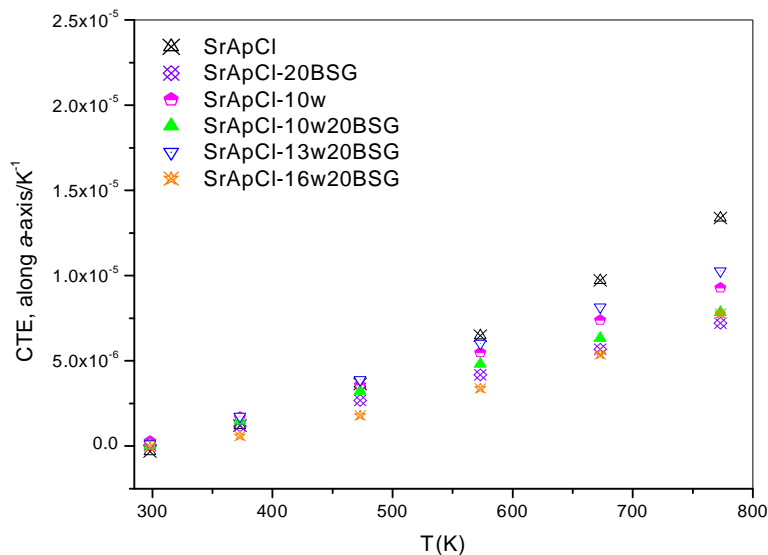


Fig. 3.10: Mean coefficient of thermal expansion (α_m) vs. T of the composites along *a*- axis from HTXRD data.

Similar trend was also observed for the % expansion along *c*-axis. The CTE vs. T plots along *c*-axis are shown in Fig. 3.11. In this case, the variation in CTE along *c*-axis is found to be less. However, CTE of SrApCl is slightly higher than that of waste loaded and glass bonded compositions above 700 K. This may be explained based on the fact, that the thermal expansion contribution of glass phase in addition to the crystalline phase (SrApCl) is not detected by XRD for the glass bonded composites. Furthermore, the substitution of waste elements having considerably lower ionic radii compared to host cation (Sr^{2+}) in the SrApCl lattice is attributed to the marginal lowering of lattice constants (*a* and *c* of the unit cell) compared to pristine SrApCl. The anticipated higher lattice expansion because of weakening of bonds due to aliovalent cation substitution into the lattice was not observed. Instead, the

lattice constants were reduced indicating the substitution of waste elements (Li^+ , K^+ *etc.*) into the SrApCl lattice for the waste loaded glass-bonded composites. The α_m along c -axis for SrApCl is found to be $9.28(1) \times 10^{-8}$ to $7.68(1) \times 10^{-6} \text{ K}^{-1}$ in the temperature range of 300 - 700 K.

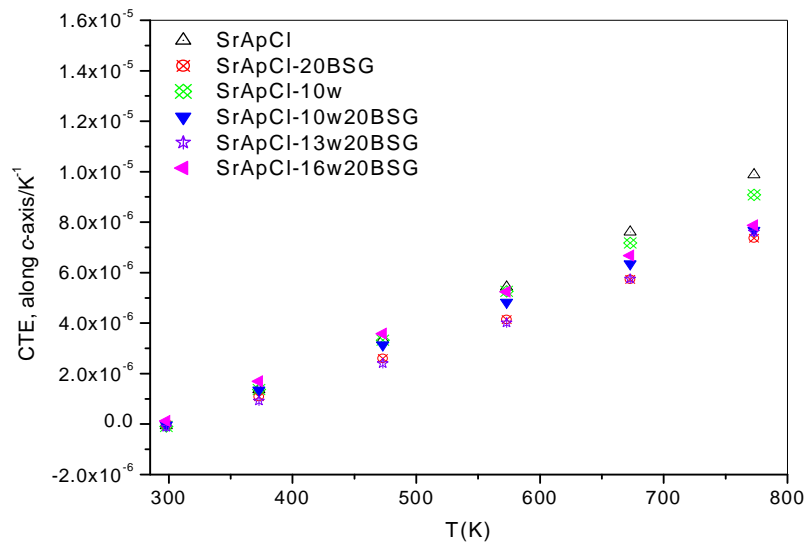


Fig. 3.11: Mean coefficient of thermal expansion (α_m) vs. T of glass composites along c -axis from HTXRD

In Fig. 3.12, a picture of the typical pellet of 10 mm height used for dilatometry measurement is shown.

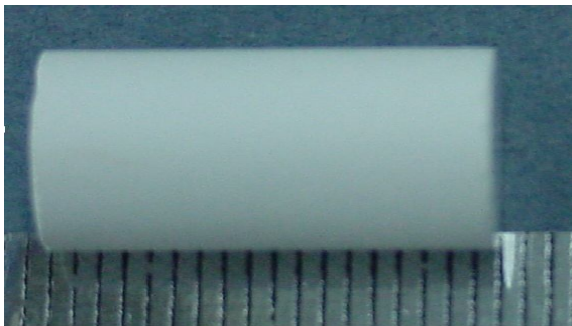


Fig. 3.12: Typical heat-treated SrApCl pellet used for thermal expansion by Push rod dilatometry

3.3.4 Thermal expansion by Thermomechanical analysis (dilatometry) and T_g measurement by TMA and DSC

In Fig. 3.13, % average linear thermal expansion of the composites measured by dilatometry is plotted. The % linear thermal expansion of SrApCl (bulk pellet) is found to be almost same for all the compositions up to 600 K. SrApCl, SrApCl-10w20BSG and SrApCl-13w20BSG compositions found to show same % thermal expansion from 300 to 900 K range of temperature. Therefore, 10 to 13 wt. % waste loading can easily be accommodated into the SrApCl-BSG matrix without anticipating any problem related to thermal expansion behavior of the waste loaded matrix. However, SrApCl + 0 waste + 20 BSG compositions showed a slightly higher % thermal expansion above 600 K compared to pristine SrApCl. This may be due to the interaction of glass forming agents (SiO_2 , B_2O_3 etc.) on the ceramic matrix and weakening of bonds of the ceramic compound. Furthermore, the lattice expansion measured by dilatometry clearly detected the combined expansion of crystalline and the glass phase of the composites. Therefore, the SrApCl expansion is the lowest among all the waste loaded compositions as anticipated. In Fig. 3.14, the instantaneous coefficient of thermal expansion (CTE) (α_i) is plotted against T (K). The plots show the variation of thermal expansion at each instant of temperature increment. The thermal expansion of SrApCl is the lowest and SrApCl-16w20BSG is the highest below the glass transition temperature of glass bonded composites. The α_m measured by dilatometry for the composites ranges from $3.80(1) \times 10^{-7}$ to $13.14(1) \times 10^{-6} \text{ K}^{-1}$ in the temperature range of 300 - 700 K. This observation on marginal increase in % thermal expansion of waste loaded composites compared to pristine SrApCl further implies the weakening of bonds in the waste loaded compositions. Thermal expansion occurs because of the anharmonic thermal vibrations of the lattice atoms leading to the

increase in interatomic distances on heating. In the case of waste loaded composites, HTXRD does not show higher expansion compared to pristine SrApCl. That may be attributed to the substitution of cations with smaller ionic radii in the place of Sr^{2+} within the solubility limit in SrApCl lattice. The lattice expansion might have been compensated by the partial contraction of the lattice because of the substitution of smaller size cations. However, the trend is reverse by dilatometry measurements. The glass network (SiO_4 -tetrahedra frame work) is weakened by the interaction of alkali elements (Li^+ , K^+ , Cs^+ *etc.*) present in the waste facilitating the formation of non-bridging oxygen's in the glass network [33]. Therefore, waste loaded-BSG bonded-SrApCl exhibited slightly higher expansion compared to pristine SrApCl by dilatometry.

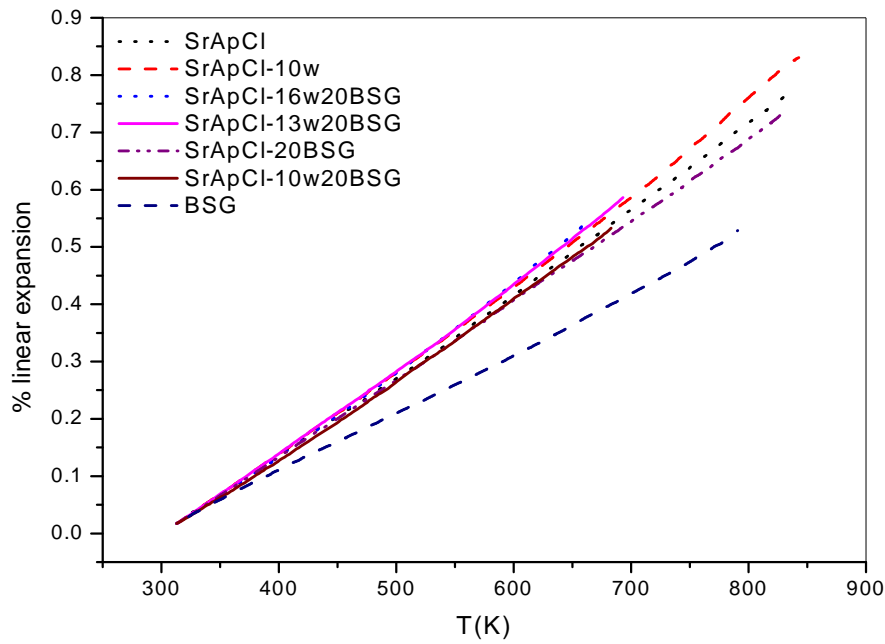


Fig. 3.13: % thermal expansion of SrApCl + x waste + 20 BSG composites by dilatometry

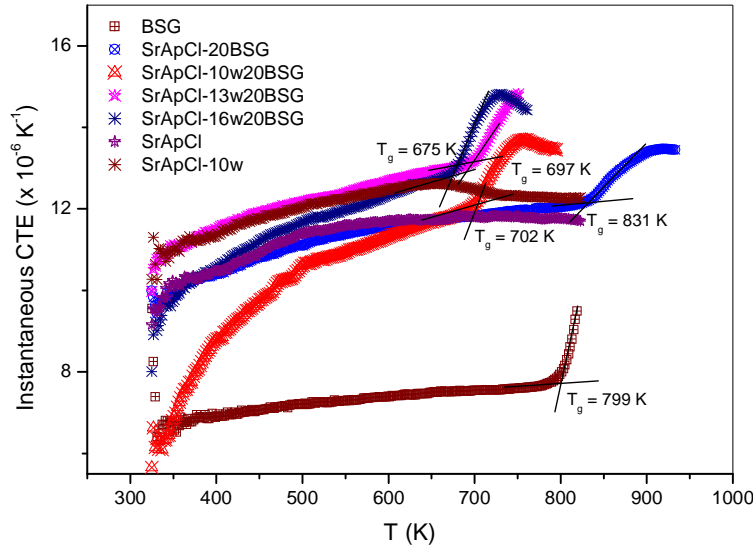


Fig. 3.14: Instantaneous CTE (α_i) vs. T showing the glass transition temperature (T_g) of glass bonded composites. SrApCl and 10 wt. % waste loaded composition does not show any glass transition

The glass transition temperature of the glass bonded compositions is shown in the Fig. 3.14. The T_g measured by thermomechanical measurements shows the correct trend for the BSG glass of nearly same composition [32, 33] and for the BSG with same composition reported in our earlier work [12, 33]. The decrease in T_g for the waste loaded composites compared to the pure BSG indicates the interaction of waste elements with the BSG matrix. In Fig. 3.14, the higher T_g value (831 K) obtained for SrApCl-20BSG composition may be due to non or little interaction of SrApCl and BSG even at elevated temperature. The T_g were also measured by DSC method (shown in Fig. 3.15) which also shows a higher value of 835 K; whereas the values found for pure BSG and SrApCl-10w20BSG were 813 K and 704 K. Dilatometry shows slightly higher T_g values for the BSG and glass-bonded composites compare to DSC method. This is due to difference in heating rate applied during the

measurement in two different methods. In dilatometry heating rate was 2 K min^{-1} , while in DSC method 10 K min^{-1} heating rate was applied. The T_g reported in the literature for pure BSG measured by Differential Scanning Calorimetry (DSC) *etc.* is nearly $813 - 830 \text{ K}$ depending on the borosilicate glass composition [34] agrees well with the measured value within the experimental error. The T_g values for glass-bonded composites are reported for the first time.

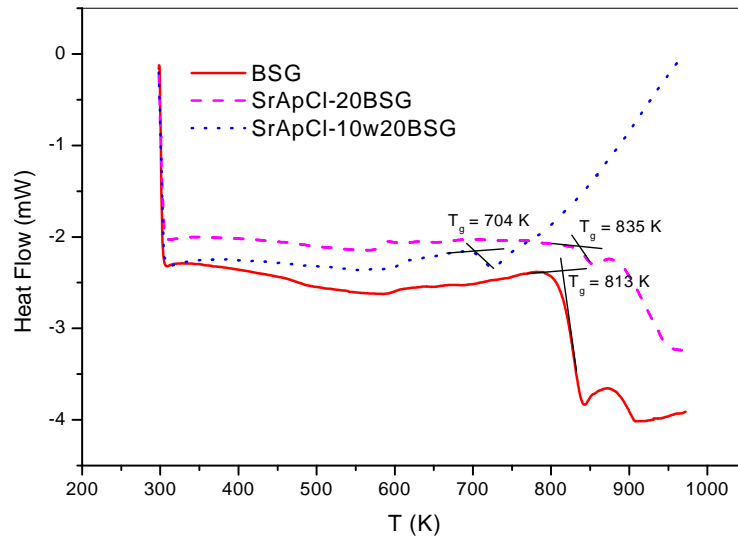


Fig. 3.15: T_g measurement BSG, SrApCl-20BSG and SrApCl-10w20BSG by DSC method

3.3.5 Enthalpy increment and heat capacity by Drop calorimetry

The enthalpy increment values of SrApCl were measured and found to be $43.93 - 334.33 \text{ J g}^{-1}$ at the temperature range $373 - 773 \text{ K}$, which were given in Table 3.4. These enthalpy increments were fitted to 4-term polynomial functions, as given in Eqn. 3.14 using the constraints (i) $(H_T^0 - H_{298K}^0)_{298} = 0$ and (ii) heat capacity of SrApCl at 298K , $(C_p)_{298K}$ was given in the literature [35]. The coefficients of the fitted equation for the enthalpy increments of SrApCl and other glass-bonded composites are given in Table 3.5. The enthalpy

increments of measured and fit values were plotted in Fig. 3.16. The measured value and fit values were in good agreement and % residuals between the measured and fit values for the measurements were found to be upto $\pm 10\%$. The % residuals were calculated as $\{(\text{measured value} - \text{fit value}) / \text{measured value}\} \times 100$. But, if we calculate the enthalpy increment of SrApCl per mole, then the relative residuals between the measured value and fit value will be less than to that of enthalpy increment measured per gram of the sample. The fit equation obtained for SrApCl is given in Eqn. 3.18.

$$H_T^0 - H_{298K}^0 = -201.9052 + 0.5010 T + 1.9637 \times 10^{-4} T^2 + 10481.2020/T \quad (3.18)$$

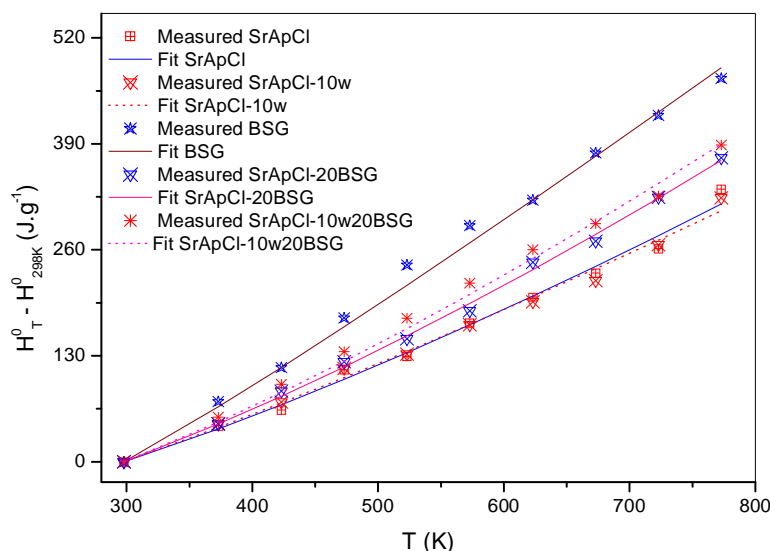


Fig. 3.16: Enthalpy increment with T (K) for SrApCl and its glass-bonded composites compare with pure BSG.

From the fitted equation, we have calculated the heat capacity (C_p), entropy (S_T) and free energy functions ($\text{FEF} = -(G_T^0 - H_{298}^0)/T$), which were given in Table 3.4. These thermodynamic functions of SrApCl were compared with the values reported in the literature for $\text{Sr}_{10}(\text{PO}_4)_6\text{Cl}_2$ by drop calorimetry [35] and DSC measurements [36] and are found to be

in good agreement. The closeness of the measured values by our instrument with that of the standard instruments (DSC and calorimetry) validates our technique.

Table 3.4: Thermodynamics functions of SrApCl

T (K)	$H_T^0 - H_{298K}^0$ Measured (J g ⁻¹)	Fit (J g ⁻¹)	Residuals (%)	$C_{p,T}$ (J g ⁻¹ K ⁻¹)	S_T (J g ⁻¹ K ⁻¹)	$-(G_T - H_{298}^0)/T$ (J g ⁻¹ K ⁻¹)
298	--	0	--	0.50	0.60	0.60
373	43.93	40.38	8.08	0.57	0.70	0.59
423	63.36	69.93	-10.37	0.61	0.76	0.60
473	112.95	101.16	10.44	0.64	0.83	0.61
523	129.11	133.87	-3.68	0.67	0.89	0.63
573	170.47	167.93	1.49	0.69	0.95	0.65
623	202.05	203.25	-0.59	0.72	1.00	0.68
673	231.55	239.78	-3.55	0.74	1.06	0.70
723	261.45	277.46	-6.12	0.77	1.11	0.73
773	334.33	316.26	5.41	0.79	1.16	0.75

Table 3.5: Coefficients of fit equations, $H_T^0 - H_{298K}^0 = a + bT + cT^2 + d/T$

Glass-bonded composites	a	b	c	d
SrApCl	-201.91	0.50	1.96E-4	10481.20
SrApCl-10w	-215.87	0.58	1.04E-4	10000.04
SrApCl-10w20BSG	-253.24	0.61	2.56E-4	14551.21
SrApCl-20BSG	-222.44	0.54	2.73E-4	11463.71
BSG	-389.65	1.06	4.84E-5	20956.53

Similarly, the heat capacity values of SrApCl-10w, SrApCl-20BSG, SrApCl-10w20BSG and BSG were evaluated from their measured enthalpy increment values and

were given in Table 3.6, 3.7, 3.8 and 3.9 respectively. The specific heat capacity values of the glass-bonded composites were plotted in Fig. 3.17. SrApCl found to show lowest specific heat capacity and BSG is showing highest specific heat capacity among the compositions shown. This may be attributed to the comparatively weak bonding characters among the constituent atoms in BSG compared to SrApCl. SrApCl is a crystalline solid whereas BSG is a super cooled liquid (amorphous solid).

Table 3.6: Enthalpy increments and heat capacity data for SrApCl-10w

T (K)	$H_T^0 - H_{298K}^0$		Residuals (%)	$C_{p,T}$ (J g ⁻¹ K ⁻¹)
	Measured (J g ⁻¹)	Fit (J g ⁻¹)		
298	--	0	--	0.53
373	46.59	42.03	9.78	0.59
423	73.32	72.03	1.77	0.61
473	114.49	103.21	9.85	0.63
523	131.95	135.39	-2.61	0.65
573	167.98	168.44	-0.27	0.67
623	196.32	202.27	-3.03	0.68
673	222.29	236.83	-6.54	0.70
723	266.18	272.07	-2.21	0.71
773	323.75	307.96	4.88	0.72

Table 3.7: Enthalpy increments and heat capacity data for SrApCl-20BSG

T (K)	$H_T^0 - H_{298K}^0$		Residuals (%)	$C_{p,T}$ (J g ⁻¹ K ⁻¹)
	Measured (J g ⁻¹)	Fit (J g ⁻¹)		
298	--	0	--	0.57
373	46.23	46.19	0.07	0.66
423	86.56	80.22	7.33	0.70
473	122.50	116.37	5.00	0.74
523	151.01	154.43	-2.26	0.78
573	185.08	194.27	-4.96	0.81
623	244.72	235.77	3.66	0.85
673	270.53	278.87	-3.08	0.88
723	324.37	323.52	0.26	0.91
773	372.64	369.70	0.79	0.94

Table 3.8: Enthalpy increments and heat capacity data for SrApCl-10w20BSG

T (K)	$H_T^0 - H_{298K}^0$		Residuals (%)	$C_{p,T}$ (J g ⁻¹ K ⁻¹)
	Measured (J g ⁻¹)	Fit (J g ⁻¹)		
298	--	0	--	0.60
373	54.60	48.78	10.66	0.70
423	94.96	84.84	10.66	0.75
473	135.13	123.15	8.87	0.79
523	176.14	163.43	7.22	0.82
573	219.23	205.50	6.26	0.86
623	260.28	249.25	4.24	0.89
673	292.12	294.57	-0.84	0.92
723	326.00	341.41	-4.73	0.95
773	388.55	389.73	-0.31	0.98

Table 3.9: Enthalpy increments and heat capacity data for BSG

T (K)	$H_T^0 - H_{298K}^0$		Residuals (%)	$C_{p,T}$ (J g ⁻¹ K ⁻¹)
	Measured (J g ⁻¹)	Fit (J g ⁻¹)		
298	--	0	--	0.85
373	73.84	67.58	8.47	0.94
423	115.63	115.72	-0.08	0.98
473	176.27	165.51	6.10	1.01
523	241.39	216.54	10.29	1.03
573	289.61	268.56	7.27	1.05
623	321.11	321.37	-0.08	1.06
673	378.86	374.87	1.05	1.08
723	424.96	428.95	-0.94	1.09
773	470.18	483.55	-2.84	1.10

The specific heat capacity was further increased when 10 wt. % simulated waste was added into SrApCl-20BSG to get SrApCl-10w20BSG. This is due to the incorporation of different alkali (Li⁺, K⁺, Na⁺ and Cs⁺), alkaline earth (Ba²⁺) and rare earth (Ce³⁺ and Nd³⁺) ions into the glass-ceramic composites. In practice, materials with higher heat capacity are desirable to withstand the deposition of decay heat released from the long lived radio-nuclides. The specific heat capacities of SrApCl and SrApCl-10w were found to be almost same at lower temperature. However, SrApCl shows higher heat capacity compared to SrArCl-10w at higher temperatures.

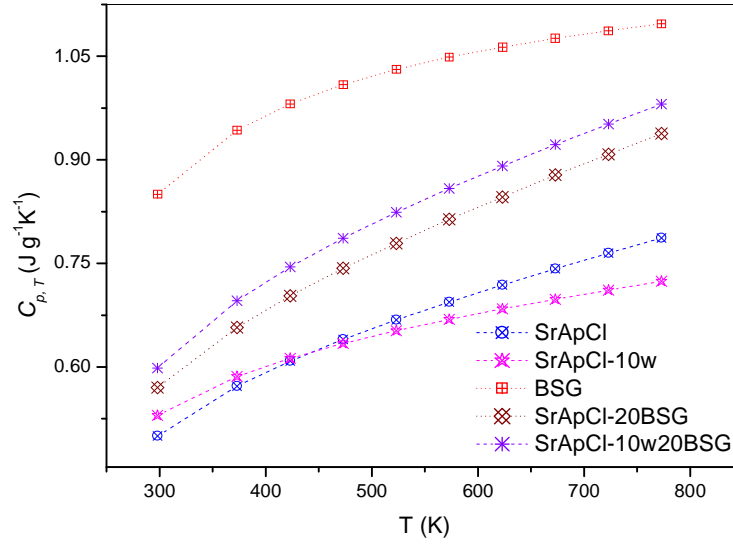


Fig. 3.17: Heat capacity vs. T (K) of SrApCl and its glass bonded composites with pure BSG

3.3.6 Electrical conductivity by DC measurement

Electrical conductivity of these glass-bonded ceramic composites was measured by DC method. The conductivity was found to be in the range of $9.90 \times 10^{-9} \text{ S cm}^{-1} - 3.2 \times 10^{-3} \text{ S cm}^{-1}$ at the temperature range $T = 425 - 1050 \text{ K}$. The conductivity of these glass-bonded composites was plotted according to the Arrhenius equation as shown in Fig. 3.18. From the Arrhenius plots, it was observed that the electrical conductivity of pristine borosilicate glass (BSG) shows highest among the other. This is due to well known ionic conductivity of Na^+ ions in the borosilicate glasses. Whereas, the conductivity of pure SrApCl and SrApCl-10w were almost same, although a slight increase of conductivity was observed for SrApCl-10w at higher temperature. As we added borosilicate glass into Sr-chloroapatite, the conductivity increases due to the glass component present in the glass-bonded composites. The trend of 10 - 16 wt. % waste loaded glass-bonded composites was $\sigma_{\text{SrApCl-10w20BSG}} < \sigma_{\text{SrApCl-13w20BSG}} < \sigma_{\text{SrApCl-16w20BSG}}$, though the difference in conductivity was not much. This is attributed to the

formation of non-bridging oxygen into the glass network and increase in current carrying modifier ions concentrations. However, the conductivity of glass-bonded composites was lower than the pristine BSG. This is because lowering of carrier ion concentration into the glass-bonded composites, where 20 wt% of the glass was used for the glass-bonded composites.

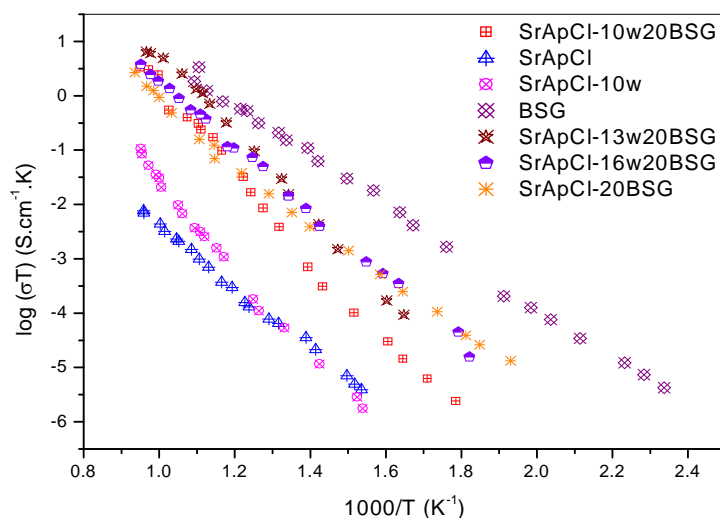


Fig. 3.18: Arrhenius plot of $\log(\sigma T)$ vs. $1000/T$ for various glass-bonded ceramic matrices

References

1. Y. I. Chang, The Integral Fast Reactor, Nucl. Tech. 88 (1989) 129-138.
2. S. Priebe, The Ceramic Waste Form Process at Idaho National Laboratory, Idaho National Laboratory, INL/CON-07-12580, July 2007.
3. M. A. Lewis, D. F. Fischer, L. J. Smith, Salt occluded zeolites as an immobilized matrix for chloride waste salt, J. Am. Ceram. Soc. 76 (1993) 2826-2832.
4. I. W. Donald, Waste Immobilization in Glass and Ceramic Based Hosts Radioactive, Toxic and Hazardous Wastes, Wiley Ltd, UK, Chapter-9, 2010, pp. 242-273.

5. P. Trocellier, Immobilization of radionuclides in single-phase crystalline waste forms: a review on their intrinsic properties and long term behavior, *Ann. Chim. Sci. Mater.* 25 (2000) 321-337.
6. E. Fleet, Y. Pan, Site Preference of Nd in Fluorapatite $[\text{Ca}_{10}(\text{PO}_4)_6\text{F}_2]$, *J. Solid State Chem.* 112 (1994) 78-81.
7. E. R. Vance, J. Davis, K. Olufson, I. Chironi, I. Karatchevtseva, I. Farnan, Candidate waste forms for immobilisation of waste chloride salt from pyroprocessing of spent nuclear fuel, *J. Nucl. Mater.* 420 (2012) 396-404.
8. G. Leturcq, A. Grandjean, D. Rigaud, P. Perouty, M. Charlot, Immobilization of fission products arising from pyrometallurgical reprocessing in chloride media, *J. Nucl. Mater.* 347 (2005) 1-11.
9. F. Audubert, J. Carpena, J. L. Lacout, F. Tetard, Elaboration of an iodine-bearing apatite Iodine diffusion into a $\text{Pb}_3(\text{VO}_4)_2$ matrix, *Solid State Ionics*, 95 (1997) 113-119.
10. A. Chartier, C. Meis, J. D. Gale, computational study of Cs immobilization in the apatites $\text{Ca}_{10}(\text{PO}_4)_6\text{F}_2$, $\text{Ca}_4\text{La}_6(\text{SiO}_4)_6\text{F}_2$ and $\text{Ca}_2\text{La}_6(\text{SiO}_4)_6\text{F}_2$, *Phys. Rev. B*, 64 (2001) 085110.
11. E. H. Oelkers, J. M. Montel, Phosphates and Nuclear Waste Storage, *Elements*, 4 [2] (2008) 113-116.
12. H. Jena, B. K. Maji, R. Asuvathraman, K. V. G. Kutty, Synthesis and thermal characterization of glass bonded Ca-chloroapatite matrices for pyrochemical chloride waste immobilization, *J. Non-Cryst. Solids*, 358 (2012) 1681-1686.

13. H. Jena, R. V. Krishnan, R. Asuvathraman, K. Nagarajan, K. V. G. Kutty, Thermal expansion and heat capacity measurements on $\text{Ba}_{10-x}\text{Cs}_x(\text{PO}_4)_6\text{Cl}_{2-8}$, ($x = 0, 0.5$) chloroapatites synthesized by sonochemical process, *J. Therm. Anal. Calorim.* 106 (2011) 875-879.
14. R. V. Krishnan, H. Jena, K. V. G. Kutty, K. Nagarajan, Heat capacity of $\text{Sr}_{10}(\text{PO}_4)_6\text{Cl}_2$ and $\text{Ca}_{10}(\text{PO}_4)_6\text{Cl}_2$ by DSC, *Thermochim. Acta*, 478 (2008) 13-16.
15. K. Sudarsanan, R. A. Young, Structure refinement and random error analysis for strontium chlorapatite, $\text{Sr}_5(\text{PO}_4)_3\text{Cl}$, *Acta Cryst. B*, 30 (1974) 1381-1385.
16. T. J. White, D. Zhili, Structural derivation and crystal chemistry of apatites, *Acta Crystallogr. B*, 59 (2003) 1-16.
17. R. Bros, J. Carpena, V. Sere, A. Beltritti, Occurrence of Plutonium and Fissiogenic REE in hydrothermal apatites in nuclear reactor 16 at Oklo (Gabon), *Radiochim. Acta*, 74 (1996) 277-282.
18. I. W. Donald, B. L. Metcalfe, S. K. Fong, L. A. Gerrard, D. M. Strachan, R. D. Scheele, A glass-encapsulated calcium phosphate waste form for the immobilization of actinide-, fluoride-, and chloride containing radioactive wastes from the pyrochemical reprocessing of plutonium metal, *J. Nucl. Mater.* 361 (2007) 78-93.
19. J. M. Juoi, M. I. Ojovan, Characterization and durability of glass composite waste from immobilising spent clinoptilolite, WM'07 conference, Tucson, AZ, 2007.
20. N. V. Ojovan, I. V. Startceva, A. S. Barinov, M. I. Ojovan, D. H. Bacon, B. P. McGrail, J. D. Vienna, Product consistency test of fully radioactive high-sodium content borosilicate glass K-26, *Symp. Proc. Mat. Res. Soc.* 824, 2004.

21. M. F. Simpson, K. M. Goff, S. G. Johnson, K. J. Bateman, T. J. Battisti, K. L. Toews, S. M. Frank, T. L. Moschetti, T. P. O'Holleran, A Description of the Ceramic Waste Form Production Process from the Demonstration Phase of the Electrometallurgical Treatment of EBR-II Spent Fuel, Nucl. Technol. 134 (2001) 263-277.
22. C. Y. Ho, R. E. Taylor (Eds.), Thermal Expansion of Solids, ASM International, Materials park, Ohio, USA, 1998, Chapter 1-2, pp. 1-131.
23. H. Czichos, T. Saito, E. Smith (Eds.), Thermal Expansion, Springer Handbook of Materials Measurement Methods, 2006, Chapter – 2, pp. 415.
24. K. V. G. Kutty, R. Asuvathraman, M. V. Krishnaiah, V. Ganesan, R. Parthasarathy, D. S. Subalakshmi, B. Suhasini, K. C. Srinivas, K. A. Gopal, P. V. Kumar, Design, fabrication and commissioning of a push rod dilatometer for thermal expansion studies on solids, IGC Report No. 283, 2006, pp. 23.
25. E. F. Kaelble, in: E. F. Kaelble (Ed.), MgO Thermal Expansion, Handbook of X-rays, Mc-Graw Hill, Chapter -13, 1967, pp. 15.
26. J. Belle, R. M. Berman, in: J. Belle, R. M. Berman (Eds.), Thorium Dioxide: Preparation and Nuclear Applications, Thermal Expansion Chapter, Govt. printing office, Washington, D.C, USA, 1984, pp. 169.
27. G. Grimvall, Thermophysical properties of materials, Revised Edition, North-Holland, Elsevier Science B. V. 1999.
28. M. V. Krishnaiah, Study of the thermophysical properties of some materials of interest in nuclear technology, PhD Thesis, University of Madras, 2000, pp. 96–104.
29. O. Knacke, O. Kubaschewski, K. Hesselmann, Thermophysical properties of Inorganic substances, 2nd ed. Berlin: Springer-Verlag, 1991.

30. B. K. Maji, H. Jena, R. Asuvathraman, K. V. G. Kutty, Electrical conductivity and thermal expansion behavior of MMoO_4 ($\text{M} = \text{Ca}, \text{Sr}$ and Ba), *J. alloys compd.* 640 (2015) 475-479.
31. K. Sudarsanan, R. A. Young, Powder diffraction File (PDF) number # 70-1007 for strontium chloride phosphate, *Acta Crystallography Sec. B*, 30 (1974) 1381.
32. R. D. Shannon, Revised effective ionic radii and systematic studies of interatomic distances in halides and chalcogenides, *Acta Cryst. A*, 32 (1976) 751-767.
33. H. Jena, R. Asuvathraman, K. V. G. Kutty, P. R. V. Rao, Comparison of electrical conductivity and thermal properties of borosilicate glass with and without simulated radioactive waste, *J. Therm. Anal. Calorim.* 115 [1] (2014) 367-374.
34. I. Avramov, T. S. Vassilev, I. Penkov, The Glass Transition Temperature of Silicate and Borate Glasses, *J. Non-Cryst. Solids*, 351 (2005) 472-476.
35. R. Babu, H. Jena, K. V. G. Kutty, K. Nagarajan, Thermodynamic functions of $\text{Ba}_{10}(\text{PO}_4)_6\text{Cl}_2$, $\text{Sr}_{10}(\text{PO}_4)_6\text{Cl}_2$ and $\text{Ca}_{10}(\text{PO}_4)_6\text{Cl}_2$, *Thermochimica Acta*, 526 (2011) 78-82.
36. R. V. Krishnan, H. Jena, K. V. G. Kutty, K. Nagarajan, Heat capacity of $\text{Sr}_{10}(\text{PO}_4)_6\text{Cl}_2$ and $\text{Ca}_{10}(\text{PO}_4)_6\text{Cl}_2$ by DSC, *Thermochimica Acta*, 478 (2008) 13-16.

Synthesis, characterization and thermophysical properties on alumino borosilicate glass (AlBSG)-bonded strontium chloroapatite composites with simulated pyrochemical chloride waste

4.1 Introduction

Apatites, $M_{10}(PO_4)_6Cl_2$, ($M = Ca, Sr, Ba \text{ etc.}$) are known to be used for the immobilization of chloride waste containing radioactive elements [1-11] and previous chapter describes the combination of Sr-chloroapatite encapsulated in borosilicate glass (BSG), which can immobilize most of the radwaste elements in the composite matrix (glass-bonded composites), thus utilizing the immobilizing efficiency of both the ceramic phase and BSG [12, 13]. However, to see the effect of glass composition on the waste loading, chemical durability and thermophysical properties, alumino borosilicate glass (AlBSG)-bonded Sr-chloroapatite (SrApCl-10w20AlBSG) were also studied. The present chapter deals with the synthesis and characterization of pristine AlBSG and its glass-ceramic composite with strontium chloroapatite (SrApCl-10w20AlBSG). The products were characterized by XRD studies. The chemical durability of these glass-bonded composites was carried out by soxhlet method. High temperature XRD (HTXRD) studies were carried out to investigate the formation of new crystalline phases if any during in situ heating of the samples (composites) at elevated temperatures. HTXRD also reveals the expansion of composite materials along a - and c -axis. The percentage linear thermal expansion and glass transition temperatures (T_g) were measured by dilatometry. Heat capacity (C_p) and T_g of the composites were also measured by differential scanning calorimetry (DSC) in the temperature range of 300 - 560 K. T_g measured by thermomechanical (TMA) or dilatometry is compared with the T_g measured by DSC technique. C_p values of these glass bonded composites were also measured

by drop calorimetry at higher temperature upto 773 K and compared with the values of DSC measurement. The results on thermal expansion, C_p and T_g on these composites are reported for the first time.

4.2 Experimental

4.2.1 Preparation and characterization of Alumino borosilicate glass (AlBSG) and its glass-bonded ceramic composite with Sr-Chloroapatite

Alumino borosilicate glass (abbreviated as AlBSG) was prepared by mixing glass forming reagents (SiO_2 {55 wt. % or 58.08 mol %} + B_2O_3 {13.9 wt. % or 12.63 mol %} + Na_2O {6.5 wt% or 6.65 mol %} + Al_2O_3 {9.7 wt. % or 6.04 mol %} + CaO {13.5 wt. % or 15.28 mol %} + K_2O {0.5 wt. % or 0.54 mol %} + MgO {0.4 wt. % or 0.63 mol %} + SrO {0.1 wt. % or 0.06 mol %} + ZrO_2 { 0.1 wt. % or 0.05 mol %}) [14], the mixture was homogenized by grinding in a mortar-pestle for half-an-hour and then calcined at 673 K in an alumina crucible for 1½ h. The calcined mixture was heated at 1473 K / 2h in the same alumina crucible in air ambience and quenched to room temperature. The products were then characterized by powder-XRD to confirm the absence of any crystalline phases present in the final product.

Strontium chloroapatite ($\text{Sr}_{10}(\text{PO}_4)_6\text{Cl}_2$, abbreviated as SrApCl) and its alumino borosilicate glass-bonded composites with 10 wt. % simulated chloride waste were prepared by mixing apatite (SrApCl): pyrochemical waste (W): glass (AlBSG) in the mass ratio of 70:10:20 respectively. Instead of directly using SrApCl for the preparation of composites, the stoichiometric concentrations of apatite-forming reagents such as $\text{Sr}(\text{OH})_2$, $\text{NH}_4\text{H}_2\text{PO}_4$ and NH_4Cl were used for the preparation of SrApCl. Then 10 wt. % of simulated chloride waste (LiCl /31.92, KCl /39.01, NaCl /11.23, CsCl /1.74, BaCl_2 /1.38, CeCl_3 / 2.63, NdCl_3 /12.08 in wt.

%) was mixed with 20 wt. % of glass-forming reagents. All the reagents were mixed together and ground thoroughly, and the mixture was heated at 773 K / 5 h and subsequently heated at 1023 K for 5 h in air. The products were characterized by powder XRD.

4.2.2 Leaching studies on the simulated waste loaded samples by Soxhlet method

Comprehensive leaching studies were done on the composites under soxhlet condition at 363 K for 28 days. The details of this method were also described in chapter-2. The analysis of the leachate solutions were done by AAS for alkali and alkaline earth elements; ICP-OES for rare earth elements and Ion Selective Electrode for Cl.

The normalised leach rate (NLR, in $\text{g cm}^{-2} \text{d}^{-1}$) of each element present in composites were calculated from the concentration of species such as Cl, Li, Na, K, Cs, Sr, Ba, Nd, Ce *etc.* present in the leachate solution, using the following equation [15, 16].

$$\text{NLR (g cm}^{-2} \text{d}^{-1}) = \frac{A_i \times V}{f_i \times S \times t} \quad (4.1)$$

Where, A_i = concentration of the i^{th} species in the leachate solution ($\mu\text{g/ml}$), V = volume of distilled water taken for analysis (ml), f_i = mol fraction of i^{th} element / species, S = surface area (cm^2) and t = time (d). The normalized leach rates obtained for these composites were close to the values reported in the literature ($10^{-6} \text{ g cm}^{-2} \text{d}^{-1}$) [17, 18] for various known matrices and are within the acceptable limit.

4.2.3 Thermal expansion measurements on the glass bonded composites by high temperature X-ray diffraction (HTXRD)

The % linear axial expansion of the powders was measured by using Philips X'pert-Pro MPD model XRD machine with high temperature attachment as described in chapter-3.

The XRD patterns of the samples were recorded at room temperature (RT) then the temperature of the sample was increased to 373 K, 473 K, 573 K and 673 K by programmed heating and cooling with a heating / cooling rate of 5 K min⁻¹. XRD pattern of the sample was recorded at preset temperatures. The lattice constants of the samples were calculated by using X'pert Plus software supplied by Philips. The % linear expansion along *a*-axis and *c*-axis was measured by using the following formula [19, 20].

$$\% \text{ expansion along } a - \text{axis} = \frac{a_{673} - a_{RT}}{a_{RT}} \times 100 \quad (4.2)$$

$$\text{Similarly; } \% \text{ expansion along } c - \text{axis} = \frac{c_{673} - c_{RT}}{c_{RT}} \times 100 \quad (4.3)$$

The mean or average coefficient of thermal expansion (CTE = α_m) was calculated by using the following formula

$$\text{Along } a - \text{axis: CTE} = \frac{a_{673} - a_{RT}}{a_{RT}} \times \frac{1}{\Delta T} \quad (4.4)$$

$$\text{along } c - \text{axis: CTE} = \frac{c_{673} - c_{RT}}{c_{RT}} \times \frac{1}{\Delta T} \quad (4.5)$$

4.2.4 Thermal expansion and glass transition temperature (T_g) measurements by dilatometry

Thermal expansion and glass transition temperature measurements on pellets of 10 mm diameter and 10 mm height were carried out by dilatometry in the temperature range 323 - 800 K in air, by using a home-built apparatus as described in details at chapter-3 [21]. Percentage linear thermal expansion for each composition was measured in the temperature range below the glass transition temperature of the encapsulated glass phase. The % linear expansion was calculated by using the following formula [19, 20].

$$\text{Percentage linear expansion} = \frac{\Delta L}{L_0} \times 100 \quad (4.6)$$

Where, ΔL = change in length and L_0 is different from L_1 . L_0 is the original length of the pellet at room temperature.

The average or mean coefficient of linear thermal expansion (CTE) of the matrices was measured below the glass transition temperature of the glass phase using the formula

$$\text{CTE} = \alpha_m = \frac{\Delta L}{L_0} \times \frac{1}{\Delta T} \quad (4.7)$$

Where, ΔL = change in length = $L_{i+1} - L_1$, L_0 = length of the pellet at room temperature, $\Delta T = T - T_i$ = change in temperature in K, where T = highest temperature of each measurement.

The instantaneous coefficient of thermal expansion (α_i) was determined by using the following formula [19, 20].

$$\alpha_i = \frac{1}{L_0} \times \frac{dL}{dT} = \frac{1}{L_0} \times \frac{L_{i+1} - L_1}{T_{i+1} - T_1} \quad (4.8)$$

Where, L_0 = length of the sample at room temperature, L_{i+1} = length of the pellet when temperature of the sample is T_{i+1} , L_1 = length of the sample at temperature T_1 . The onset of the instantaneous CTE vs. T (K) will give the glass transition temperatures (T_g) of the corresponding glass-bonded Sr-chloroapatites composites.

4.2.6 Glass transition temperature (T_g) and heat capacity (C_p) measurements by DSC

The measurements on glass transition temperatures and heat capacity were carried out using differential scanning calorimeter (DSC) (Model No.: DSC821e/700 of M/s. Mettler Toledo GmbH, Switzerland) as described in chapter-3. The T_g values determined from DSC was then compared with the values obtained from dilatometry measurement.

4.2.5 Enthalpy increment measurement by Drop Calorimetry

Enthalpy increments of these glass-bonded ceramic composites were measured by using a home built drop calorimeter [22, 23] at the temperature range of 373 – 773 K with a step size of 50 K as described in chapter-3.

The enthalpy increment data were fitted to an equation (Eqn. 4.9) of the form

$$H_T^0 - H_{298K}^0 = a + bT + cT^2 + d/T \quad (4.9)$$

, using the non-linear least square fitting program written in Matlab software. Two linear constraints (i) $(H_T^0 - H_{298K}^0)_{298} = 0$ and (ii) $(\frac{d}{dT}(H_T^0 - H_{298K}^0))_{298} = (C_p)_{298}$ were imposed on the coefficients to get a meaningful fitting. The heat capacity, C_p was derived from the enthalpy increment data by differentiating the fitted equation (eqn. 4.9) as given in Eqn. 4.10.

$$C_p = b + 2cT - d/T^2 \quad (4.10)$$

The heat capacity values obtained from drop calorimetry were then compared with C_p values measured by DSC method.

4.2.6 Electrical conductivity measurement by DC technique

The electrical conductivity measurements of the prepared glass (AlBSG) and its glass-bonded composite (SrApCl-10w20AlBSG) were carried out by DC techniques [24]. Cylindrical pellets of these pristine glass was prepared by melting the well characterized glass at 1473 K and then the melt was transferred or poured into a graphite crucible (12 mm dia and 15 mm height) to fabricate pellets of required dimension for the electrical conductivity measurements. The graphite crucible was cut opened to remove the glass pellet. These pellets (10 mm diameter and 6 mm length) were annealed at 800 K in a platinum crucible for 15 h in air. The pellets were characterized by powder-XRD once again to confirm amorphous character and subsequently used for electrical resistivity measurements.

Whereas, in case of measurements of electrical conductivity of glass-bonded ceramic composites, the pellets (10 mm dia and 3 mm height) were fabricated and subsequently heated to 1073 K for 10 h in air ambience. The pellets were characterized by powder-XRD once again to confirm the presence crystalline Sr-chloroapatite phase in the composite and used for electrical resistivity measurements. The details of the experimental procedure were given in chapter-3. The conductivity of samples was calculated using the formula as given in Eq. 4.11.

$$\sigma = \frac{L}{A} \times \frac{1}{R} \quad (4.11)$$

Where, σ = conductivity (S cm^{-1}), R = resistance (ohms), L = length or thickness (cm) and A = cross sectional area of the pellet (cm^2).

4.3 Results and Discussions

4.3.1 Characterization by powder-XRD

The XRD patterns of pure strontium chloroapatite (SrApCl), aluminoborosilicate glass (AlBSG) and SrApCl-10w20AlBSG were given in Fig. 4.1. From the XRD patterns, it was observed that Sr-chloroapatite is the crystalline phase present in SrApCl as well as in SrApCl-10w20AlBSG, whereas an amorphous glass phase was observed in aluminoborosilicate glass. However, we did not observe any peak corresponding to glass phase in glass-bonded ceramic composite. This may be due to the presence of crystalline phase in SrApCl-10w20AlBSG and the peak corresponding to glass phase was buried in the background. These XRD patterns were compared with the standard JCPDS patterns of strontium chloroapatite and lattice constants of both the pure strontium chloroapatite as well as SrApCl-10w20AlBSG were calculated with the help of X'pert pro software package that are given in Table 4.1 [25].

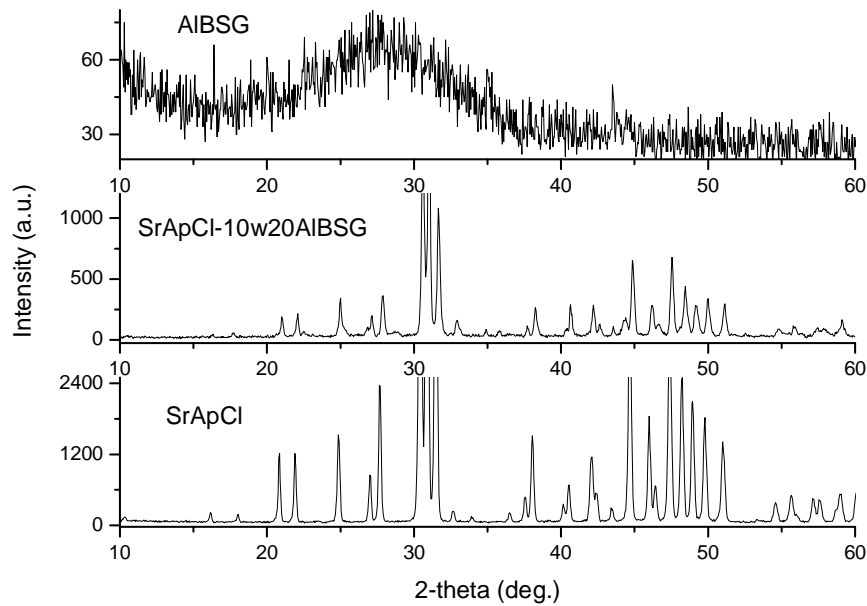


Fig. 4.1: Room temperature XRD patterns of SrApCl, SrApCl-10w20AlBSG and AlBSG

Table 4.1: Lattice constants calculated from the XRD patterns of $\text{Sr}_{10}(\text{PO}_4)_6\text{Cl}_2$ and waste-loaded glass-bonded composites. Crystal system: Hexagonal; SG = $\text{P6}_3/\text{m}$

Composites nominal composition	Lattice constants of crystalline phase in the composite (sample powders heat-treated at 1023 K, XRD recorded at room temperature)
SrApCl	$a = 9.858(2)$, $c = 7.177(2)\text{\AA}$, $\alpha = 90^\circ$, $\gamma = 120^\circ$, $V/10^6 = 604.02 \text{ pm}^3$
SrApCl-10w20AlBSG	$a = 9.863(1)$, $c = 7.184(1)\text{\AA}$, $\alpha = 90^\circ$, $\gamma = 120^\circ$, $V/10^6 = 605.38 \text{ pm}^3$

4.3.2 Leaching studies by soxhlet method

The leaching studies were done by using Soxhlet method and leachate concentration of various elements was measured by various analytical methods like AAS for alkali and alkaline earth elements, ICP-OES for rare earth elements and Ion chromatography for chloride. Then normalised leach rates of various species were calculated with time and was

given in Fig. 4.2. The normalised leach rate was observed to be in the order of 10^{-2} to 10^{-4} g $\text{cm}^{-2} \text{d}^{-1}$ and the normalised leach rate decreases with time (d).

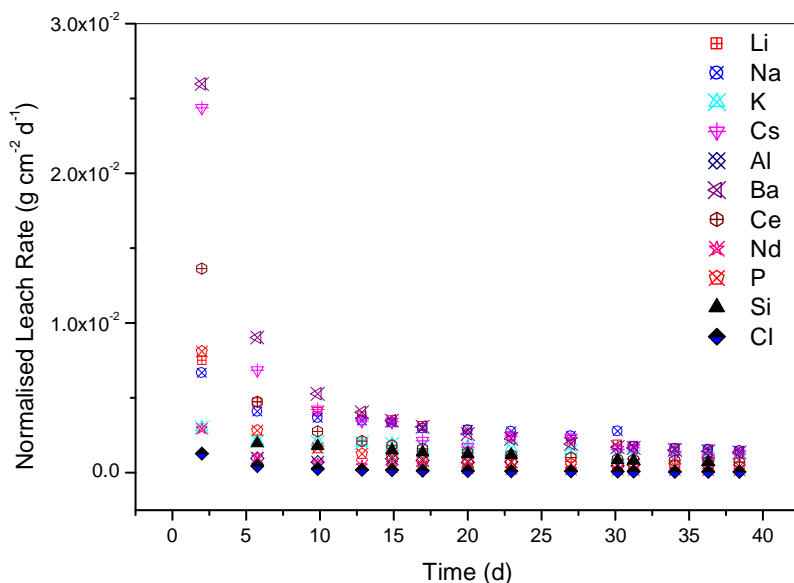


Fig. 4.2: Normalised leach rate with time for SrApCl-10w20AlBSG

4.3.3 Thermal expansion by HTXRD

Fig. 4.3 shows the High Temperature XRD (HTXRD) patterns recorded at various temperatures (298 - 673 K) for SrApCl-10w20AlBSG. The lattice constants were calculated from the XRD patterns at elevated temperatures. The lattice constants were found to increase on increasing temperature. Structural transition was not observed for the crystalline phase on heating the sample from 298 to 673 K in air. All the measurements were carried out below glass transition temperature of the composites. However, glass transition of the composites was observed above 673 K. The material did not react with the Pt-strip used as sample holder as well as heating element within the temperature range of measurement.

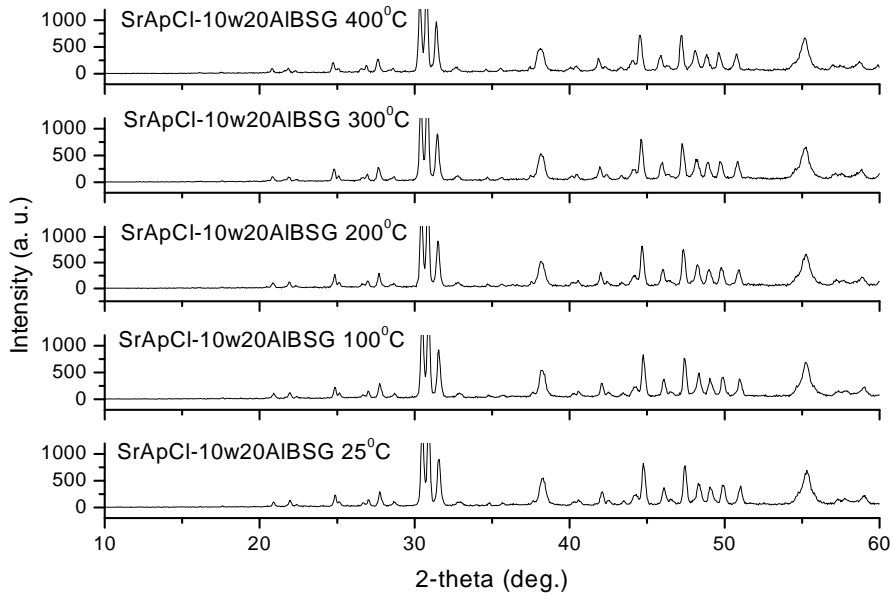


Fig. 4.3: HT-XRD patterns of SrApCl-10w20AlBSG at various temperatures

Fig. 4.4 shows the variation of lattice constant along a -axis of the unit cell. The lattice constant shows an increase with the increase in temperature. These values were fitted to a second order polynomial and the fitted equation found to be $a / \text{\AA} = 9.85 + 1.50\text{E}^{-5} T + 8.38\text{E}^{-9} T^2$ with $R^2 = 0.995$. The coefficient of thermal expansion along the a -axis was found to be $2.44(1) \times 10^{-6} \text{ K}^{-1}$ at the temperature range of 298 - 673 K.

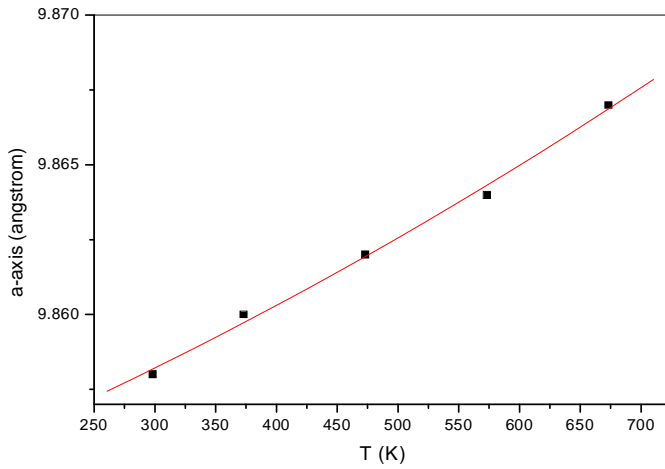


Fig. 4.4: lattice parameter (a -axis) expansion with T (K)

Similarly, the c -parameter was also measured at the temperature range $T = 298 - 673$ K as shown in Fig. 4.5. These values were also fitted to a second order polynomial and the fitting equation found to be $c / \text{\AA} = 7.13 + 1.02\text{E}^{-4} T - 3.44\text{E}^{-9} T^2$ having coefficient of determination, $R^2 = 0.998$. The coefficient of thermal expansion along the c -axis was found to be $14.16(1) \times 10^{-6} \text{ K}^{-1}$ at the temperature range of $T = 298 - 673$ K.

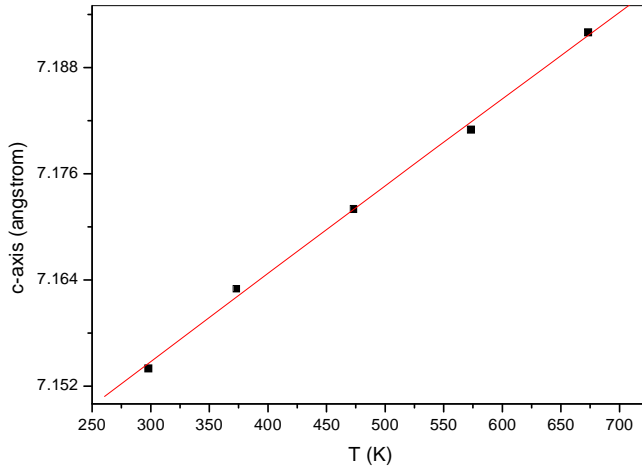


Fig. 4.5: Lattice parameter (c -axis) expansion with T (K) by HTXRD

Volume expansion of the unit cell of SrApCl-10w20AlBSG was also calculated by using the hexagonal unit cell volume and given in Fig. 4.6. Expansion of unit cell were fitted to a second order polynomial and found to be $V / \text{\AA}^3 = 598 + 0.01 T - 4.3\text{E}^{-7} T^2$ having $R^2 = 0.996$.

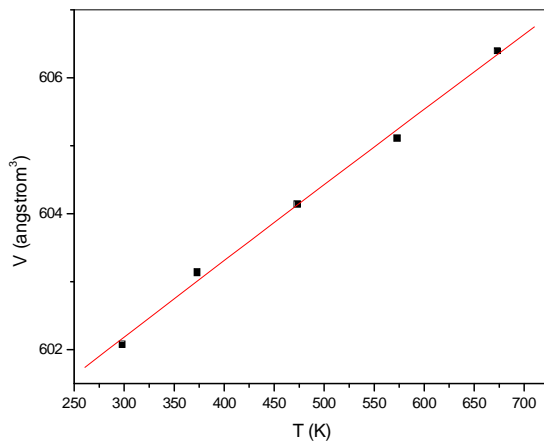


Fig. 4.6: Volume expansion with T (K) by HTXRD

4.3.4 Thermal expansion and T_g measurement by Dilatometry

The percentage (%) linear expansion for SrApCl, SrApCl-10w20AlBSG and AlBSG was measured in the temperature range below the glass transition temperature of the glass phase. The % linear thermal expansion was calculated by using the formula [19, 20] as shown in Eq. 4.6, the average coefficient of thermal expansion (CTE) of the compounds was calculated by using the formula shown in Eq. 4.7.

The glass transition temperature of the pellets was investigated by measuring the thermal expansion behavior of the composites slightly beyond the glass transition temperature and well below the softening point of the glass. The instantaneous coefficient of thermal expansion (α_i) was measured by using the formula given in Eq. 4.8.

The % linear thermal expansion of the glass-bonded composites is shown in Fig. 4.7. The % thermal expansion for glass-bonded ceramic composite is the highest among the pure ceramic and glass compositions. The coefficients of thermal expansion of these composites were found to be $12.91 \pm 0.25 \times 10^{-6}$, $14.5 \pm 0.29 \times 10^{-6}$, and $9.90 \pm 0.18 \times 10^{-6} \text{ K}^{-1}$ for SrApCl, SrApCl-10w20AlBSG and AlBSG respectively. From the thermal expansion measurements, it was observed that waste-loaded strontium chloroapatite with aluminoborosilicate glass bonding showed the highest thermal expansion compared to the parent glass or ceramic. This may be attributed to the effect of amorphous glass rigid network than that of pure ceramic or waste loaded glass-bonded ceramic compositions. The glass transition temperature of these composites were also measured from dilatometry experiment from the onset of instantaneous coefficient of thermal expansion vs. T (K) plot and found to be $710 \pm 5 \text{ K}$ for SrApCl-10w20AlBSG and $818 \pm 5 \text{ K}$ for pristine ALBSG as shown in Fig. 4.8 and in Table 4.2. The values shown are the T_g -onset [26]. This indicates the comparatively higher rigidity of pure

aluminoborosilicate glasses compared to glass-bonded ceramic composites as formation of non-bridging oxygen in glass network is obvious with the addition of waste elements as a modifier.

The glass transition temperatures (T_g) of SrApCl-10w20AlBSG and AlBSG were measured by dilatometry and DSC. The values obtained from these measurements were tabulated in Table 4.2. The plots of instantaneous coefficient of thermal expansion (Inst. CTE) vs. T (K) will give the T_g -onset values for dilatometry measurement; similarly, for DSC measurements T_g -onset was taken in the DSC scan (*i.e.* heat flow vs. T (K)) as shown in Fig. 4.8. The T_g values were found to be 820 ± 4 and 735 ± 4 K in DSC methods, whereas 818 ± 5 and 710 ± 5 K in dilatometry technique for AlBSG and SrApCl-10w20AlBSG respectively. Lower the thermal expansion, higher will be its glass transition temperatures and vice versa. The glass transition temperatures obtained from DSC and dilatometry are agreed well with slight variation in their values. The variation may be attributed due to the different heating rates applied in two different methods (heating rate in DSC was 10 K min^{-1} ; while in dilatometry, it was 2 K min^{-1}) or two different methods of measurement techniques. The glass transition temperature of AlBSG is higher than that of glass-bonded ceramic composite (SrApCl-10w20AlBSG). This may be attributed to the formation of non-bridging oxygen's on the addition of waste elements as a modifier to the glass-bonded ceramic composite compared to the pristine AlBSG. The glass transition temperatures of these pure glass and glass-bonded ceramic were measured for the first time.

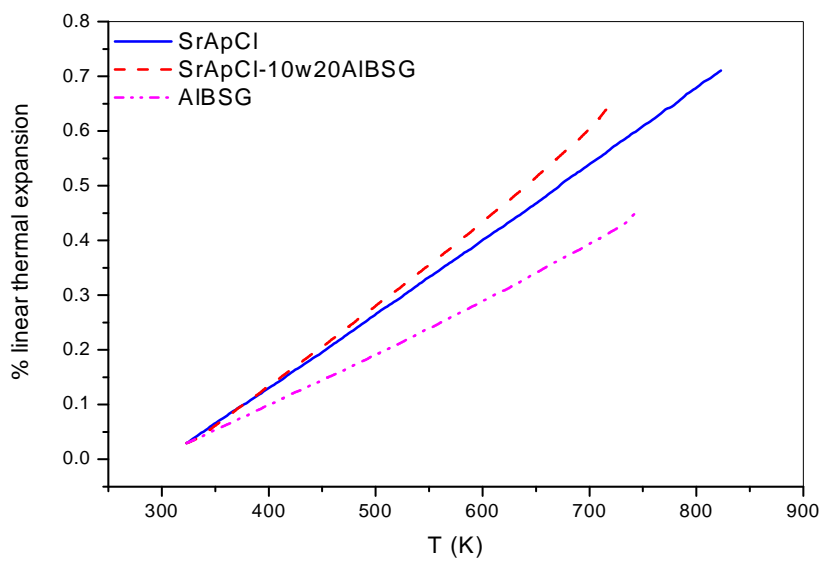


Fig. 4.7: % TE vs. T (K) for SrApCl, SrApCl-10w20AlBSG and AlBSG by dilatometry

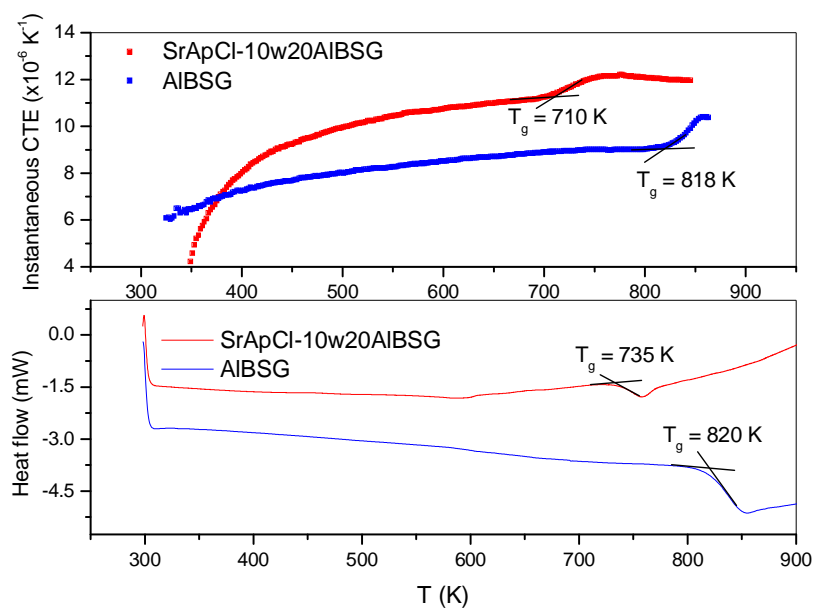


Fig. 4.8: Comparison of glass transition temperature (T_g) for SrApCl-10w20AlBSG and AlBSG

Table 4.2: comparison of T_g values by DSC and dilatometric method for AlBSG and SrApCl-10w20AlBSG

Glass Compositions	T_g by DSC measurement (K)	T_g by Dilatometry measurement (K)	Literature values (K)
AlBSG	820 \pm 4	818 \pm 5	1023* (SP)
SrApCl-10w20AlBSG	735 \pm 4	710 \pm 5	--

SP*= Softening point, T_g not available in the literature

4.3.5 Enthalpy increments and C_p measurement by Drop calorimetry

The enthalpy increment values of pure SrApCl, SrApCl-10w20AlBSG, and pristine AlBSG were measured at the temperature range $T = 373 - 773$ K by drop calorimetry and were given in Table 4.3 and 4.4 respectively. The % difference between the measured value and the fit values were observed to be upto $\pm 10\%$. These enthalpy increments were fitted to 4-term polynomial functions, $H_T^0 - H_{298K}^0 = a + bT + cT^2 + d/T$ using the constraints (i) $(H_T^0 - H_{298K}^0)_{298K} = 0$ and (ii) heat capacity of glass and glass-bonded ceramic composites at 298K, $(C_p)_{298K}$. C_p at 298 K was calculated according to the Neumann-Kopp rule using the heat capacity values of Sr-apatite, simulated waste form and glass forming reagents investigated and reported in our earlier work where heat capacity of these composites were measured by DSC method [29]. The coefficients of fit equation for the enthalpy increments of waste loaded glass-ceramic composites were given in Table 4.5. The enthalpy increments of measured and fit values were plotted in Fig. 4.9. From the enthalpy increment plots, it was observed that there is a good agreement between the measured values and the fit values. The heat capacity of the composites were then computed at the temperature range $T = 298 - 773$ K by first derivative of the fitted enthalpy increment equation and were plotted in Fig. 4.10. The calculated heat capacity values were given in Table 4.3, 4.4 and found to be in the range of $0.57 - 0.87 \text{ J g}^{-1} \text{ K}^{-1}$ and $0.80 - 1.05 \text{ J g}^{-1} \text{ K}^{-1}$ for SrApCl-10w20AlBSG and AlBSG

respectively at the temperature range $T = 298 - 773$ K. The heat capacity of pristine AlBSG was found to be highest and SrApCl is found to be lowest, whereas C_p values of glass-bonded ceramic composites was intermediate between the two. This is usual; as C_p of ceramic is known to be lower because of lower the degrees of freedom of vibration, rotation & translation and as we proceed to waste loaded glass-bonded ceramic composites, degrees of freedom increases. Hence, increased in heat capacity values were observed. The enthalpy increment and heat capacity values were measured per gram of the sample as the exact formula weights of these above glass-ceramic composites were not known. The C_p values of the glass-bonded ceramic composites were compared with the C_p values measured by DSC method and found to be in good agreement within a difference of 2 - 5 %. The heat capacity values of the above glass and glass-bonded ceramic composites were studied for the first time by drop calorimetric technique at high temperatures upto 773 K.

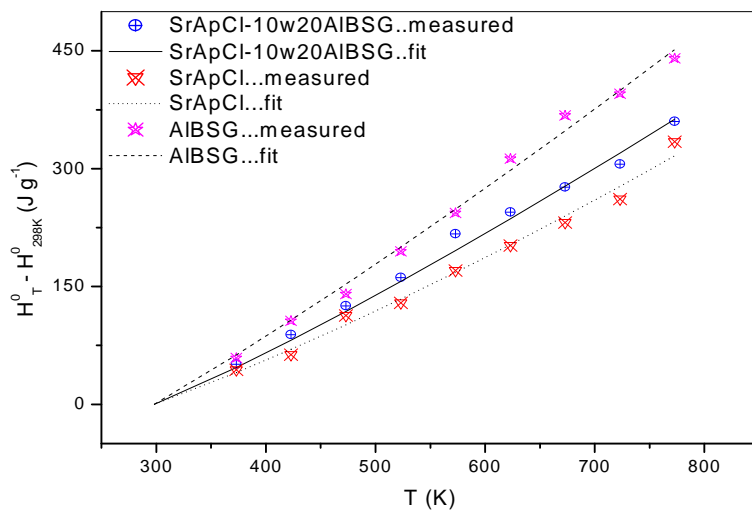


Fig. 4.9: Enthalpy increments measurements of SrApCl, SrApCl-10w20AlBSG, AlBSG

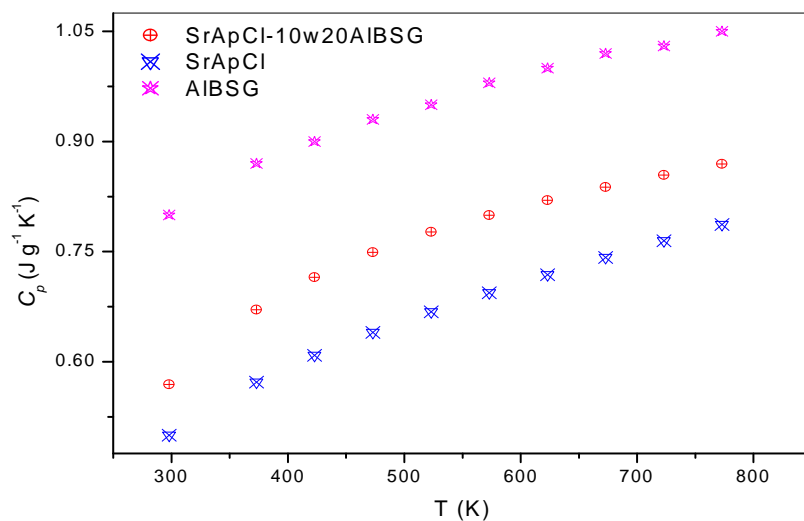


Fig. 4.10: Heat capacity measurements of SrApCl, SrApCl-10w20AlBSG and AlBSG by drop calorimetry

Table 4.3: Enthalpy increments and heat capacity data for SrApCl-10w20AlBSG

T (K)	$H_T^0 - H_{298K}^0$ Measured (J g ⁻¹)	Fit (J g ⁻¹)	Difference (%)	$C_{p,T}$ (J g ⁻¹ K ⁻¹)	C_p (DSC method) [29] (J g ⁻¹ K ⁻¹)
298	-	0	-	0.57	0.57
373	50.88	46.85	7.92	0.67	0.65
423	88.77	81.56	8.13	0.71	0.68
473	125.33	118.19	5.69	0.75	0.71
523	161.39	156.36	3.12	0.78	0.74
573	216.81	195.78	9.69	0.80	0.76
623	244.71	236.28	3.44	0.82	0.78
673	276.50	277.73	-0.44	0.83	0.80
723	305.61	320.04	-4.72	0.85	0.82
773	359.99	363.14	-0.87	0.87	0.84

Table 4.4: Enthalpy increments and heat capacity data for AlBSG

T (K)	$H_T^0 - H_{298K}^0$ Measured (J g ⁻¹)	Fit (J g ⁻¹)	Residuals (%)	$C_{p,T}$ (J g ⁻¹ K ⁻¹)
298	--	0	--	0.80
373	58.96	62.82	-6.55	0.87
423	106.33	107.18	-0.80	0.90
473	140.47	153.06	-8.96	0.93
523	194.64	200.23	-2.88	0.95
573	243.76	248.56	-1.97	0.98
623	312.75	297.92	4.74	1.00
673	367.65	348.26	5.27	1.02
723	395.36	399.53	-1.05	1.03
773	440.37	451.68	-2.57	1.05

Table 4.5: Coefficients of fit equations, $H_T^0 - H_{298K}^0 = a + bT + cT^2 + d/T$

Glass-ceramics composites	a	b	c	d
SrApCl	-201.91±0.15	0.50±0.00	1.96E-4±1.99E-7	10481.20±23.65
SrApCl-10w20AlBSG	-303.61±0.08	0.75±0.00	1.01E-4±8.19E-6	21329.66±23.24
AlBSG	-304.56±0.09	0.85±0.00	1.46E-4±1.28E-7	11788.78±19.11

4.3.6 Electrical conductivity by DC measurement

The electrical conductivity of pure aluminoborosilicate glass (AlBSG), pure Sr-chloroapatite and glass-bonded ceramic composite were studied by DC measurements. The electrical conductivity was found in the range of $4.99 \times 10^{-9} - 1.09 \times 10^{-3} \text{ S cm}^{-1}$ at the temperature range 537-1113 K. The Arrhenius plots of $\log(\sigma T)$ vs. $1000/T$ were shown in the Fig. 4.11.

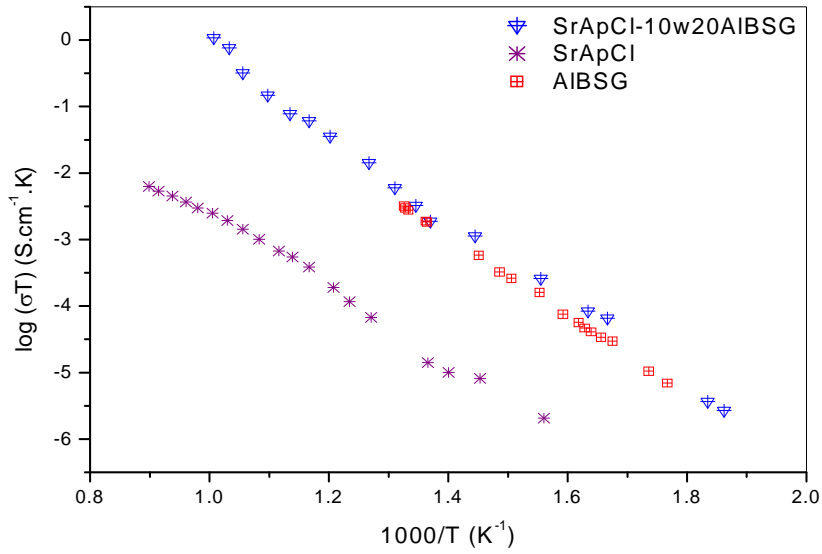


Fig. 4.11: Comparison of Electrical conductivity of SrApCl, SrApCl-10w20AlBSG and pristine AlBSG

It was found that SrApCl was having the lowest conductivity, whereas AlBSG and SrApCl-10w20AlBSG were having similar electrical conductivity. This suggests that as glass was added to strontium chloroapatite, conductivity increased due to the increase in concentration of Na^+ in the glass phase [28, 29]. The activation energies of these glass and glass-bonded composites were also calculated from the slope of $\log(\sigma T)$ vs. $1000/T$ Arrhenius plot and were found to be 1.11 eV, 1.19 eV and 1.26 eV for pure SrApCl, pristine AlBSG and SrApCl-10w20AlBSG respectively, which also suggests the ionic type of conduction prevails in these glass-bonded composites. However, ionic conductivity exhibited by SrApCl is not due to Na^+ ; confirmation on the exact conducting species responsible for electrical conduction in SrApCl needs further investigations.

References

1. P. Trocellier, Immobilization of radionuclides in single phase crystalline waste forms: a review on their intrinsic properties and long term behavior, *Ann. Chim. Sci. Mater.* 25 (2000) 321–337.
2. M. E. Fleet, Y. Pan, Site Preference of Nd in Fluoroapatite $[\text{Ca}_{10}(\text{PO}_4)_6\text{F}_2]$, *J. Solid State Chem.* 112 (1994) 78–81.
3. E. R. Vance, J. Davis, K. Olufson, I. Chironi, I. Karatchevtseva, I. Farnan, Candidate waste forms for immobilisation of waste chloride salt from pyroprocessing of spent nuclear fuel, *J. Nucl. Mater.* 420 (2012) 396–404.
4. G. Leturcq, A. Grandjean, D. Rigaud, P. Perouty, M. Charlot, Immobilization of fission products arising from pyrometallurgical reprocessing in chloride media, *J. Nucl. Mater.* 347 (2005) 1–11.
5. F. Audubert, J. Carpena, J. L. Lacout, F. Tetard, Elaboration of an iodine-bearing apatite Iodine diffusion into a $\text{Pb}_3(\text{VO}_4)_2$ matrix, *Solid State Ionics*, 95 (1997) 113–119.
6. A. Chartier, C. Meis, J. D. Gale, Computational study of Cs immobilization in the apatites $\text{Ca}_{10}(\text{PO}_4)_6\text{F}_2$, $\text{Ca}_4\text{La}_6(\text{SiO}_4)_6\text{F}_2$ and $\text{Ca}_2\text{La}_8(\text{SiO}_4)_2\text{O}_2$, *Phys. Rev. B* 64 (2001) 085110.
7. Eric H. Oelkers, Jean- Marc Montel, Phosphates and Nuclear Waste Storage, *Elements* 4 (2008) 113–116.
8. M. Wei, J. H. Evans, T. Bostrom, L. Grondhal, Synthesis and characterization of hydroxyapatite, fluoride-substituted hydroxyapatite and fluoroapatite, *J. Mater. Sci. Mater. Med.* 14 (2003) 311–320.

9. H. Jena, R. V. Krishnan, R. Asuvathraman, K. Nagarajan, K. V. G. Kutty, Thermal expansion and heat capacity measurements on $\text{Ba}_{10-x}\text{Cs}_x(\text{PO}_4)_6\text{Cl}_{2-2x}$, ($x = 0 - 0.5$) chloroapatites synthesized by sonochemical process, *J. Therm. Anal. Calorim.* 106 (2011) 875–879.
10. R. V. Krishnan, H. Jena, K. V. G. Kutty, K. Nagarajan, Heat capacity of $\text{Sr}_{10}(\text{PO}_4)_6\text{Cl}_2$ and $\text{Ca}_{10}(\text{PO}_4)_6\text{Cl}_2$ by DSC, *Thermochim. Acta.* 478 (2008) 13–16.
11. J. O. Nriagu, Lead orthophosphates-IV: formation and stability in the environment, *Geochim. Cosmochim. Acta.* 38 (1974) 887–898.
12. I. W. Donald, B. L. Metcalfe, S. K. Fong, L. A. Gerrard, D. M. Strachan, R. D. Scheele, A glass-encapsulated calcium phosphate waste form for the immobilization of actinide, fluoride-, and chloride-containing radioactive wastes from the pyrochemical reprocessing of plutonium metal, *J. Nucl. Mater.* 361 (2007) 78–93.
13. H. Jena, B. K. Maji, R. Asuvathraman, K. V. G. Kutty, Synthesis and thermal characterization of glass bonded Ca-chloroapatite matrices for pyrochemical chloride waste immobilization, *J. Non-Cryst. Solids*, 358 (2012) 1681–1686.
14. M. A. Lewis, S. Verma, J. P. Ackerman, Effect of different glasses in glass-bonded zeolite, Argonne National Laboratory, ANL/CMT/CP-84676, 1995.
15. I. W. Donald, B. L. Metcalfe, S. K. Fong, L. A. Gerrard, D. M. Strachan, R. D. Scheele, A glass-encapsulated calcium phosphate waste form for the immobilization of actinide-, fluoride-, and chloride containing radioactive wastes from the pyrochemical reprocessing of plutonium metal, *J. Nucl. Mater.* 361 (2007) 78-93.
16. J. M. Juoi, M. I. Ojovan, Characterization and durability of glass composite waste from immobilising spent clinoptilolite, WM'07 conference, Tucson, AZ, 2007.

17. K. Raj, K. K. Prasad, N. K. Bansal, Radioactive waste management practices in India, Nucl. Engg. Desig. 236 (2006) 914–930.
18. N. V. Ojovan, I. V. Startceva, A. S. Barinov, M. I. Ojovan, D. H. Bacon, B. P. McGrail, J. D. Vienna, Product consistency test of fully radioactive high-sodium content borosilicate glass K-26, Sym. Proc. Mat. Res. Soc. 824, 2004.
19. C. Y. Ho, R. E. Taylor (Eds.), Thermal Expansion of Solids, ASM International, Materials park, Ohio, USA, Chapter 1-2, 1998, pp. 1-131.
20. H. Czichos, T. Saito, E. Smith (Eds.), Thermal Expansion, Springer Handbook of Materials Measurement Methods, Chapter – 2, 2006, pp. 415.
21. K. V. G. Kutty, R. Asuvathraman, M. V. Krishnaiah, V. Ganesan, R. Parthasarathy, D. S. Subalakshmi, B. Suhasini, K. C. Srinivas, K. A. Gopal, P. V. Kumar, Design, fabrication and commissioning of a push rod dilatometer for thermal expansion studies on solids, IGC Report No. 283, 2006, pp. 23.
22. M. V. Krishnaiah, R. Asuvathraman, K. Joseph, B. Suhasini, K. V. Govindan Kutty, Drop calorimeter for the measurement of enthalpy increment of solids: design, fabrication and commissioning, IGC Report No. 319, 2013, pp.16.
23. M. V. Krishnaiah, Study of the thermophysical properties of some materials of interest in nuclear technology, PhD Thesis, University of Madras, 2000, pp. 96–104.
24. Binoy Kumar Maji, H. Jena, R. Asuvathraman, Electrical conductivity and glass transition temperature (T_g) measurements on some selected glass used for nuclear waste immobilization, J. Non-Cryst. Solids, 434 (2016) 102-107.
25. K. Sudarsanan, R. A. Young, Structure refinement and random error analysis for strontium chlorapatite, $\text{Sr}_5(\text{PO}_4)_3\text{Cl}$, Acta Crystallography B, 30 (1974) 1381-1385.

26. I. Avramov, T. S. Vassilev, I. Penkov, The glass transition temperature of silicate and borate glasses, *J. Non-Cryst Solids*, 351 (2005) 472–476.
27. B. K. Maji, H. Jena, R. V. Krishnan, R. Asuvathraman, K. Ananthasivan, K. V. G. Kutty, Comparison of thermal expansion and heat capacity properties of various borosilicate glass-bonded strontium chloroapatite composites loaded with simulated pyrochemical waste, *J. Therm. Anal. Calorim.* 119 [3] (2015) 1825-1831.
28. D. Ehrt, R. Keding, Electrical conductivity and viscosity of borosilicate glasses and melts, *Phys. Chem. Glasses: Eur. J. Glass Sci. Technol. B*, 50(3) (2009) 165-171.
29. A. Grandjean, M. Malki, C. Simonnet, Effect of composition on ionic transport in $\text{SiO}_2\text{-B}_2\text{O}_3\text{-Na}_2\text{O}$ glasses, *J. Non-Cryst. Solids*, 32 (2006) 2731- 2736.

Synthesis, characterization and thermophysical property measurements on barium borosilicate glass (BaBSG)-bonded Sr-chloroapatite composites loaded with simulated pyrochemical chloride waste

5.1 Introduction

In the previous chapters, studies were carried out on glass-bonded composites of Sr-chloroapatite with borosilicate glass (BSG) and alumino borosilicate glass (AlBSG) [1-8]. Barium borosilicate glass (BaBSG) was used for the immobilization of sulphate bearing HLW [9]. Thus BaBSG and its glass-bonded Sr-chloroapatite composites were taken into consideration to explore their suitability over BSG or AlBSG glass bonded analogues with respect to chemical durability, heat capacity and thermal expansion properties *etc.* This chapter describes the synthesis, characterization and thermo-physical properties measurement on pristine BaBSG and its waste loaded glass-bonded composite with strontium chloroapatite (SrApCl-10w20BaBSG). XRD studies showed the formation of crystalline phase of Sr-chloroapatite. High temperature XRD (HTXRD) was carried out to investigate the occurrence or non-occurrence of in situ phase changes during heating. HTXRD also unravels the lattice expansion along *a*- and *c*-axis of the crystalline phase present in the composite matrices. The percentage linear thermal expansion and glass transition temperatures (T_g) were measured by dilatometry. Heat capacity (C_p) and T_g of the composites were also measured by differential scanning calorimetry (DSC) in the temperature range of 300 – 560 K. T_g measured by thermomechanical (TMA) or dilatometry is compared with the T_g measured by DSC technique. C_p values of these glass bonded composites were also measured by drop calorimetry upto 773 K and compared with that of DSC measurement. The results on thermal expansion, C_p and T_g on these composites are reported for the first time.

5.2 Experimental

5.2.1 Synthesis and characterization of barium borosilicate glass (BaBSG) and BaBSG-bonded Sr-chloroapatite composite (SrApCl-10w20BaBSG)

Barium borosilicate glass (abbreviated as BaBSG) was also prepared by mixing glass forming reagents (SiO_2 {38.61 wt. % or 47.35 mol %} + B_2O_3 {25.32 wt. % or 26.8 mol %} + Na_2O {12.02 wt% or 14.29 mol %} + BaO {24.05 wt. % or 11.56 mol %}) [9], the mixture was homogenized by grinding in a mortar-pestle for half-an-hour and then calcined at 673 K in an alumina crucible for 1½ h. The calcined mixture was then melted at 1473 K / 2h in the same alumina crucible and quenched to room temperature. The products were then characterized by powder-XRD to confirm the absence of any crystalline phases present in the final products.

Strontium chloroapatite ($\text{Sr}_{10}(\text{PO}_4)_6\text{Cl}_2$, abbreviated as SrApCl) and its barium borosilicate glass-bonded composites with 10 wt. % simulated chloride waste were prepared by mixing apatite (SrApCl): pyrochemical waste (W): glass (BaBSG) in the mass ratio of 70:10:20 respectively. Instead of directly using SrApCl for the preparation of composites, the stoichiometric concentrations of apatite-forming reagents such as SrCO_3 , $\text{NH}_4\text{H}_2\text{PO}_4$ and NH_4Cl were used for the preparation of SrApCl. Then 10 wt. % of simulated chloride waste ($\text{LiCl}/31.92$, $\text{KCl}/39.01$, $\text{NaCl}/11.23$, $\text{CsCl}/1.74$, $\text{BaCl}_2/1.38$, $\text{CeCl}_3/2.63$, $\text{NdCl}_3/12.08$ in wt. %) was mixed with 20 wt. % of glass-forming reagents. All the reagents were mixed together and ground thoroughly, and the mixture was heated at 773 K / 5 h and subsequently heated at 1023 K for 5 h in air. The products were characterized by powder XRD.

5.2.2 Leaching studies by soxhlet measurement

Comprehensive leaching studies were carried out on the composites under soxhlet condition at 363 K for 28 days. The details of this method were also described in chapter-2. The analysis of the leachate solutions were done by AAS for alkali and alkaline earth elements; ICP-OES for rare earth elements and ion selective electrode for Cl.

The elemental composition of the leachate was obtained from the chemical analysis. By using the chemical analysis result, normalised leach rate (NLR, $\text{g cm}^{-2}\text{d}^{-1}$) for each element (Cl, Li, Na, K, Cs, Sr, Ba, Nd, Ce *etc.*) was calculated as follows [10]

$$\text{NLR} = \frac{A_i \times V}{f_i \times S \times t} \quad (5.1)$$

Where, A_i = concentration of the i^{th} species in the leachate solution ($\mu\text{g/ml}$), V = volume of distilled water taken for analysis (ml), f_i = mol fraction of i^{th} element / species, S = surface area (cm^2) and t = time (d). The literature values for the standard glasses were in the order of $10^{-6} \text{ g cm}^{-2} \text{ d}^{-1}$ [9].

5.2.3 Thermal expansion measurements on the glass bonded composites by high temperature X-ray diffraction (HTXRD)

The % linear axial expansion of the powders was measured by using Philips X'pert-Pro MPD model XRD machine with high temperature attachment. The details were described in chapter-3. The XRD patterns of the samples were recorded at room temperature (RT) and then the temperature of the sample was increased to 373 K, 473 K, 573 K and 673 K by programmed heating and cooling with a heating / cooling rate of 5 K min^{-1} . XRD pattern of the sample was recorded at preset temperatures. The lattice constants of the samples were calculated by using X'pert Plus software package supplied by Philips. The % linear expansion along a -axis and c -axis was measured by using the following formula [11, 12].

$$\% \text{ expansion along } a - \text{axis} = \frac{a_{673} - a_{RT}}{a_{RT}} \times 100 \quad (5.2)$$

$$\text{Similarly; } \% \text{ expansion along } c - \text{axis} = \frac{c_{673} - c_{RT}}{c_{RT}} \times 100 \quad (5.3)$$

The mean or average coefficient of thermal expansion (CTE = α_m) was calculated by using the following formula

$$\text{Along } a - \text{axis; CTE} = \frac{a_{673} - a_{RT}}{a_{RT}} \times \frac{1}{\Delta T} \quad (5.4)$$

$$\text{along } c - \text{axis; CTE} = \frac{c_{673} - c_{RT}}{c_{RT}} \times \frac{1}{\Delta T} \quad (5.5)$$

5.2.4 Thermal expansion by thermomechanical measurement (Dilatometry)

The glass-bonded ceramic powders of SrApCl-10w20BaBSG and SrApCl were fabricated to 10 mm dia and 10 mm length pellets. These pellets were heat-treated at 1023 K for 10 h in air. These annealed pellets were taken for thermal expansion measurement by a home-built dilatometer [13]. The detailed description was given in chapter-3. The percentage (%) linear expansions for SrApCl, SrApCl-10w20BaBSG and pristine BaBSG were measured in the temperature range below the glass transition temperature of the glass phase. The % linear thermal expansion was calculated by using the following formula [14, 15] shown in Eq. 5.6.

$$\text{Percentage linear thermal expansion} = \% \text{ LTE} = \left(\frac{\Delta L}{L} \right) \times 100 \quad (5.6)$$

The average coefficient of thermal expansion (CTE, α_m) of the compounds was calculated by using the formula shown in Eq. 5.7,

$$\text{Average CTE} = \alpha_m = \left(\frac{\Delta L}{L} \right) \times \left(\frac{1}{\Delta T} \right) \quad (5.7)$$

Where, ΔL = change in length, L = the length of the pellet at room temperature and ΔT = change in absolute temperature (K). The instantaneous coefficient of thermal expansion (α_i) was also measured by using the formula given in Eq. 5.8:

$$\alpha_i = \left(\frac{1}{L_0} \right) \times \left(\frac{dL}{dT} \right) = \left(\frac{1}{L_0} \right) \times \left(\frac{L_{i+1} - L_1}{T_{i+1} - T_1} \right) \quad (5.8)$$

Where, L_0 = length of the pellet at room temperature, L_{i+1} = length of the sample when temperature of the sample is T_{i+1} , and L_1 & T_1 = length and temperature of the sample respectively at beginning of the measurement just above the room temperature.

5.2.5 Glass transition temperature (T_g) and heat capacity (C_p) measurements by DSC

The measurements on glass transition temperatures and heat capacity were carried out using differential scanning calorimeter (DSC) (Model No.: DSC821e/700 of M/s. Mettler Toledo GmbH, Switzerland). The details of the procedure were described in chapter-3.

5.2.6 Enthalpy increments and C_p measurement by Drop Calorimetry

Enthalpy increments of these glass-bonded composites were measured by using a home built drop calorimeter at the temperature range of 373 – 773 K as described in Chapter-3 [16, 17]. These enthalpy increment data were then fitted in a 4-term polynomial equation ($H_T^0 - H_{298K}^0 = a + bT + cT^2 + d/T$) using the two constraints i) $(H_T^0 - H_{298K}^0)_{298} = 0$ and (ii) $\left(\frac{d}{dT} (H_T^0 - H_{298K}^0) \right)_{298} = (C_p)_{298}$. The heat capacity, C_p was derived from the enthalpy increment data by differentiating the fitted enthalpy increment equation as given by, $C_p = b + 2cT - d/T^2$. C_p values obtained from DSC measurement were then compared with the computed C_p values of drop calorimetric techniques. The C_p values found to be similar within the difference of 2-5%.

5.2.7 Electrical conductivity by DC measurement

The electrical conductivity measurements of the prepared glass (BaBSG) and its glass-bonded composite (SrApCl-10w20BaBSG) were carried out by DC measurement techniques. The cylindrical pellets of BaBSG were prepared by melting the synthesized glasses at 1173 K and then the melt was transferred or poured into a graphite crucible (10 mm dia and 12 mm height) to fabricate pellets of required dimension. The graphite crucible was cut, opened to remove the glass pellets. These pellets (8 mm dia and 6 mm length) were annealed at 773 K in a platinum crucible for 15 h in air. Whereas, in case of measurements of electrical conductivity of glass-bonded glass ceramic composites, the pellets (10 mm dia and 2 mm height) were fabricated and subsequently heated to 1073 K for 10 h in air ambience. The detailed description of this procedure was given in chapter-3. The conductivity of samples was calculated using the formula as given in Eq. 5.9 [18].

$$\sigma = \frac{L}{A} \times \frac{1}{R} \quad (5.9)$$

Where, σ is the conductivity (S cm^{-1}), R is the resistance (ohms), A and L is the cross sectional area (cm^2) and length or thickness (cm) of the pellet respectively.

5.3 Results and Discussions

5.3.1 Characterization by XRD

The powder-XRD pattern of pure BaBSG is shown in Fig. 5.1. The XRD patterns confirmed the formation of glasses as the appearance of a characteristic broad hump / peak at lower 2θ -angle and absence of any crystalline peaks corresponding to respective glass forming reagents / oxide constituents (SiO_2 , B_2O_3 , Na_2O and BaO) of BaBSG. The formation of broad peak at lower 2θ -values is attributed to the short range periodicity and amorphous nature of the solid.

Figure 5.1 shows the formation of Sr-chloroapatite crystalline single phase by XRD for various glass-bonded/encapsulated composites. The presence of glass phase in the composites was not prominently seen in the XRD pattern. This may be attributed to the presence of comparatively small quantity of glassy phase compared to the crystalline phase. The broad hump expected in the XRD pattern for the glass phase might have been buried in the background. The lattice constants of the crystalline phase present in the composites were calculated by using X'pert Pro software which was confirmed by referring to the standard JCPDS pattern of strontium chloroapatite (PDF card No. # 70-1007) [19] and is given in Table 5.1. In all the cases, the SrApCl was indexed to a hexagonal crystal system. The lattice constants do show slight variation along *a*- and *c*-axis. This may be attributed to the substitution of smaller or bigger ions into the Sr-sublattice of SrApCl crystalline phase.

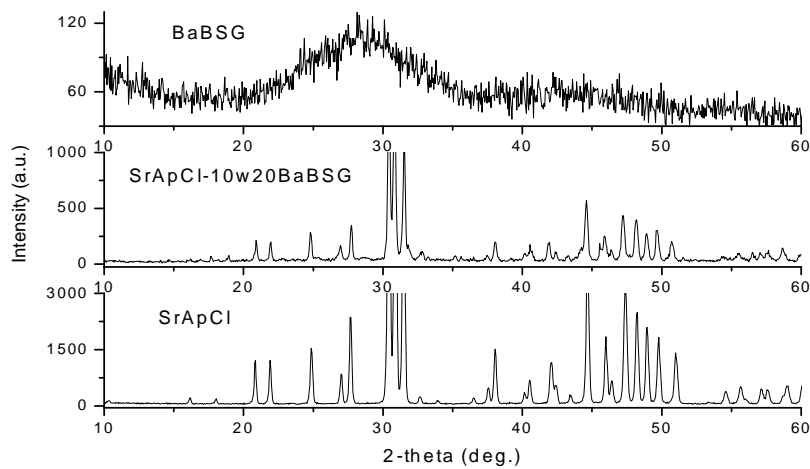


Fig. 5.1: XRD patterns of SrApCl, SrApCl-10w20BaBSG and BaBSG at room temperatures

Table 5.1: Lattice constants of SrApCl and SrApCl-10w20BaBSG recorded at room temperature, Crystal system: Hexagonal; SG = P6₃/m

Composites nominal composition	Lattice constants of crystalline phase in the composite (sample powders heat-treated at 1023 K, XRD recorded at room temperature)
SrApCl	$a = 9.858(2)$, $c = 7.177(2)\text{\AA}$, $\alpha = 90^\circ$, $\gamma = 120^\circ$, $V/10^6 = 604.02\text{ pm}^3$
SrApCl-10w20BaBSG	$a = 9.852(2)$, $c = 7.198(3)\text{\AA}$, $\alpha = 90^\circ$, $\gamma = 120^\circ$, $V/10^6 = 605.11\text{ pm}^3$

5.3.2 Leaching studies by soxhlet method

The leaching studies were done by using Soxhlet method and the concentration of elements in the leachate were measured by various analytical methods like AAS for alkali and alkaline earth elements, ICP-OES for rare earth elements and ion chromatography for chloride etc. Then normalised leach rates of various species were calculated with time and was given in Fig. 5.2. The normalised leach rate was observed to be in the order of 10^{-2} to $10^{-4}\text{ g cm}^{-2}\text{ d}^{-1}$.

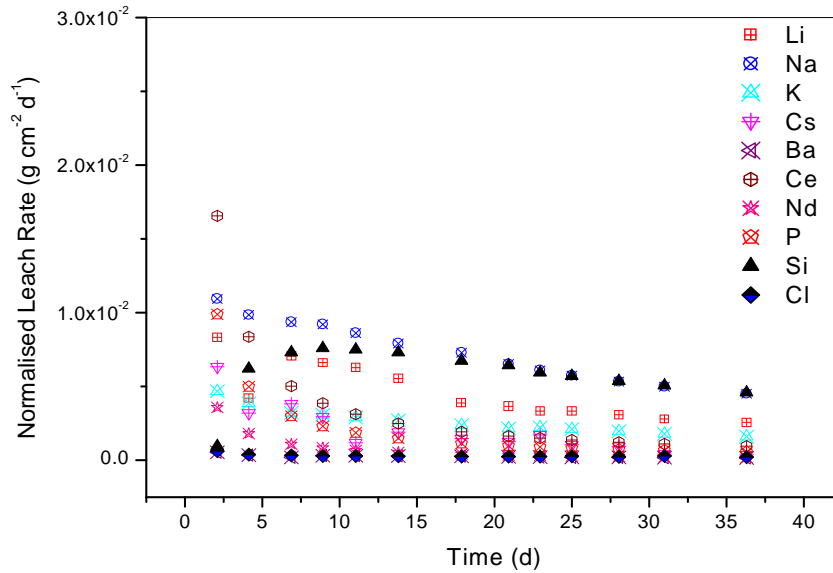


Fig. 5.2: Normalised leach rate with time for SrApCl-10w20BaBSG

5.3.3 Thermal expansion by HTXRD

Fig. 5.3 shows the High Temperature XRD (HTXRD) patterns recorded at various temperatures (298 - 673 K) for SrApCl-10w20BaBSG. The lattice constants were calculated from the XRD patterns recorded at elevated temperatures by using X'Pert pro package. The lattice constants were found to increase on increasing temperature. Structural transition was not observed for the crystalline phase on heating the sample from 298 to 673 K in air. All the measurements were carried out below glass transition temperature of the composites. However, glass transition (T_g) of the composites were observed above 673 K. The material did not react with the Pt-strip used as sample holder and heating element within the temperature range of measurement.

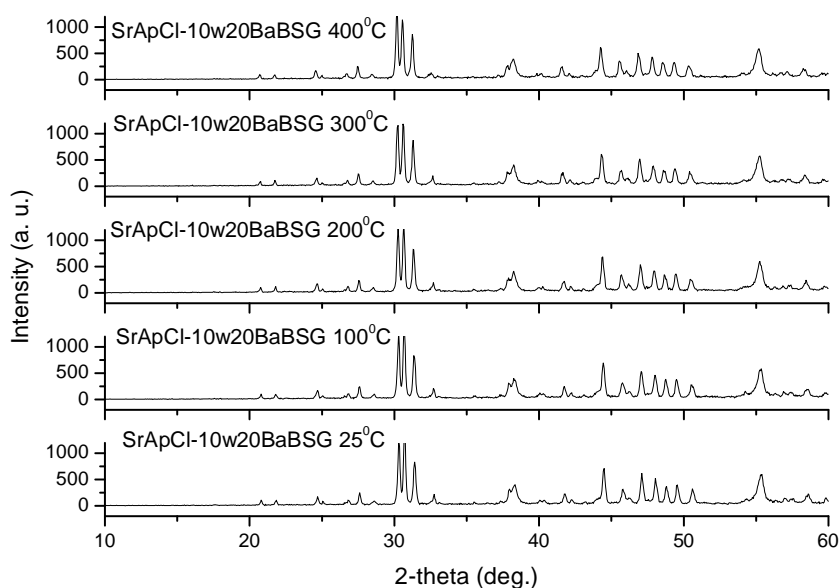


Fig. 5.3: HTXRD patterns of SrApCl-10w20BaBSG at various temperatures

Fig. 5.4 shows the variation of lattice constant along a -axis of the unit cell at the temperature range $T = 298 - 673$ K. Lattice constants increase with the increase in

temperature. This may be attributed to the positive thermal expansion of a -axis with the temperature effect. These lattice constants along the a -axis was fitted to a second order equation and fitting values found to be a (Å) = $9.85 + 3.56E^{-5} T + 8.94E^{-8} T^2$ having $R^2 = 0.996$. The coefficient of thermal expansion along the a -axis was found to be $12.70(2) \times 10^{-6} K^{-1}$ at the temperature range 298 - 673 K.

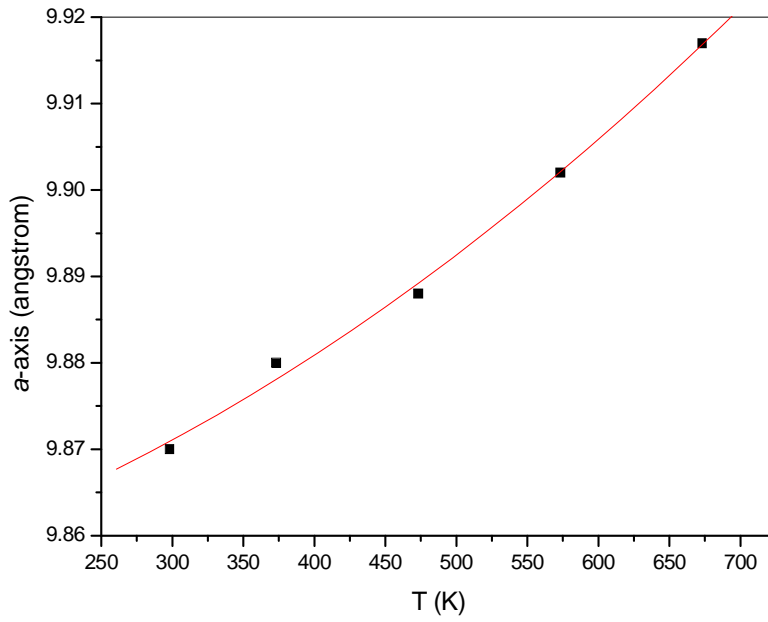


Fig. 5.4: Lattice parameter (a -axis) expansion with T (K) by HTXRD

Similarly, the c -parameter was also measured and is shown in Fig. 5.5. The c -axis of SrApCl-10w20BaBSG also shows positive thermal expansion with the temperature effect. These values also fitted to a second order polynomial and the fitted equation was found to be c (Å) = $7.196 + 3.15E^{-5} T + 6.53E^{-8} T^2$ having correlation of determination, $R^2 = 0.992$. The coefficient of thermal expansion along the c -axis was found to be $13.68(2) \times 10^{-6} K^{-1}$ at the temperature range 298 – 673 K.

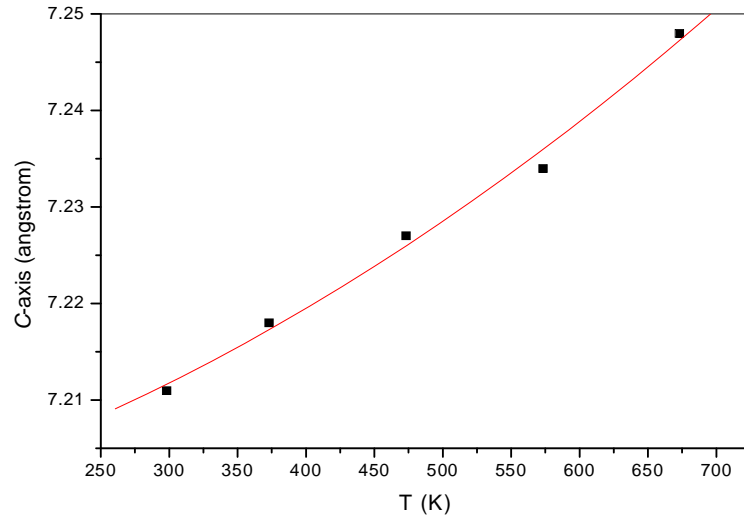


Fig. 5.5: Lattice parameter (*c*-axis) expansion with T (K) by HTXRD

Volume expansion of the unit cell of SrApCl-10w20AlBSG was also calculated by using the hexagonal unit cell volume and given in Fig. 5.6. Expansion of unit cell were fitted to a second order polynomial and found to be $V / \text{\AA}^3 = 605.21 + 0.01 T + 1.59\text{E}^{-5} T^2$ having $R^2 = 0.981$.

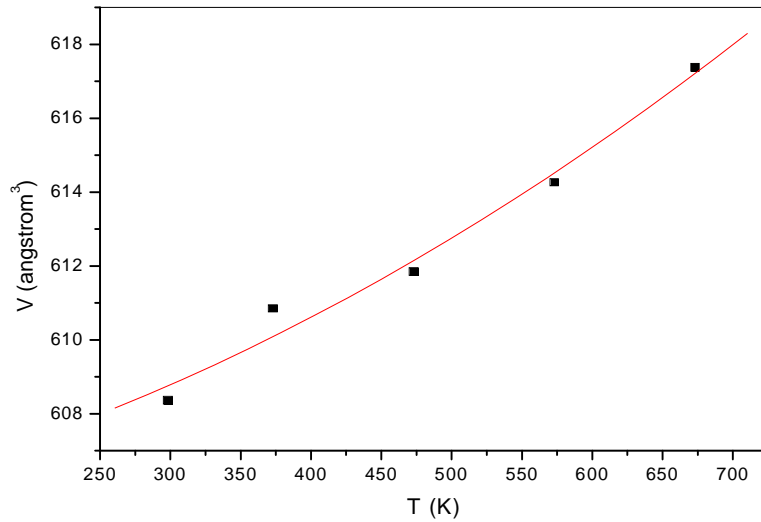


Fig. 5.6: Lattice cell volume expansion with T (K) by HTXRD

5.3.4 Thermal expansion and T_g measurement by dilatometry

The % linear thermal expansion of the pure SrApCl, pristine BaBSG glass, and glass-bonded composites is shown in Fig. 5.7. The % thermal expansion for SrApCl-10w20BaBSG is found to be highest compared to pure glass and ceramic materials. Glass shows the lowest thermal expansion compared to the crystalline ceramic materials. However, the glass-bonded ceramic composites show higher thermal expansion. This may be attributed to the formation of non-bridging oxygen in glass. The coefficients of thermal expansion of these composites were also calculated and found to be $12.91 \pm 0.25 \times 10^{-6}$, $16.2 \pm 0.32 \times 10^{-6}$ and $11.84 \pm 0.23 \times 10^{-6} \text{ K}^{-1}$ for SrApCl, SrApCl-10w20BaBSG and BaBSG respectively. The glass transition temperature of these composites were also measured from dilatometry experiment and found to be $673 \pm 5 \text{ K}$ for SrApCl-10w20BaBSG and $781 \pm 5 \text{ K}$ for BaBSG as shown in Fig. 5.8 and in Table 5.2 (the values shown are the T_g -onset) [20]. The decrease in T_g for composites indicate weakening of glass network in waste loaded glass-bonded ceramic composites compared to the pristine glass.

5.3.5 Glass transition temperature (T_g) by DSC

The DSC scans of the samples are shown in Fig. 5.8. The figure shows that the glass transition temperatures (T_g) of SrApCl-10w20BaBSG and BaBSG are 685 ± 4 and $785 \pm 4 \text{ K}$ respectively (Table 5.2). The T_g values of the composites are found to decrease in comparison to parent glass composition used for encapsulating the SrApCl ceramic along with pyrochemical waste. The decrease in T_g may be attributed to the interaction of waste elements with glass network formers and modifiers. The T_g values obtained from DSC measurement were also compared with the value obtained from dilatometric measurement and found to be in good agreement with slight variation in T_g values. The heat capacity of the

glass-bonded ceramic composite was measured in the temperature range of 298 – 560 K (below glass transition temperatures). The C_p of SrApCl-10w20BaBSG as a function of temperature is given in Table 5.3. The standard deviation between measurements is in the range of 1-2%.

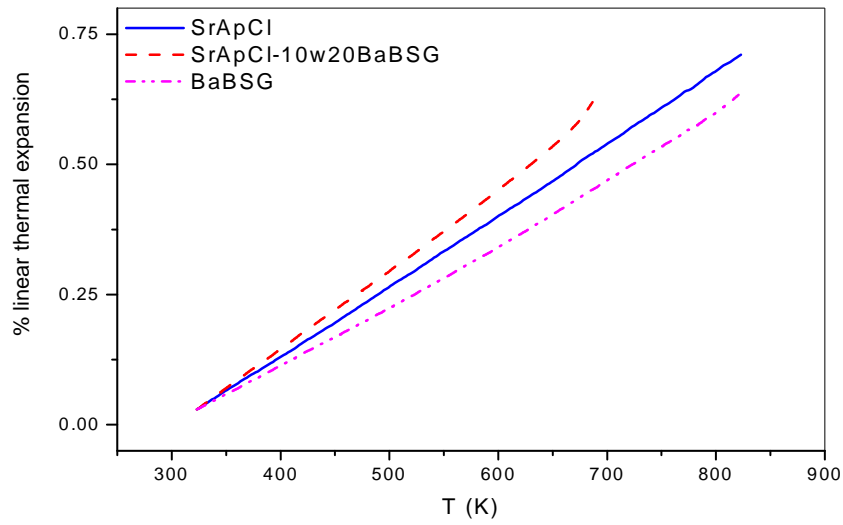


Fig. 5.7: Percentage linear thermal expansion of SrApCl, SrApCl-10w20BaBSG and BaBSG with T (K)

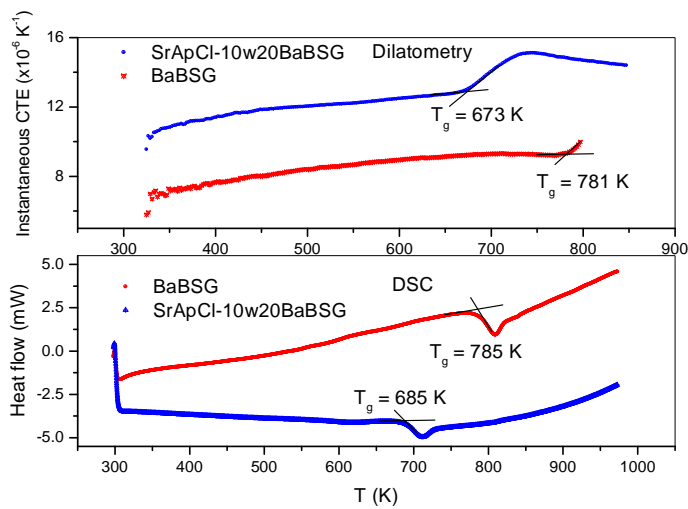


Fig. 5.8: Glass transition temperatures (T_g) for BaBSG and SrApCl-10w20BaBSG by DSC and dilatometry

Table 5.2: comparison of T_g values by DSC and dilatometric method for BaBSG and SrApCl-10w20BaBSG

Glass Compositions	T_g by DSC measurement (K)	T_g by Dilatometry measurement (K)	Literature values (K)
BaBSG	785 \pm 4	781 \pm 5	769
SrApCl-10w20BaBSG	685 \pm 4	673 \pm 5	--

5.3.6 Enthalpy increment and heat capacity (C_p) by Drop calorimetry

The enthalpy increment values of SrApCl (details described in chapter-3), SrApCl-10w20BaBSG and pure BaBSG were measured at the temperature range $T = 373-773$ K. The enthalpy increment of SrApCl-10w20BaBSG and BaBSG along with heat capacity values were given in Table 5.3 and 5.4 respectively. The % difference between the measured value and the fit values were observed to be upto $\pm 10\%$. These enthalpy increments were fitted to 4-term polynomial functions, $H_T^0 - H_{298K}^0 = a + bT + cT^2 + d/T$ using the constraints (i) $(H_T^0 - H_{298K}^0)_{298K} = 0$ and (ii) heat capacity of SrApCl, SrApCl-10w20BaBSG and BaBSG at 298K, $(C_p)_{298K}$. C_p at 298 K was calculated according to the Neumann-Kopp rule using the heat capacity values of Sr-apatite, whereas for glass and glass-bonded ceramic composites C_p at 298 K was measured in our earlier work by DSC method [21]. The coefficients of fitting equation for the enthalpy increments of waste loaded glass-ceramic composites were given in Table 5.5. The enthalpy increments of measured and fit values were plotted in Fig. 5.9. From the enthalpy increment plots, it was observed that there is a good agreement between the measured values and the fit values. The heat capacity of the composites were then computed at the temperature range $T = 298 - 773$ K by first derivative of the fitted enthalpy increment equation and were plotted in Fig. 5.10. The calculated heat capacity values were shown in Table 5.3 & 5.4 and found to be in the range of $0.54 - 0.85 \text{ J g}^{-1} \text{ K}^{-1}$ and $0.58 - 1.06 \text{ J g}^{-1} \text{ K}^{-1}$

for SrApCl-10w20BaBSG and pristine BaBSG respectively at the temperature range $T = 298 - 773$ K. Pure glass is having the higher heat capacity values compared to strontium chloroapatite. However, we found that glass-bonded ceramic composites are having the intermediate heat capacity values compared to pure crystalline and its pure glass. The reason may be ascribed to the interaction of glass phase with ceramic phase. The enthalpy increment and heat capacity values measured were expressed per gram of sample as the exact formula weights of these above glass-ceramic composites were not known. These C_p values of the glass-ceramic composites were compared with the C_p values measured by DSC method and found to be in good agreement within a difference upto 5 %. The heat capacity values of the above glass-ceramic composites were studied for the first time by drop calorimetric technique at high temperature upto 773 K.

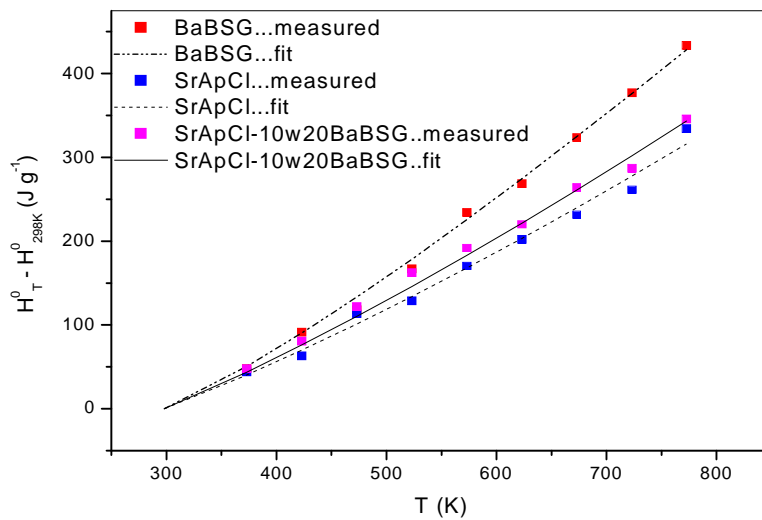


Fig. 5.9: Enthalpy increments measured and fit values of SrApCl, SrApCl-10w20BaBSG and BaBSG with T (K)

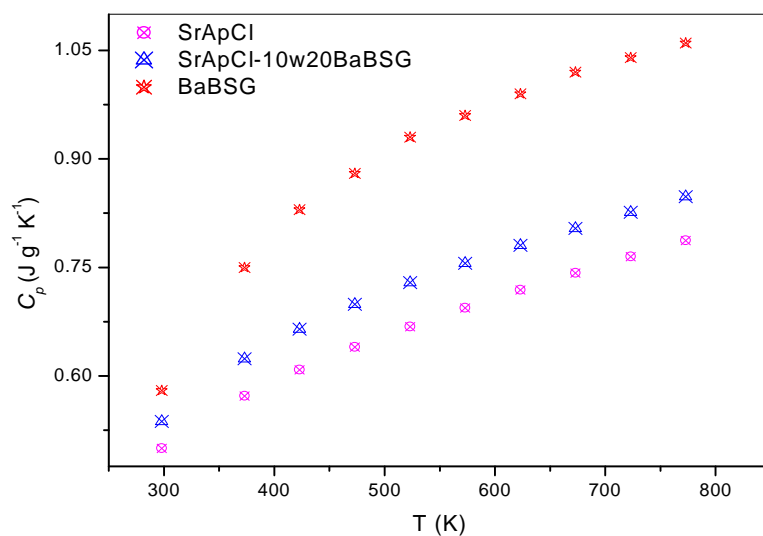


Fig. 5.10: Heat capacity of SrApCl, SrApCl-10w20BaBSG and BaBSG with T (K)

Table 5.3: Enthalpy increments and heat capacity data for SrApCl-10w-20BaBSG

T (K)	$H_T^0 - H_{298K}^0$ Measured (J g ⁻¹)	Fit (J g ⁻¹)	Difference (%)	$C_{p,T}$ (J g ⁻¹ K ⁻¹)	C_p (DSC method) [21] (J g ⁻¹ K ⁻¹)
298	-	0	-	0.54	0.54
373	47.51	43.79	7.84	0.62	0.61
423	80.561	76.03	5.62	0.66	0.65
473	122.00	110.16	9.70	0.70	0.68
523	162.47	145.87	10.21	0.73	0.71
573	191.78	183.00	4.58	0.76	0.73
623	220.07	221.42	-0.61	0.78	0.75
673	264.10	261.04	1.16	0.80	0.78
723	286.85	301.79	-5.20	0.83	0.80
773	345.68	343.64	0.58	0.85	0.82

Table 5.4: Enthalpy increments and heat capacity of BaBSG

T (K)	$H_T^0 - H_{298K}^0$ Measured (J g ⁻¹)	Fit (J g ⁻¹)	Residuals (%)	$C_{p,T}$ (J g ⁻¹ K ⁻¹)
298	--	0	--	0.58
373	48.13	50.70	-5.34	0.75
423	91.68	90.36	1.45	0.83
473	117.80	133.19	-13.06	0.88
523	166.79	178.45	-6.99	0.93
573	234.24	225.66	3.66	0.96
623	268.54	274.50	-2.22	0.99
673	323.27	324.74	0.45	1.02
723	376.96	376.20	0.20	1.04
773	433.70	428.77	1.14	1.06

Table 5.5: Coefficients of fit equations, $H_T^0 - H_{298K}^0 = a + bT + cT^2 + d/T$

Glass-ceramic composites	a	b	c	d
SrApCl	-201.91±0.15	0.50±0.00	1.96E-4±1.99E-7	10481.20±23.65
SrApCl-10w20BaBSG	-241.76±0.12	0.59±0.00	1.80E-4±1.11E-7	14541.19±16.29
BaBSG	-420.40±0.28	0.94±0.00	1.19E-4±2.23E-7	38461.82±29.19

5.3.7 Electrical conductivity by DC measurement

Electrical conductivity of pure SrApCl, pristine BaBSG and glass-bonded ceramic composite (SrApCl-10w20BaBSG) were measured by DC technique. The electrical conductivity were found to be in the range of $3.23 \times 10^{-9} - 8.44 \times 10^{-3} \text{ S cm}^{-1}$ at the temperature range $T = 640 - 983 \text{ K}$. These electrical conductivity values are plotted in Fig. 5.11. It was observed that SrApCl is having the lowest electrical conductivity values;

whereas, BaBSG and SrApCl-10w20BaBSG shows almost similar conductivity trend. The enhance conductivity in case of BaBSG and BABSG bonded composite is due to the contribution of Na^+ ions present in the glass phase of the composite and glass [22-24]. Whereas, the SrApCl does not have Na^+ ion, therefore its conductivity is relatively lower. The activation energies of these glass and glass-bonded composites were also computed from the slope of $\log(\sigma T)$ vs. $1000/T$ plot and found to be 1.11 eV, 1.19 eV and 1.41 eV for SrApCl, BaBSG and SrApCl-10w20BaBSG respectively.

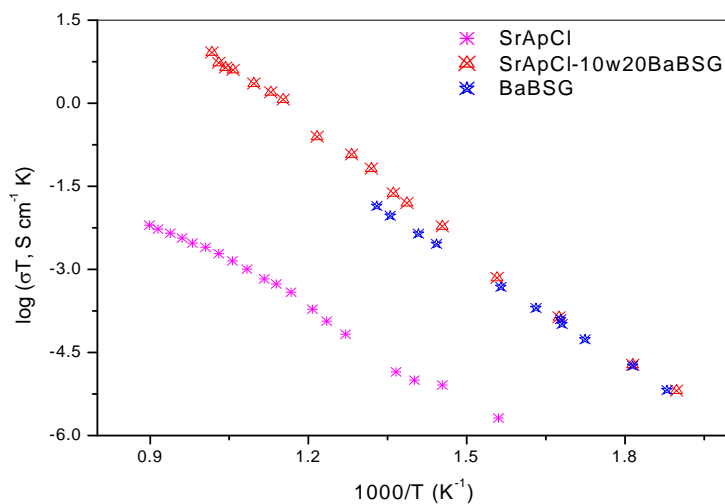


Fig. 5.11: Electrical conductivity of SrApCl, SrApCl-10w20BaBSG and BaBSG

References:

1. G. Leturcq, A. Grandjean, D. Rigaud, P. Perouty, M. Charlot, Immobilization of fission products arising from pyrometallurgical reprocessing in chloride media, J. Nucl. Mater. 347 (2005) 1-11.

2. E. R. Vance, J. Davis, K. Olufson, I. Chironi, I. Karatchevtseva, I. Farnan, Candidate waste forms for immobilisation of waste chloride salt from pyroprocessing of spent nuclear fuel, *J. Nucl. Mater.* 420 (2012) 396–404.
3. H. Jena, B. K. Maji, R. Asuvathraman, K. V. G. Kutty, Synthesis and thermal characterization of glass bonded Ca-chloroapatite matrices for pyrochemical chloride waste immobilization, *J. Non-Cryst. Solids*, 358 (2012) 1681–1686.
4. P. Trocellier, Immobilization of radionuclides in single phase crystalline waste forms: a review on their intrinsic properties and long term behavior, *Ann. Chim. Sci. Mater.* 25 (2000) 321–337.
5. I. W. Donald, B. L. Metcalfe, S. K. Fong, L. A. Gerrard, D. M. Strachan, R. D. Scheele, A glass-encapsulated calcium phosphate waste form for the immobilization of actinide-, fluoride-, and chloride containing radioactive wastes from the pyrochemical reprocessing of plutonium metal, *J. Nucl. Mater.* 361 (2007) 78–93.
6. M. Wei, J. H. Evans, T. Bostrom, L. Grondhal, Synthesis and characterization of hydroxyapatite, fluoride-substituted hydroxyapatite and fluoroapatite, *J. Mater. Sci. Mater. Med.* 14 (2003) 311–320.
7. M. A. Lewis, S. Verma, J. P. Ackerman, Effect of different glasses in glass-bonded zeolite, Argonne National Laboratory, ANL/CMT/CP-84676, 1995.
8. J. O. Nriagu, Lead orthophosphates-IV: formation and stability in the environment, *Geochim. Cosmochim. Acta*, 38 (1974) 887–898.
9. C. P. Kaushik, R. K. Mishra, P. Sengupta, A. Kumar, D. Das, G. B. Kole, K. Raj, Barium borosilicate glass—a potential matrix for immobilization of sulphate bearing high-level radioactive waste, *J. Nucl. Mater.* 358 (2006) 129–138.

10. M. A. Lewis, S. Verma, J. P. Ackerman, Effect of different glasses in glass-bonded zeolite, Argonne National Laboratory, ANL/CMT/CP-84676, 1995.
11. E. F. Kaelble, MgO thermal expansion, In: E. F. Kaelble (editor), Handbook of X-rays, Chapter -13, New York, Mc-Graw Hill, 1967, pp. 15.
12. J. Belle, R. M. Berman, Thermal expansion chapter, In: J. Belle, R. M. Berman (editors), Thorium dioxide: preparation and nuclear applications, DOE/NE-0060, US Department of Energy, Washington D. C, Govt. printing office, USA, 1984, pp. 169.
13. K. V. G. Kutty, R. Asuvathraman, M. V. Krishnaiah, V. Ganesan, R. Parthasarathy, D. S. Subalakshmi, B. Suhasini, K. C. Srinivas, K. A. Gopal, P. V. Kumar, Design, fabrication and commissioning of a push rod dilatometer for thermal expansion studies on solids, IGC report no. 283, 2006.
14. C. Y. Ho, R. E. Taylor (editors), Thermal expansion of solids, ASM International: Materials Park, Chapter 1–2, 1998, pp. 1–131.
15. H. Czichos, T. Saito, E. Smith (editors), Thermal expansion, In: Springer handbook of materials measurement methods, Chapter-2, 2006, pp. 415.
16. M. V. Krishnaiah, R. Asuvathraman, K. Joseph, B. Suhasini, K. V. Govindan Kutty, Drop calorimeter for the measurement of enthalpy increment of solids: design, fabrication and commissioning, IGC Report No. 319, 2013, pp.16.
17. G. Grimvall, Thermophysical properties of materials, Revised Edition, North-Holland, Elsevier Science B. V., 1999.
18. B. K. Maji, H. Jena, R. Asuvathraman, K. V. G. Kutty, Electrical conductivity and thermal expansion behavior of MMoO_4 ($\text{M} = \text{Ca}, \text{Sr}$ and Ba), J. alloys compd. 640 (2015) 475-479.

19. K. Sudarsanan, R. A. Young, Structure refinement and random error analysis for strontium chloroapatite, $\text{Sr}_5(\text{PO}_4)_3\text{Cl}$, *Acta Cryst. B*, 30 (1974) 1381-1385.
20. I. Avramov, T. S. Vassilev, I. Penkov, The glass transition temperature of silicate and borate glasses, *J. Non-Cryst Solids*, 351 (2005) 472–476.
21. B. K. Maji, H. Jena, R. V. Krishnan, R. Asuvathraman, K. Ananthasivan, K. V. G. Kutty, Comparison of thermal expansion and heat capacity properties of various borosilicate glass-bonded strontium chloroapatite composites loaded with simulated pyrochemical waste, *J. Therm. Anal. Calorim.* 119 [3] (2015) 1825-1831.
22. D. Ehrt, R. Keding, Electrical conductivity and viscosity of borosilicate glasses and melts, *Phys. Chem. Glasses: Eur. J. Glass Sci. Technol. B*, 50(3) (2009) 165-171.
23. Binoy Kumar Maji, H. Jena, R. Asuvathraman, Electrical conductivity and glass transition temperature (T_g) measurements on some selected glass used for nuclear waste immobilization, *J. Non-Cryst. Solids*, 434 (2016) 102-107.
24. A. Grandjean, M. Malki, C. Simonnet, Effect of composition on ionic transport in SiO_2 - B_2O_3 - Na_2O glasses, *J. Non-Cryst. Solids*, 32 (2006) 2731- 2736.

Synthesis, characterization and thermophysical properties on lead borosilicate glass (PbBSG)-bonded Sr-chloroapatite composites with simulated pyrochemical chloride waste

6.1 Introduction

In the previous chapters, various modification of borosilicate glass has been adopted to see the efficiency of glass-bonded composites with Sr-chloroapatite [1-13]. Lead borosilicate glass (PbBSG) is one of such composition used in this study with chloroapatites [14]. The present chapter deals with the synthesis and characterization of pristine PbBSG and its glass-bonded ceramic composite with Strontium chloroapatite (SrApCl-10w20PbBSG). XRD characterization was used for the phase detection of glass-bonded composites. High Temperature XRD (HTXRD) was carried out to see whether in situ phase changes were occurring or not. HTXRD also reveals the lattice expansion of composite materials along *a*- and *c*-axis. The percentage linear thermal expansion and glass transition temperatures (T_g) were measured by dilatometry. Heat capacity (C_p) and T_g of the composites were also measured by differential scanning calorimetry (DSC) in the temperature range of 300–560 K. T_g measured by thermomechanical (TMA) or dilatometry is compared with the T_g measured by DSC technique. C_p values of these glass bonded composites were also measured by drop calorimetry at high temperature upto 773 K and compared with that of DSC data. The results on thermal expansion, C_p and T_g on these composites are discussed in this chapter.

6.2 Experimental

6.2.1 Synthesis and characterization of Sr-chloroapatite and its lead borosilicate glass-bonded composites

Lead borosilicate glass (abbreviated as PbBSG) was also prepared by mixing glass forming reagents (SiO_2 {37.5 wt. % or 50.99 mol %} + B_2O_3 {25.0 wt. % or 29.34 mol %} + Na_2O {6.25 wt% or 8.24 mol %} + PbO {31.25 wt. % or 11.43 mol %}) [14], the mixture was homogenized by grinding in a mortar-pestle for half-an-hour and then calcined at 673 K in an alumina crucible for 1½ h. The calcined mixture was heated to 1473 K / 2h in the same alumina crucible and air quenched to room temperature. The products were then characterized by powder-XRD to confirm the absence of any crystalline phases present in the final products.

Strontium chloroapatite ($\text{Sr}_{10}(\text{PO}_4)_6\text{Cl}_2$, abbreviated as SrApCl) and its lead borosilicate glass-bonded composites with 10 wt. % simulated chloride waste were prepared by mixing apatite (SrApCl): pyrochemical waste (W): glass (PbBSG) in the mass ratio of 70:10:20 respectively. Instead of directly using SrApCl for the preparation of composites, the stoichiometric concentrations of apatite-forming reagents such as SrCO_3 , $\text{NH}_4\text{H}_2\text{PO}_4$ and NH_4Cl were used for the preparation of SrApCl. Then 10 wt. % of simulated chloride waste ($\text{LiCl}/31.92$, $\text{KCl}/39.01$, $\text{NaCl}/11.23$, $\text{CsCl}/1.74$, $\text{BaCl}_2/1.38$, $\text{CeCl}_3/2.63$, $\text{NdCl}_3/12.08$ in wt. %) was mixed with 20 wt. % of glass-forming reagents. All the reagents were mixed together and ground thoroughly, and the mixture was heated at 773 K / 5 h and subsequently heated at 1023 K for 5 h in air. The products were characterized by powder XRD.

6.2.2 Fabrication of pellets of Sr-chloroapatite and its PbBSG glass-bonded composites

The powder samples of Sr-chloroapatite (SrApCl), Sr-chloroapatites + 10 wt. % simulated chloride waste + 20 wt. % PbBSG (SrApCl-10w20PbBSG) and PbBSG were fabricated into cylindrical pellets of 10 mm diameter and 10 mm height using tungsten

carbide die and plunger. The powder was pressed using 1-2 tons of loads in the die and plunger in a pellet press (Hydraulic pellet press, Ms. Kimaya Engineers, India). The pellets were heat-treated at 1123 K for 8 - 15 h in air on a platinum boat/crucible to improve the density of the pellets. The following compositions were thus fabricated (a) Sr-chloroapatite (SrApCl), b) SrApCl + 10 wt. % chloride waste + 20 wt. % PbBSG (SrApCl-10w20PbBSG) and pristine lead borosilicate glass (PbBSG). The theoretical density of the composites was calculated by using volume fraction procedure as describes in Chapter-3. The major phases considered for theoretical density calculation of the composites are lead borosilicate glass and apatite phase. The measured density of the pellets was nearly 80 - 83 % of the theoretical density. These glass bonded composites can achieve maximum 85 % of theoretical density under the preparation conditions followed in this work. This may be attributed to the inherent porous nature of the material.

6.2.3 Leaching studies on the simulated waste loaded samples

The leaching studies of SrApCl-10w20PbBSG were carried out at 363 K by soxhlet method as described in details at chapter-2. The leachate samples were collected upto 28 days and the leachate solutions were then analyzed by ISE (Ion Selective Electrode) for Cl⁻, AAS (Atomic Absorption Spectroscopy) and ICP-OES (Inductively Coupled Plasma - Optical Emission Spectroscopy) techniques were used to analyze alkali, alkaline earth and rare earth elements.

The normalised leach rate (NLR, g cm⁻² d⁻¹) was calculated from leachate concentrations of each element (Cl, Li, Na, K, Cs, Sr, Ba, Nd, Ce *etc.*) by using the following equation [15].

$$NLR = \frac{A_i \times V}{f_i \times S \times t} \quad (6.1)$$

Where, A_i = concentration of the i^{th} species in the leachate solution ($\mu\text{g/ml}$), V = volume of distilled water taken for analysis (ml), f_i = mol fraction of i^{th} element / species, S = surface area (cm^2) and t = time (d). The literature values of normalised leach rate are in the order of $\sim 10^{-6} \text{ g cm}^{-2} \text{ d}^{-1}$ for standard radwaste immobilization matrices [14].

6.2.4 Thermal expansion measurements by HTXRD

The % linear axial expansion of the powders was measured by using Philips X'pert-Pro MPD model with high temperature attachment. The details procedure was described in chapter-3. The XRD patterns of the samples were recorded at room temperature (RT) then the temperature of the sample was increased to 373 K, 473 K, 573 K and 673 K by programmed heating and cooling with a heating / cooling rate of 5 K min^{-1} . XRD pattern of the sample was recorded at preset temperatures. The lattice constants of the samples were calculated by using X'pert Plus software package supplied by Philips. The % linear expansion along a -axis and c -axis was measured by using the following formula [16, 17].

$$\% \text{ expansion along } a - \text{axis} = \frac{a_{673} - a_{RT}}{a_{RT}} \times 100 \quad (6.2)$$

$$\text{Similarly; \% expansion along } c - \text{axis} = \frac{c_{673} - c_{RT}}{c_{RT}} \times 100 \quad (6.3)$$

The mean or average coefficient of thermal expansion ($\text{CTE} = \alpha_m$) was calculated by using the following formula

$$\text{Along } a - \text{axis; CTE} = \frac{a_{673} - a_{RT}}{a_{RT}} \times \frac{1}{\Delta T} \quad (6.4)$$

$$\text{along } c - \text{axis; CTE} = \frac{c_{673} - c_{RT}}{c_{RT}} \times \frac{1}{\Delta T} \quad (6.5)$$

6.2.5 Thermal expansion and glass transition temperature (T_g) measurements by dilatometry

Thermal expansion and glass transition temperature measurements on pellets of 10 mm diameter and 10 mm height were carried out by dilatometry in the temperature range 323 - 800 K in air, by using a home-built apparatus [18]. The details of the procedure were described in chapter-3. The % linear expansion was calculated by using the following formula [16, 17].

$$\text{Percentage linear expansion} = \frac{\Delta L}{L_0} \times 100 \quad (6.6)$$

Where, ΔL = change in length, L_0 is the original length of the pellet at room temperature.

The coefficient of thermal expansion was calculated by using the formula

$$\text{CTE} = \alpha_m = \frac{\Delta L}{L_0} \times \frac{1}{\Delta T} \quad (6.7)$$

Where, ΔL = change in length = $L_{i+1} - L_1$, L_0 = length of the pellet at room temperature, ΔT = change in temperature in K = $T - T_i$, where T = highest temperature of each measurement.

The instantaneous coefficient of thermal expansion (α_i) was determined by using the following formula [17, 19].

$$\alpha_i = \frac{1}{L_0} \times \frac{dL}{dT} = \frac{1}{L_0} \times \frac{L_{i+1} - L_1}{T_{i+1} - T_1} \quad (6.8)$$

Where, L_0 = length of the sample at room temperature, L_{i+1} = length of the pellet when temperature of the sample is T_{i+1} , L_1 = length of the sample at temperature (T_1) when heating is started at the beginning of heating cycle of the experiment. The onset of the

instantaneous CTE vs. T (K) will give the glass transition of the corresponding glass-bonded Sr-chloroapatite composites.

6.2.6 Glass transition temperature (T_g) and heat capacity (C_p) measurement by DSC

The measurements on glass transition temperatures and heat capacity were carried out using differential scanning calorimeter (DSC) (Model No.: DSC821e/700 of M/s. Mettler Toledo GmbH, Switzerland) as described in chapter-3. The obtained T_g and C_p values were compared with the dilatometry and drop calorimetry measurements respectively.

6.2.7 Enthalpy increment and heat capacity measurement by Drop Calorimetry

Enthalpy increments of these glass-ceramic composites were measured by using a home built drop calorimeter [20, 21] at the temperature range of 373 – 773 K as described in chapter-3.

The enthalpy increment data were then fitted to an equation (Eqn. 6.9) of the form

$$H_T^0 - H_{298K}^0 = a + bT + cT^2 + d/T \quad (6.9)$$

, using the non-linear least square fitting program written in Matlab software. Two linear constraints (i) $(H_T^0 - H_{298K}^0)_{298} = 0$ and (ii) $(\frac{d}{dT}(H_T^0 - H_{298K}^0)_{298}) = (C_p)_{298}$ were imposed on the coefficients to get a meaningful fitting. The heat capacity, C_p was derived from the enthalpy increment data by differentiating the fitted equation (eqn. 6.9) as given in Eqn. 6.10.

$$C_p = b + 2cT - d/T^2 \quad (6.10)$$

The validation of the home-built drop calorimeter was done by measuring the enthalpy increments of standard MgO single crystal procured from Crystec, USA as also described in chapter-3.

6.2.8 Electrical conductivity measurements by DC technique

The electrical conductivity measurements of the prepared glass (BaBSG) and its glass-bonded composite (SrApCl-10w20BaBSG) were carried out by DC technique. The cylindrical pellets of BaBSG were prepared by melting the synthesized glasses at 1173 K and then the melt was transferred or poured into a graphite crucible (12 mm dia and 15 mm height) to fabricate pellets of required dimension. The graphite crucible was cut opened to remove the glass pellets. These pellets (10 mm diameter and 6 mm length) were annealed at 773 K in a platinum crucible for 15 h in air. The detailed description of this procedure was given in chapter-3. The conductivity of samples was calculated using the formula as given in Eq. 6.11 [22].

$$\sigma = \frac{L}{A} \times \frac{1}{R} \quad (6.11)$$

Where, σ is the conductivity (S cm^{-1}), R is the resistance (ohms), A & L are the cross sectional area (cm^2) and length or thickness of the pellet (cm) respectively.

6.3 Results and Discussions

6.3.1 Characterization by XRD

Fig. 6.1 shows the XRD-patterns of pure SrApCl, SrApCl-10w20PbBSG and pristine PbBSG. In SrApCl and SrApCl-10w20PbBSG XRD-patterns, it is found that Sr-chloroapatite is the only crystalline phase present among the glass-bonded composite; whereas, PbBSG XRD-pattern shows a broad hump at lower 2θ -value, which is the characteristic of glass phase. However, the broad peak due to glass phase is not observed in the XRD-pattern of glass-bonded composite. The broad hump due to glass phase (20 wt. %) is buried under the background because of the intense reflections from the crystalline phase (80 wt. %) as shown in Fig. 6.1.

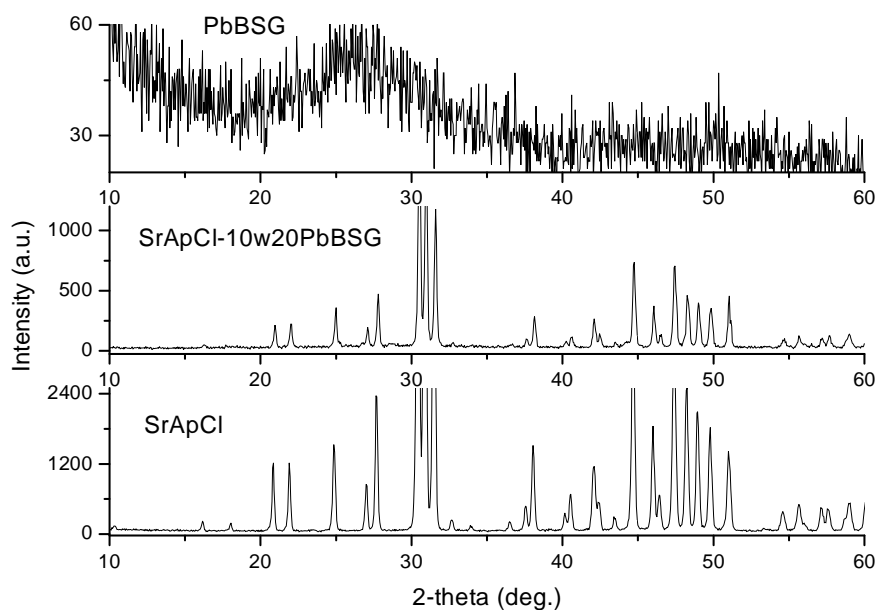


Fig. 6.1: Room temperature XRD patterns of SrApCl, SrApCl-10w20PbBSG and PbBSG

6.3.2 Leaching studies by soxhlet method

The leaching studies were carried out by using Soxhlet method and leachate concentration of various elements were measured by various analytical methods like AAS for alkali and alkaline earth elements, ICP-OES for rare earth elements and Ion chromatography for Chloride etc. Then normalised leach rates of various species were calculated with time and was given in Fig. 6.2. The normalised leach rate was observed to be in the order of 10^{-2} to $10^{-4} \text{ g cm}^{-2} \text{ d}^{-1}$.

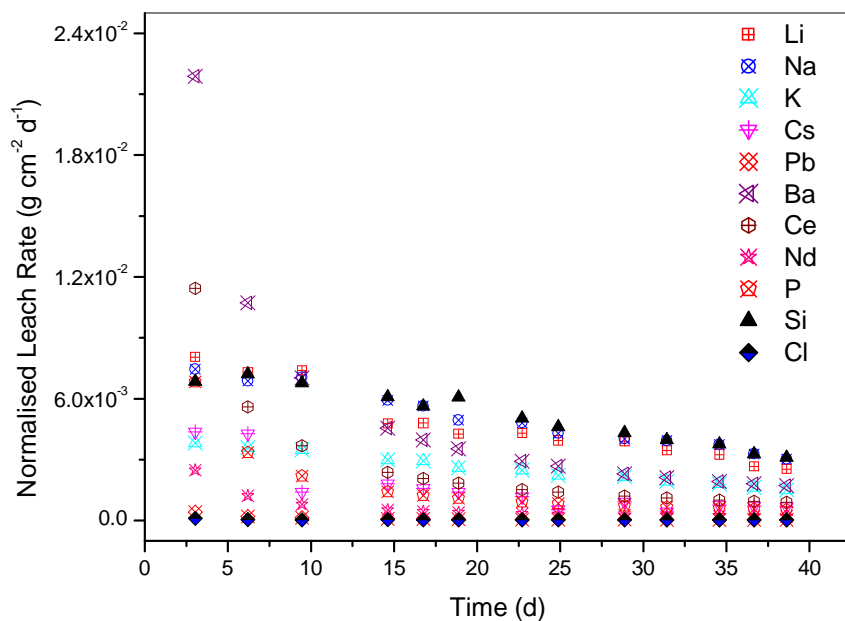


Fig. 6.2: Normalised leach rate with time for SrApCl-10w20PbBSG

6.3.3 Thermal expansion by HTXRD

Fig. 6.3 shows the High Temperature XRD (HTXRD) patterns recorded at various temperatures (298 - 673 K) for SrApCl-10w20PbBSG. The lattice constants were calculated from the XRD patterns at elevated temperatures. The lattice constants were found to increase on increasing temperature. In this method, no structural transitions were observed for the crystalline phase on heating the sample from 298 to 673 K in air. All the measurements were carried out below glass transition temperature of the composites. However, glass transition temperatures of the composites were observed above 673 K. The material did not react with the Pt-strip used as sample holder as well as heating element within the temperature range of measurement.

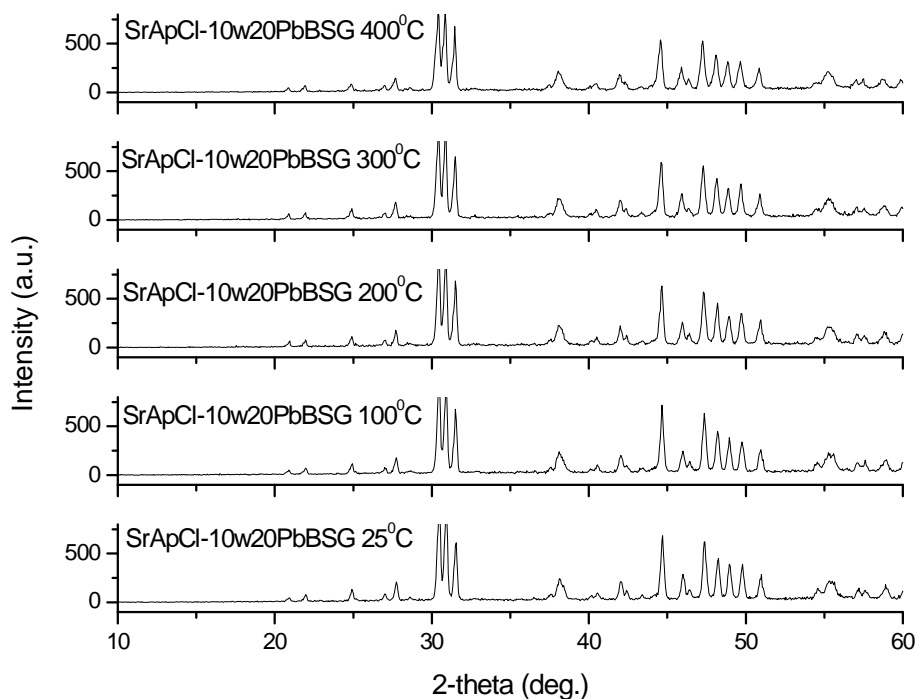


Fig. 6.3: HT-XRD patterns of SrApCl-10w20PbBSG with T (K)

Fig. 6.4 shows the variation of lattice constants along a -axis of the unit cell. From the lattice constant plot, it was observed that there is an increase in values along the a -axis with the temperature. This study suggested that the unit cell is expanding with increase in temperature. The a -axis values were fitted at various temperatures as shown in equation $y = a + bT + cT^2$. The fitting equation was found to be $a \text{ (Å)} = 9.82 + 4.79E^{-5} T + 2.02E^{-8} T^2$ having the R^2 value of 0.999. The lattice parameter expansion with various temperature is attributed to the substitution of smaller cations, $r^{\text{VIII}}(\text{Li}^+) = 0.9\text{Å}$, $r^{\text{VII}}(\text{Na}^+) = 1.12 \text{ Å}$, $r^{\text{IX}}(\text{Na}^+) = 1.24 \text{ Å}$, $r^{\text{VII}}(\text{Sr}^{2+}) = 1.21\text{Å}$, $r^{\text{IX}}(\text{Sr}^{2+}) = 1.31\text{Å}$ into the Sr-sublattice [23]. The coefficient of thermal expansion along the a -axis was found to be $16.78(2) \times 10^{-6} \text{ K}^{-1}$ at the temperature range 298 – 673 K.

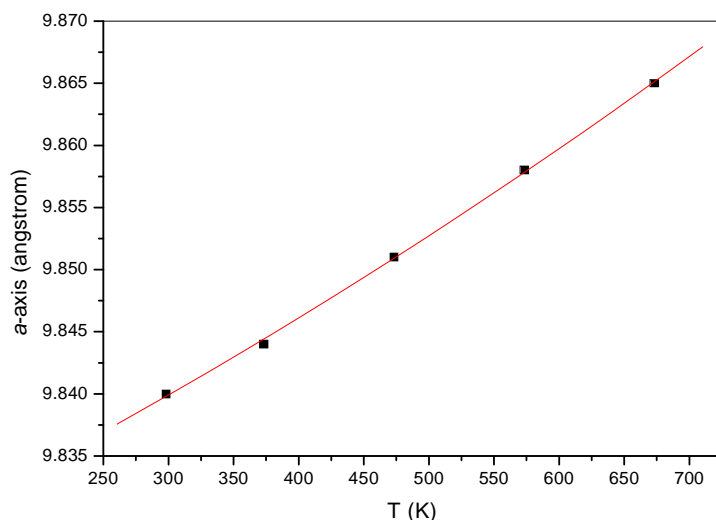


Fig. 6.4: Lattice parameter (*a*-axis) expansion with T (K) by HTXRD

Similarly, the *c*-parameter was also measured and is shown in Fig. 6.5. There is an increase in lattice constant (*c*-axis) along with various temperatures for the composition SrApCl-10w20PbBSG. The lattice parameter along the *c*-axis were also fitted to second order polynomial fit and the fitted equation was found to be $c \text{ (Å)} = 7.15 + 4.92\text{E}^{-5} T - 2.35\text{E}^{-8} T^2$ having coefficient of determination, $R^2 = 0.97$. The coefficient of thermal expansion along the *c*-axis was found to be $3.35(2) \times 10^{-6} \text{ K}^{-1}$ at the temperature range 298 – 673 K.

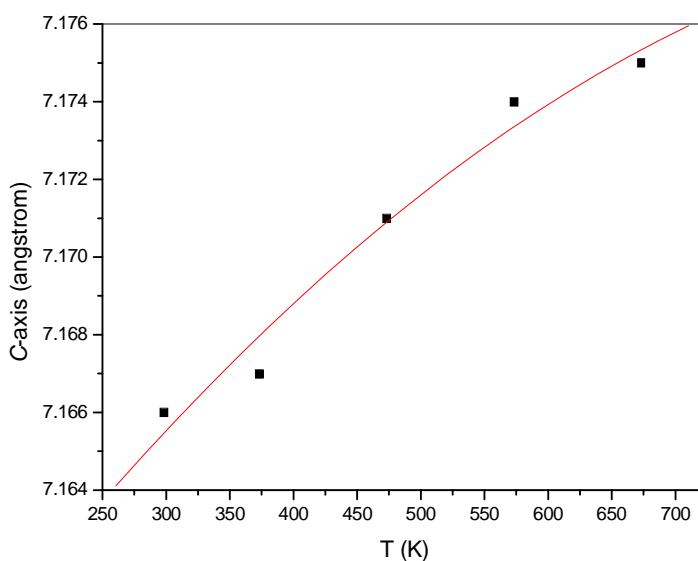


Fig. 6.5: Lattice parameter (*c*-axis) expansion with T (K) by HTXRD

Fig. 6.6 shows the variation of cell volume with temperature. Cell volume expanding with temperature in the range $T = 298 - 673$ K. These cell volume are fitted to a second order equation and fitting equation was found to be $V / \text{\AA}^3 = 598.09 + 0.01 T + 1.95E^{-6} T^2$ having $R^2 = 0.997$.

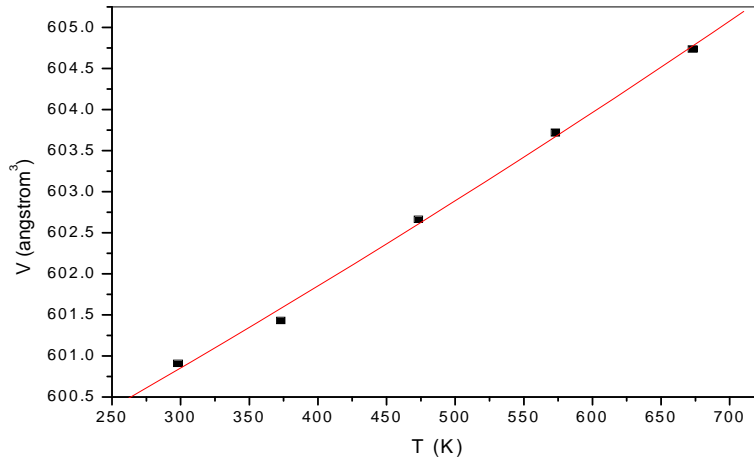


Fig. 6.6: Cell volume (V) expansion with T (K) by HTXRD

6.3.4 Thermal expansion and T_g measurement by Dilatometry

Percentage linear thermal expansion of SrApCl-10w20PbBSG was measured by dilatometry (thermo mechanical analysis) and the values were compared with that of pristine ceramic phase (SrApCl) as well as with pristine glass phase (PbBSG) as shown in Fig.6.7. Thermal expansion of pure lead borosilicate glass is found to be lower than that of pure ceramic SrApCl (Sr-chloroapatite). However, the thermal expansion of glass-bonded composites with simulated waste composition showed higher percentage thermal expansion compared to pure PbBSG and SrApCl. This can be well understood if we incorporate the effect of 10 wt% simulated waste in glass-bonded composite. With the addition of simulated chloride waste, the formation of non-stoichiometric Sr-chloroapatite in ceramic phase and

non-bridging oxygen in glass network increases. Hence, % thermal expansion of glass-bonded ceramic composite (SrApCl-10w20PbBSG) is higher than that of corresponding pristine ceramic and glass phases. Average thermal expansion coefficients of these glass-bonded composites were calculated from the dilatometric measurement and found to be $12.91 \times 10^{-6} \text{ K}^{-1}$ at $T = (323 - 845) \text{ K}$, $12.10 \times 10^{-6} \text{ K}^{-1}$ at $T = (323 - 735) \text{ K}$ and $16.40 \times 10^{-6} \text{ K}^{-1}$ at $T = (323 - 695) \text{ K}$ for SrApCl, PbBSG and SrApCl-10w20PbBSG respectively.

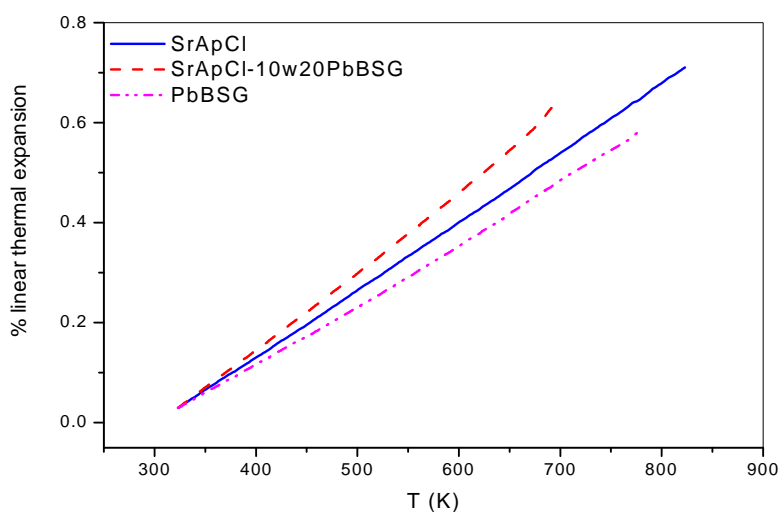


Fig. 6.7: Percentage linear thermal expansion of SrApCl, SrApCl-10w20PbBSG and PbBSG with T (K)

Glass transition temperatures of pure glass as well glass-bonded composites were measured by dilatometry and DSC measurement as shown in Fig. 6.8. T_g values were found to be $742 \pm 5 \text{ K}$ and $680 \pm 5 \text{ K}$ for PbBSG and SrApCl-10w20PbBSG respectively for dilatometry measurement; whereas by DSC measurement, T_g values were found to be $749 \pm 4 \text{ K}$ and 688 ± 5 for PbBSG and SrApCl-10w20PbBSG respectively as tabulated in Table 6.1. Trends found in glass transition temperature values also compliment the thermal expansion behavior of these glass-bonded ceramic composites, where lower thermal expansion

materials show higher glass transition temperatures and vice versa. There is a small difference between the T_g values measured by both the techniques. This may be attributed to the two different method of measurement or is due to two different heating rate applied in two techniques during the measurement (a heating rate of 2 K/min applied in dilatometry technique whereas, a heating rate of 10 K/min was applied for DSC measurement). T_g values of glass-bonded ceramic composites were reported for the first time.

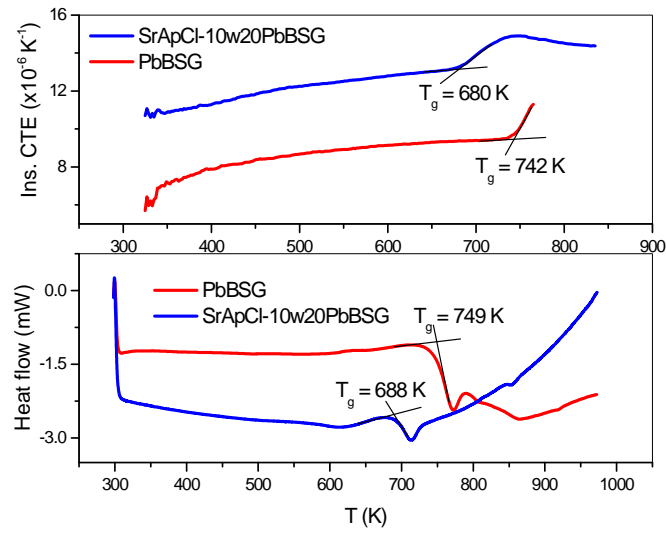


Fig. 6.8: Glass transition temperature measurements for SrApCl-10w20PbBSG and PbBSG by DSC as well as by dilatometry

Table 6.1: comparison of T_g values by DSC and dilatometric method for PbBSG and SrApCl-10w20PbBSG

Glass Compositions	T_g by DSC measurement (K)	T_g by Dilatometry measurement (K)	Literature values (K)
PbBSG	749 ± 4	742 ± 5	778
SrApCl-10w20PbBSG	688 ± 4	680 ± 5	--

6.3.5 Enthalpy increment and C_p by Drop calorimetry

The enthalpy increment values of SrApCl-10w20PbBSG and pristine PbBSG were measured at the temperature range $T = 373 - 773$ K and were given in Table 6.3 and 6.4 respectively. The enthalpy increments and heat capacity of SrApCl were explained in detail in chapter-3. The % difference between the measured value and the fit values were observed to be upto $\pm 10\%$. These enthalpy increments were fitted to 4-term polynomial functions, $H_T^0 - H_{298K}^0 = a + bT + cT^2 + d/T$ using the constraints (i) $(H_T^0 - H_{298K}^0)_{298K} = 0$ and (ii) heat capacity of SrApCl-10w20PbBSG and PbBSG at 298 K, $(C_p)_{298K}$. C_p at 298 K of pure glass and composite materials were measured by DSC method [24]. The coefficients of fitting equation for the enthalpy increments of waste loaded glass-ceramic composites were given in Table 6.2. The enthalpy increments of measured and fit values were plotted in Fig. 6.9. From the enthalpy increment plots, it was observed that there is a good agreement between the measured values and the fit values. The heat capacity of the composites were then computed at the temperature range $T = 298 - 773$ K by first derivative of the fitted enthalpy increment equation and were plotted in Fig. 6.10. The calculated heat capacity values were found to be in the range of $0.50 - 0.79 \text{ J g}^{-1} \text{ K}^{-1}$, $0.52 - 0.77 \text{ J g}^{-1} \text{ K}^{-1}$ and $0.57 - 0.93 \text{ J g}^{-1} \text{ K}^{-1}$ for SrApCl, SrApCl-10w20PbBSG and PbBSG respectively at the temperature range $T = 298 - 773$ K. These C_p values of the glass-bonded ceramic composites were compared with the C_p values measured by DSC method and found to be in good agreement within a difference of 2 - 5 %. Heat capacity of pure glass (BaBSG) is found to be higher than that of pure ceramic (SrApCl). Glass is an amorphous solid (supercooled liquid) and the atoms in the glass have higher vibrational & rotational; degrees of freedom than that of crystalline solids. In case of glass-bonded ceramic composites having 80 wt% of ceramic and 20 wt% of glass, C_p values

increase slightly, because of presence of Na^+ -ions in the glass component of the composite. The heat capacity values of the above glass-ceramic composites were studied first time by drop calorimetric technique at high temperatures upto 773 K.

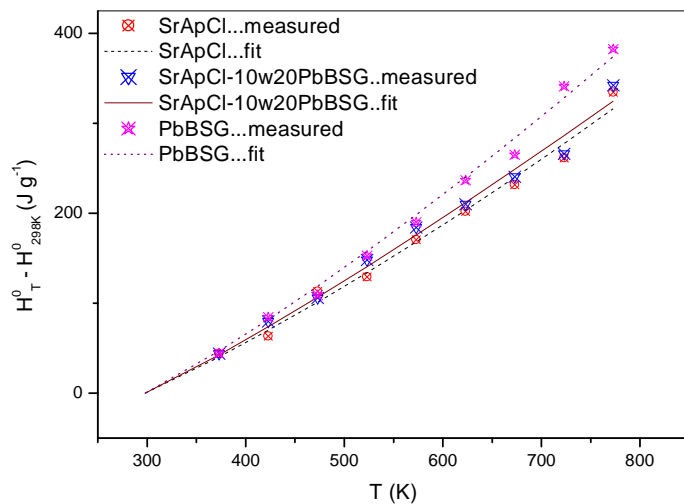


Fig. 6.9: Measured and Fit values of enthalpy increment with T (K) for SrApCl, SrApCl-10w20PbBSG and PbBSG

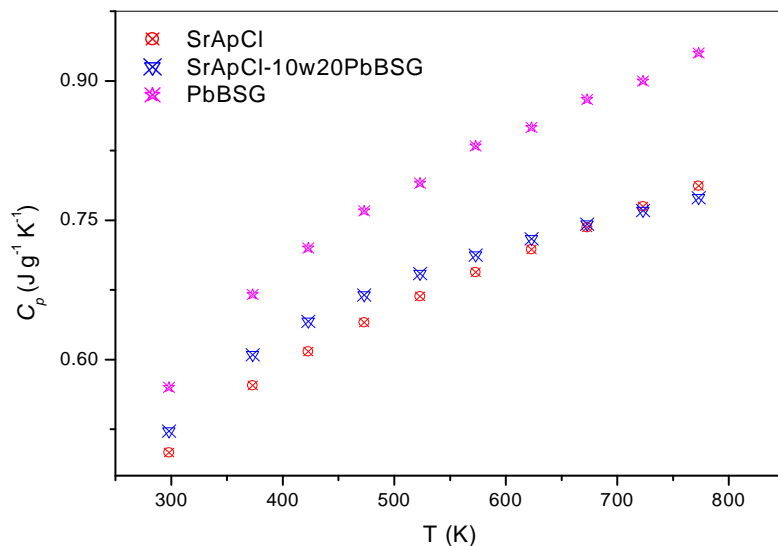


Fig. 6.10: Heat capacity measurement with T (K) for SrApCl, SrApCl-10w20PbBSG and PbBSG by drop calorimetry

Table 6.2: Coefficients of fit equations, $H_T^0 - H_{298K}^0 = a + bT + cT^2 + d/T$

Glass-ceramics composites	a	b	c	d
SrApCl	-201.91±0.15	0.50±0.00	1.96E-4±1.99E-7	10481.20±23.65
SrApCl-10w20PbBSG	-257.83±0.12	0.65±0.00	0.98E-4±1.11E-7	16474.97±24.12
PbBSG	-272.58±0.20	0.65±0.00	1.97E-4±2.04E-7	17914.35±15.19

Table 6.3: Enthalpy increments and heat capacity data for SrApCl-10w-20PbBSG

T	$H_T^0 - H_{298K}^0$		Difference	$C_{p,T}$	C_p (DSC method)
	Measured	Fit			[24]
(K)	(J g ⁻¹)	(J g ⁻¹)	(%)	(J g ⁻¹ K ⁻¹)	(J g ⁻¹ K ⁻¹)
298	-	0	-	0.52	0.52
373	43.78	42.60	2.71	0.60	0.60
423	79.79	73.79	7.51	0.64	0.63
473	105.8	106.58	-0.66	0.67	0.66
523	147.96	140.65	4.93	0.69	0.68
573	184.07	175.79	4.50	0.71	0.69
623	210.00	211.85	-0.88	0.73	0.71
673	240.64	248.75	-3.37	0.74	0.72
723	266.12	286.41	-7.62	0.76	0.74
773	342.22	324.78	5.09	0.77	0.75

Table 6.4: Enthalpy increments and heat capacity of PbBSG

T (K)	$H_T^0 - H_{298K}^0$ Measured (J g ⁻¹)	Fit (J g ⁻¹)	Residuals (%)	$C_{p,T}$ (J g ⁻¹ K ⁻¹)
298	--	0	--	0.57
373	44.08	46.90	-6.40	0.67
423	84.45	81.78	3.15	0.72
473	109.25	118.85	-8.79	0.76
523	152.76	157.76	-3.27	0.79
573	189.87	198.29	-4.43	0.83
623	236.56	240.28	-1.57	0.85
673	265.04	283.64	-7.02	0.88
723	341.01	328.27	3.73	0.90
773	382.43	374.13	2.17	0.93

6.3.6 Electrical conductivity by DC measurement

The electrical conductivity of pure aluminoborosilicate glass (PbBSG), pure Sr-chloroapatite and glass-bonded ceramic composite were studied by DC measurements. The electrical conductivity was found to be in the range of $4.99 \times 10^{-9} - 2.80 \times 10^{-3} \text{ S cm}^{-1}$ at the temperature range of 571 - 1113 K. The Arrhenius plots of $\log(\sigma T)$ vs. $1000/T$ were shown in the Fig. 6.11. It was found that SrApCl was having the lowest conductivity, whereas AlBSG and SrApCl-10w20PbBSG were having similar electrical conductivity. However, the conductivity of SrApCl-10w20PbBSG increases with the increase in temperature. This suggests that as glass is added to strontium chloroapatite, conductivity increase due to the ionic conductivity of Na^+ present in the glass network [25-27]. The activation energies for the above glass and glass-bonded composites were found to be 1.11 eV, 1.24 eV and 1.76 eV for SrApCl, PbBSG and SrApCl-10w20PbBSG respectively.

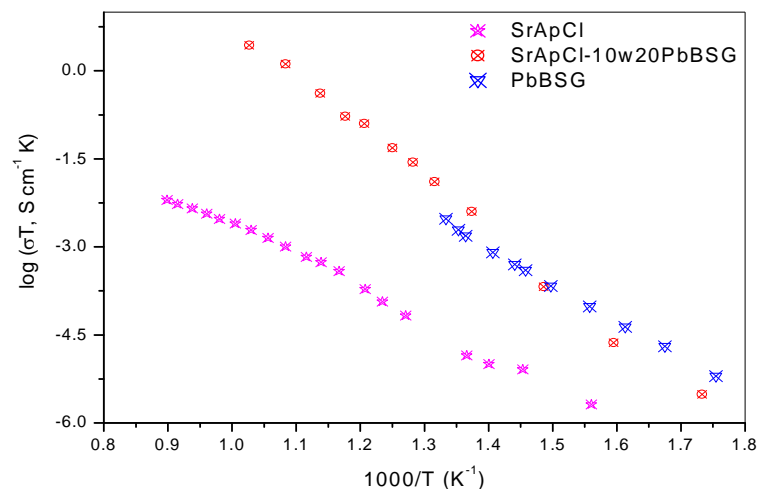


Fig. 6.11: Electrical conductivity measurements of SrApCl, SrApCl-10w20PbBSG and PbBSG

References:

1. M. Wei, J. H. Evans, T. Bostrom, L. Grondhal, Synthesis and characterization of hydroxyapatite, fluoride-substituted hydroxyapatite and fluoroapatite, J. Mater. Sci. Mater. Med. 14 (2003) 311–320.
2. T. J. White, D. Zhili, Structural derivation and crystal chemistry of apatites, Acta Crystallography B, 59 (2003) 1-16.
3. P. Trocellier, Immobilization of radionuclides in single phase crystalline waste forms: a review on their intrinsic properties and long term behavior, Ann. Chim. Sci. Mater. 25 (2000) 321–337.
4. H. Jena, B. K. Maji, R. Asuvathraman, K. V. G. Kutty, Synthesis and thermal characterization of glass bonded Ca-chloroapatite matrices for pyrochemical chloride waste immobilization, J. Non-Cryst. Solids, 358 (2012) 1681–1686.

5. J. O. Nriagu, Lead orthophosphates-IV: formation and stability in the environment, *Geochim. Cosmochim. Acta*, 38 (1974) 887–898.
6. I. W. Donald, B. L. Metcalfe, S. K. Fong, L. A. Gerrard, D. M. Strachan, R. D. Scheele, A glass-encapsulated calcium phosphate waste form for the immobilization of actinide, fluoride-, and chloride-containing radioactive wastes from the pyrochemical reprocessing of plutonium metal, *J. Nucl. Mater.* 361 (2007) 78–93.
7. S. Priebe, The ceramic waste form process at Idaho National Laboratory, International conference on incineration and thermal treatment technologies, INL/CON-07-12580, 2007.
8. C. Pereira, Production of sodalite waste forms by addition of glass, Argonne National Laboratory, ANL/CMT/CP-84675, 1995.
9. C. P. Kaushik, R. K. Mishra, P. Sengupta, A. Kumar, D. Das, G. B. Kole, K. Raj, Barium borosilicate glass—a potential matrix for immobilization of sulphate bearing high-level radioactive waste, *J. Nucl. Mater.* 358 (2006) 129–138.
10. M. A. Lewis, S. Verma, J. P. Ackerman, Effect of different glasses in glass-bonded zeolite, Argonne National Laboratory, ANL/CMT/CP-84676, 1995.
11. E. R. Vance, J. Davis, K. Olufson, I. Chironi, I. Karatchevtseva, I. Farnan, Candidate waste forms for immobilisation of waste chloride salt from pyroprocessing of spent nuclear fuel, *J. Nucl. Mater.* 420 (2012) 396–404.
12. F. Audubert, J. Carpena, J. L. Lacout, F. Tetard, Elaboration of an iodine-bearing apatite Iodine diffusion into a $\text{Pb}_3(\text{VO}_4)_2$ matrix, *Solid State Ionics*, 95 (1997) 113–119.
13. J. M. Juoi, M. I. Ojovan, Characterization and durability of glass composite waste from immobilising spent clinoptilolite, WM'07 conference, Tucson, AZ, 2007.

14. K. Raj, K. K. Prasad, N. K. Bansal, Radioactive waste management practices in India, Nucl. Engg. Desig. 236 (2006) 914–930.
15. M. A. Lewis, S. Verma, J. P. Ackerman, Effect of different glasses in glass-bonded zeolite, Argonne National Laboratory, ANL/CMT/CP-84676, 1995.
16. E. F. Kaelble, MgO thermal expansion, In: E. F. Kaelble (editor), Handbook of X-rays, Chapter -13, New York, Mc-Graw Hill, 1967, pp. 15.
17. J. Belle, R. M. Berman, Thermal expansion chapter, In: J. Belle, R. M. Berman (editors), Thorium dioxide: preparation and nuclear applications, DOE/NE-0060, US Department of Energy, Washington D. C, Govt. printing office, USA, 1984, pp. 169.
18. K. V. G. Kutty, R. Asuvathraman, M. V. Krishnaiah, V. Ganesan, R. Parthasarathy, D. S. Subalakshmi, B. Suhasini, K. C. Srinivas, K. A. Gopal, P. V. Kumar, Design, fabrication and commissioning of a push rod dilatometer for thermal expansion studies on solids, IGC report no. 283, 2006.
19. H. Czichos, T. Saito, E. Smith (Eds.), Thermal Expansion, Springer Handbook of Materials Measurement Methods, Chapter – 2, 2006, pp. 415.
20. M. V. Krishnaiah, R. Asuvathraman, K. Joseph, B. Suhasini, K. V. Govindan Kutty, Drop calorimeter for the measurement of enthalpy increment of solids: design, fabrication and commissioning, IGC Report No. 319, 2013, pp.16.
21. M. V. Krishnaiah, Study of the thermophysical properties of some materials of interest in nuclear technology, PhD Thesis, University of Madras, 2000, pp. 96–104.
22. B. K. Maji, H. Jena, R. Asuvathraman, K. V. G. Kutty, Electrical conductivity and thermal expansion behavior of MMoO_4 ($\text{M} = \text{Ca}, \text{Sr}$ and Ba), J. alloys compd. 640 (2015) 475–479.

23. R. D. Shannon, Revised effective ionic radii and systematic studies of interatomic distances in halides and chalcogenides, *Acta Crystallography A*, 32 (1976) 751-767.
24. B. K. Maji, H. Jena, R. V. Krishnan, R. Asuvathraman, K. Ananthasivan, K. V. G. Kutty, Comparison of thermal expansion and heat capacity properties of various borosilicate glass-bonded strontium chloroapatite composites loaded with simulated pyrochemical waste, *J. Therm. Anal. Calorim.* 119 [3] (2015) 1825-1831.
25. A. Grandjean, M. Malki, C. Simonnet, Effect of composition on ionic transport in $\text{SiO}_2\text{-B}_2\text{O}_3\text{-Na}_2\text{O}$ glasses, *J. Non-Cryst. Solids*, 32 (2006) 2731- 2736.
26. B. K. Maji, H. Jena, R. Asuvathraman, Electrical conductivity and glass transition temperature (T_g) measurements on some selected glass used for nuclear waste immobilization, *J. Non-Cryst. Solids*, 434 (2016) 102-107.
27. D. Ehrt, R. Keding, Electrical conductivity and viscosity of borosilicate glasses and melts, *Phys. Chem. Glasses: Eur. J. Glass Sci. Technol. B*, 50(3) (2009) 165-171.

Summary and Conclusions

The work reported in this thesis consists of synthesis of glass-bonded ceramic composites of Sr-chloroapatite loaded with simulated pyrochemical waste and their characterization by XRD and various techniques. Four different types of borosilicate glasses (borosilicate, alumina-borosilicate, barium-borosilicate and lead-borosilicate) were used to synthesize these waste loaded glass bonded composites and their thermo-physical properties were measured at elevated temperatures and compared.

The optimization of chloride waste loading was attempted into Sr-chloroapatite. Then the pyrochemical waste loaded chloroapatite was added with borosilicate glass to synthesize borosilicate glass-bonded Sr-chloroapatite. In this work, synthesis of SrApCl, SrApCl-10w, SrApCl-20BSG and 10 - 16 wt. % waste loaded glass-bonded ceramic composites (SrApCl-10w20BSG, SrApCl-13w20BSG and SrApCl-16w20BSG) were done by solid state reaction route using apatite forming reagents and glass forming reagents. The composites were characterized by XRD and various other techniques. Then thermophysical properties of these composites were measured at elevated temperatures and compared. As the waste loading increased from 10 to 16 wt. % into the glass-bonded ceramic composites, the thermal expansion, heat capacity (C_p) were found to increase. XRD studies showed the formation of crystalline phase of Sr-chloroapatite in all the composites except 16 wt. % waste loaded (SrApCl-16w20BSG) one. In this composite, phase separation of $\text{Sr}_3(\text{PO}_4)_2$ was observed along with the main crystalline phase of Sr-chloroapatite. Leaching studies revealed that leaching from the composite matrix increases with increased waste loading. SrApCl-

10w20BSG shows lowest normalised leach rate for the constituent elements among all the composites.

HTXRD studies confirmed the non-occurrence of in-situ interactions among the constituent elements in the matrix leading to the formation of other crystalline phases except Sr-chloroapatite solid solution. Percentage thermal expansion of the glass-bonded composites increases with the increase in waste loading. Glass transition temperature (T_g) of the composites decrease with increase in waste loading ($T_{g, SrApCl-10w20BSG} > T_{g, SrApCl-13w20BSG} > T_{g, SrApCl-16w20BSG}$). C_p values increased from pristine SrApCl to waste loaded composites, but it is lower than that of pristine borosilicate glass (BSG). The trend found to be in the order of C_p , $SrApCl < C_{p, SrApCl-10w} < C_{p, SrApCl-20BSG} < C_{p, SrApCl-10w20BSG} < C_{p, BSG}$.

The properties of borosilicate glass-bonded composite (SrApCl-10w20BSG) were compared with the properties of aluminium borosilicate (SrApCl-10w20AlBSG), barium borosilicate (SrApCl-10w20BaBSG) and lead borosilicate (SrApCl-10w20PbBSG) –bonded waste loaded composites. XRD studies reveal the formation of crystalline phase of Sr-chloroapatite in all the four glass-bonded composites. Leaching studies showed 10 wt. % waste loaded BSG-bonded composite (SrApCl-10w20BSG) has the lowest normalised leach rate for the simulated waste elements compared to that of SrApCl-10w20AlBSG, SrApCl-10w20BaBSG and SrApCl-10w20PbBSG.

HTXRD shows the non-occurrence of structural transitions on heating of these composite materials from 298 to 673 K in air ambience, which suggests the thermal stability of the crystalline phase in presence of the decay heat released from the waste elements. Percentage thermal expansion of SrApCl-10w20AlBSG was found to be lowest compared to SrApCl-10w20BSG; whereas SrApCl-10w20BaBSG and SrApCl-10w20PbBSG show

thermal expansion of the same order of magnitude, but higher than that of SrApCl-10w20AlBSG and SrApCl-10w20BSG as shown in Fig. 7.1. The thermal expansion coefficients were found to show similar trend as described above (SrApCl-10w20BSG: $15.1 \times 10^{-6} \text{ K}^{-1}$, SrApCl-10w20AlBSG: $14.5 \times 10^{-6} \text{ K}^{-1}$, SrApCl-10w20BaBSG: $16.2 \times 10^{-6} \text{ K}^{-1}$ and SrApCl-10w20PbBSG: $16.4 \times 10^{-6} \text{ K}^{-1}$). The glass-transition temperatures (T_g) values obtained from dilatometry (thermomechanical analysis) measurements exhibited the expected trend shown in thermal expansion measurements (lower the % thermal expansion, higher will be its T_g values). T_g values obtained from dilatometry and DSC measurements were shown in Table 7.1.

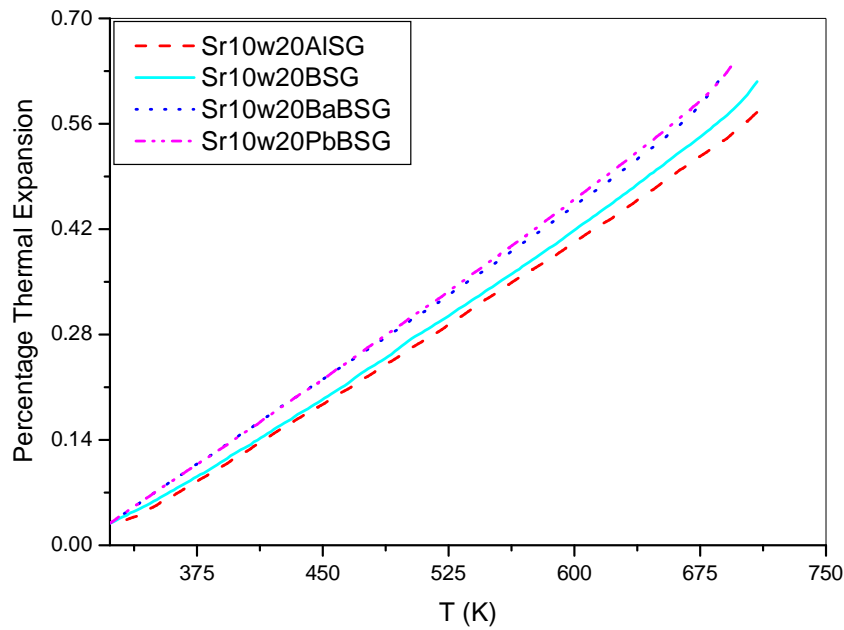


Fig. 7.1: Percentage thermal expansion vs. T (K) plot of Sr-chloroapatite glass-bonded composites with various types of glass bonding material

Table 7.1: T_g values of glass-bonded composites measured by dilatometry and DSC

Glass-ceramic compositions	T_g by dilatometry (K)	T_g by DSC (K)
SrApCl-10w20BSG	702 ± 5	704 ± 4
SrApCl-10w20AlBSG	710 ± 5	735 ± 4
SrApCl-10w20BaBSG	673 ± 5	685 ± 3
SrApCl-10w20PbBSG	680 ± 5	688 ± 3

Heat capacity values trend was found to be $C_{p, \text{SrApCl-10w20BSG}} > C_{p, \text{SrApCl-10w20AlBSG}} > C_{p, \text{SrApCl-10w20BaBSG}} > C_{p, \text{SrApCl-10w20PbBSG}}$ as shown in the Fig. 7.2. Higher heat capacity values are desirable for a good host matrix.

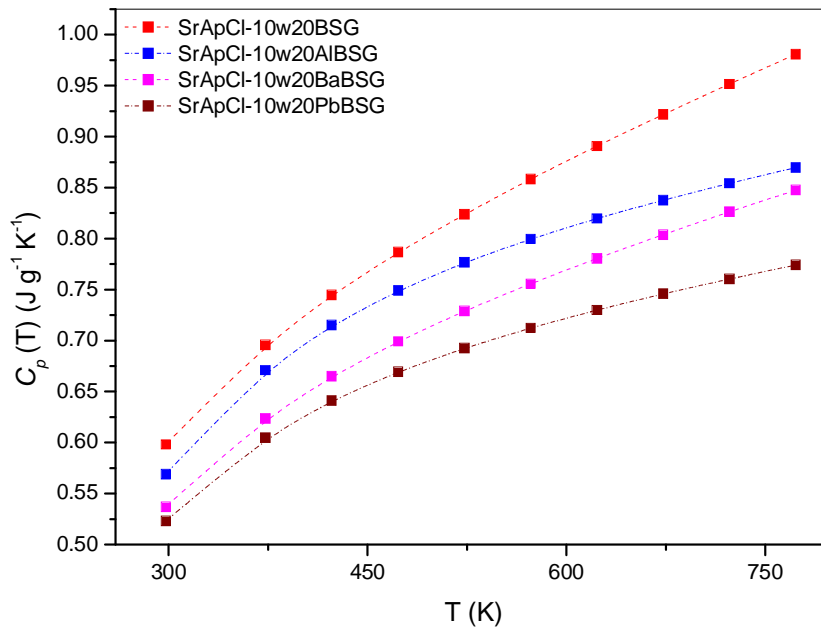


Fig. 7.2: Heat capacity (C_p) values of the glass-bonded composites obtained from drop calorimetry measurement

Form these above observations, it can be concluded that all the four various glass compositions form glass-bonded ceramic composites without any second phase with 10 wt.

% of simulated chloride waste. High temperature XRD (HTXRD) studies also show the absence of structural transitions or formation of new phases from the constituent elements added to the glass-ceramic composite on heat-treating the composites. These data reveals the structural stability of the composites in presence of the decay heat released from the radio-nuclides present in the waste form. The results obtained from leaching studies imply SrApCl-10w20BSG exhibit higher leach resistance than SrApCl-10w20AlBSG, SrApCl-10w20BaBSG and SrApCl-10w20PbBSG. The measured percentage thermal expansion found to show an increasing trend of SrApCl-10w20AlBSG < SrApCl-10w20BSG < SrApCl-10w20BaBSG \approx SrApCl-10w20PbBSG, which was also manifested in glass transition temperature. The trend of T_g values were found to be SrApCl-10w20AlBSG > SrApCl-10w20BSG > SrApCl-10w20PbBSG > SrApCl-10w20BaBSG. However, the difference in thermal expansion coefficients was very small. The measured heat capacity values found to be in the order of SrApCl-10w20BSG > SrApCl-10w20AlBSG > SrAPCl-10w20BaBSG > SrApCl-10w20PbBSG. C_p value is one of the important criteria for selecting the matrix and it is desirable to be high for the host matrix to qualify for waste immobilization.

From the above studies it can be concluded that 10 wt. % waste loading is feasible into the glass bonded ceramic composites without deviating from the desired criteria of a suitable matrix such as low leach rate, thermal stability *etc.* Among the various types of glass-bonded ceramic composites, SrApCl-10w20BSG is found to be more suitable and closely satisfy the desired requirements of a best matrix than SrApCl-10w20AlBSG, SrApCl-10w20BaBSG and SrApCl-10w20PbBSG composites.

Scope of the Work:

The Sr-chloroapatite glass bonded composite is a promising matrix for the immobilization pyrochemical waste. However, these studies can be extended to other alkaline earth chloro apatites (such as Ca-, Ba-chloroapatite *etc.*) to examine their suitability for the immobilization of pyrochemical waste. Various thermo-physical properties such as phase stability leach resistance in alkali and acid water, thermal expansion and heat capacity data of the matrices can be compared with the present work. This work can also be extended to the synthesis and characterization of oxo-, fluoro-apatites. These compositions can also be probed by replacing some of the phosphate group with silicate (SiO_4) groups. The present work describes the waste loading efficiency and their thermo-physical properties of Sr-chloroapatite with 20 wt. % of various glass compositions. A systematic study can also be done with the change in percentage of glass phase *i.e.* 10 wt. %, 20 wt. %, 30 wt. % 40 wt. % *etc.* On the other hand, the study of phosphate glasses can also be done in order to compare with borosilicate glasses. A comprehensive systematic study of individual waste element loading in Sr-chloroapatite can also be carried out experimentally and their experimental results can also be compared with the theoretical calculations.